
HETERODYNE SPECTROSCOPY WITH SINGLE ATOMS IN A HIGH-FINESSE OPTICAL CAVITY

Masterarbeit in Physik

von

Sebastian Manz

angefertigt im Institut für Angewandte Physik,
vorgelegt der Mathematisch-Naturwissenschaftlichen Fakultät
der Universität Bonn

Bonn, Oktober 2012

1. Gutachter: Prof. Dr. Dieter Meschede
2. Gutachter: Prof. Dr. Manfred Fiebig

Contents

Introduction	1
1 Coupling atoms to a high-finesse optical resonator	3
1.1 Theoretical background	3
1.1.1 The Jaynes-Cummings model	3
1.1.2 From closed to open systems - the master equation	5
1.2 Experimental setup	7
1.2.1 Magneto-optical trap	8
1.2.2 Transporting atoms to the cavity	8
1.2.3 Realization of strong coupling - a high-finesse optical cavity	10
1.2.4 Detection scheme	12
1.2.5 Cavity stabilization	13
1.2.6 Enhanced coupling control - a strongly focused dipole trap	14
1.3 Implementation of a heterodyne detection scheme	21
1.3.1 Experimental setup	22
1.3.2 Measurement procedure and data evaluation	23
2 Theoretical aspects of heterodyne detection	25
2.1 Analytical $g^{(2)}$ -function	25
2.2 Analytical spectrum of the $g^{(2)}$ -function	27
2.3 Discretized $g^{(2)}$ -function	29
2.4 Influence of afterpulsing and detector dead time	30
2.5 The discrete Fourier transform	33
2.6 Estimation of the signal-to-noise ratio	36

2.7	Verification of estimated signal-to-noise ratio	39
3	Mapping intracavity dynamics to the frequency domain	45
3.1	Theoretical description	46
3.1.1	Theoretical derivation of sideband scattering rates	46
3.1.2	Estimation of cooling rates for the experimental parameters	50
3.2	Measuring the quantized motion of single atoms	53
3.3	Analytical description of different broadening mechanisms	56
3.3.1	Influence of radial degree of freedom on sideband structure	56
3.3.2	Sideband transitions in sinusoidal potentials	60
3.3.3	Influence of lock laser intensity fluctuations	61
3.3.4	Level dependent transition linewidth	63
3.3.5	Resulting spectral line shape	63
3.4	Comparison of modeled line shape and measurements	65
3.5	Future challenges	67
	Summary and outlook	69
	Bibliography	71

List of Figures

1.1	Experimental setup of the cavity QED system	7
1.2	Recorded ICCD image of two atoms in the dipole trap	9
1.3	Cavity standing waves and detection scheme	12
1.4	Setup of the new strongly focused dipole trap	14
1.5	Shear plate images of the 2-inch collimator	17
1.6	Measured beam profile and expected point spread function	19
1.7	Radial oscillation frequencies	20
1.8	Heterodyne detection setup.	22
1.9	Data acquisition and analysis procedure	23
2.1	Exemplary $g^{(2)}$ function and corresponding spectrum	28
2.2	Effect of afterpulsing and detector dead time	30
2.3	Correction of afterpulsing and detector dead time	33
2.4	Exemplary schematic for the application of window functions	34
2.5	Fourier spectrum calculated with and without window function	35
2.6	Theoretical and measured spectral noise	40
2.7	Theoretical and measured sideband area	41
2.8	Theoretical and measured signal-to-noise ratio	42
3.1	Schematic of the assumed experimental situation	47
3.2	Phase dependence of scattering rates and averaged cooling map	51
3.3	Level scheme, sideband transitions and idealized spectral response	53
3.4	Motional sidebands at different lock laser intensities	55
3.5	Configuration of different trapping lasers	57

3.6	Spectral response function for the influence of radial broadening	60
3.7	Lock laser intensity distribution	62
3.8	Contribution of different broadening mechanisms	64
3.9	Comparison of measurement data and simulated line shapes	65
3.10	Comparison of one- and two-atom data	67

Introduction

The field of quantum electrodynamics deals with the interaction of light and matter. The experimental study of these interactions at the single particle level, i. e. of a single photon and a single atom, is of major interest in quantum optics. Besides mere observation, it is highly desirable to control and manipulate single atoms in order to realize qubits, the essential constituents of quantum computers. In contrast to a classical bit which can be either in state $|0\rangle$ or $|1\rangle$, a qubit can be in any superposition $|s\rangle = \alpha_0|0\rangle + \alpha_1|1\rangle$. Certain classes of computations can then be performed exponentially faster compared to today's classical computers [1]. One of the most prominent examples is Shor's algorithm for the prime factorization [2].

The development of quantum mechanics in the early twentieth century set the beginning of this new era in physics. Since then it was an experimental physicist's dream to explore the underlying mechanisms of our world at the single particle level. The major problem of single-photon single-atom systems in free space is their weak interaction, which makes it difficult to observe any effects [3]. The field of cavity quantum electrodynamics (CQED) in the strong-coupling regime [4, 5] opened up new possibilities: Here, the atom is placed between two highly reflecting mirrors, which form a resonator and thus enlarge the number of interactions between one atom and the same photon. A first theoretical model was developed by Jaynes and Cummings [6], who described the idealized interaction of a two-level atom with one quantized mode of the electromagnetic field without dissipation.

The realization of such systems took years. Especially manufacturing cavities of high finesse to enter the strong-coupling regime demanded great technological effort. The invention of laser cooling [7] was another major prerequisite to prepare, observe and manipulate quantum mechanical states at the single atom level. Placing atoms for longer times inside the cavity was realized with different techniques using a combination of laser cooling and gravity [8] or atomic fountains [9]. But perfect positioning could only be achieved with the application of dipole traps (DT) as optical conveyor belts [10–12]. These techniques allowed measurements at the single atom level e. g. the observation of the vacuum-Rabi splitting [8]. Since then fascinating experiments like the reconstruction of single atom trajectories (atom-cavity microscope) [13], the realization of the one-atom laser [14] or the observation of photon blockade [15] emerged. Further experiments entangled single photons with single atoms in optical cavities, paving the way for quantum networks in the future [16, 17].

The present experiment consists of a high-finesse optical cavity to which we can strongly couple single neutral cesium atoms. The latter are prepared in a stable hyperfine ground state $|F = 3, 4\rangle$ and can be loaded into the cavity using an optical conveyor belt. In the strong-coupling regime, one atom can already shift the cavity resonance such that the probe laser transmission is significantly suppressed depending on the atomic internal state. This allows non-destructive state measurements inside the cavity (quantum non-demolition measurement, QND) [18–20] by recording the transmission with a single photon counting module (SPCM). During the past years this technique has been exploited to analyze our system and investigate phenomena such as quantum jumps [21–24], Electromagnetically Induced Transparency (EIT) [23, 25, 26] and the Quantum Zeno Effect [23].

Until now all experiments performed with the present setup lacked proper control of the coupling strength. Proper coupling control is mandatory for certain entanglement schemes [27, 28] and is thus desirable to achieve. Two prerequisites to enhance the coupling control comprise perfect confinement and sufficient cooling of the atoms inside the cavity. Strong confinement of the atom inside the cavity was so far only attained along two spatial directions. Therefore, the implementation of a strongly focused dipole trap (SFDT) along the third direction allows three dimensional confinement and thus better control of the coupling strength g . Hence, as part of this thesis, a SFDT was set up and characterized. The second premise, sufficient cooling, can be achieved with the application of appropriate cooling techniques such as resolved-sideband Raman cooling [29] or EIT-cooling [23]. The extraction of cooling parameters such as the atomic temperature and the respective cooling rates inside the cavity is of major interest. So far the setup did not allow the evaluation of these parameters. Here, a new detection scheme, namely heterodyne detection [30], can be exploited to gain further insight into the current system. Heterodyne sideband spectroscopy allows the extraction of the temperature and cooling rate of the atoms inside the cavity from the structure of the motional sidebands which in turn reveals information whether ground-state cooling is already possible. Therefore, a heterodyne detection setup was implemented into the existing setup and characterized as part of this thesis. In addition, first measurements employing heterodyne sideband spectroscopy were performed and analyzed.

The present thesis is divided into three parts: Chapter one gives a brief theoretical introduction followed by a short description of the existing experimental setup. Subsequently, the implementation and characterization of the strongly focused dipole trap is presented. The chapter closes with an introduction of the heterodyne detection setup. Chapter two highlights theoretical aspects of heterodyne detection, emphasizing the estimation of the expected signal-to-noise ratio in comparison to the measurements. Finally, chapter three deals with heterodyne spectroscopy as a tool to map intracavity dynamics to frequency domain. At first a short theoretical introduction into cooling of the motional degree of freedom of a trapped atom in a cavity is given. First measurements of motional sidebands are presented and possible broadening mechanisms are discussed in detail. Eventually, the extracted temperature and cooling rate is compared to theoretical expectations.

Chapter 1

Coupling atoms to a high-finesse optical resonator

The essential objective of our CQED experiment is the realization of cavity-mediated coupling of two or more atoms in order to create entangled states. The following chapter first provides a short introduction into theoretical aspects. Furthermore the experimental constituents which are necessary to understand the subsequent chapters are briefly summarized. Finally, the implementation and characterization of the strongly focused dipole trap is discussed and the heterodyne detection setup is introduced.

1.1 Theoretical background

The interaction between single atoms and a mode of a light field in an optical resonator is known as cavity quantum electrodynamics. In principle one can distinguish between two processes: *coherent* and *incoherent* atom-light interaction. The first describes the idealized interaction between the atom and the light field without any dissipation to and thus interaction with the environment. This is described by the Jaynes-Cummings model.

Dissipative dynamics usually disturb the coherent evolution of the system under investigation. Nevertheless they are desirable in the setup because only due to those processes we are able to extract information from the system. Therefore, the next subsections will first introduce the idealized Jaynes-Cummings model and then take dissipative processes into account introducing the concept of the master equation.

1.1.1 The Jaynes-Cummings model

The Jaynes-Cummings model deals with the interaction of an idealized two-level atom with a single mode of the electromagnetic field. The atom possesses a ground state $|g\rangle$

and an excited state $|e\rangle$ and the electromagnetic mode is represented by the quantized mode of the resonator. The coupling is mediated via the electric dipole interaction and the Hamiltonian in the rotating wave approximation reads [5]

$$\hat{H}_{\text{dip}} = \hbar g(\mathbf{r}) (\sigma^\dagger a + \sigma a^\dagger) \quad (1.1)$$

where $g(\mathbf{r})$ is the position-dependent coupling factor, $\sigma = |g\rangle\langle e|$ the annihilation operator for an atomic excitation and a the annihilation operator for a photon in the cavity mode. The two contributions in the Hamiltonian can be intuitively understood: Either a photon is absorbed from an atom in the ground state which will then be in the excited state or the atom decays from the excited into the ground state and thus emits a photon into the cavity mode. It is important to point out that the dipole interaction leads to an energy exchange between atom and light field but no dissipative channel is included. The strength of the dipole interaction is determined by the coupling factor $g(\mathbf{r})$ which can be written as the product of the atomic dipole moment \mathbf{d} and the intracavity field $\mathbf{E}_c(\mathbf{r})$ [31]

$$g(\mathbf{r}) = \frac{\mathbf{d} \cdot \mathbf{E}_c(\mathbf{r})}{\hbar} = d \sqrt{\frac{\omega_c}{2\hbar\epsilon_0 V}} \psi(\mathbf{r}). \quad (1.2)$$

The right-hand side depends on the matrix element d of the corresponding transition, the frequency of the cavity field ω_c , the mode volume V and the spatial mode $\psi(\mathbf{r})$ which emphasizes the position dependence of the coupling strength. The latter is normalized to its maximum value.

Besides H_{dip} , the Hamilton operator for the two-level atom \hat{H}_a and the cavity mode \hat{H}_c have to be taken into account. The full Jaynes-Cummings Hamiltonian is then given by [6, 32]

$$\begin{aligned} \hat{H}_{\text{JC}} &= \hat{H}_a + \hat{H}_c + \hat{H}_{\text{dip}} \\ &= \hbar\omega_a \sigma^\dagger \sigma + \hbar\omega_c \left(a^\dagger a + \frac{1}{2} \right) + \hbar g(\mathbf{r}) (\sigma^\dagger a + \sigma a^\dagger) \end{aligned} \quad (1.3)$$

where ω_a denotes the atomic transition frequency between ground and excited state. Without interaction (i. e. $\hat{H}_{\text{dip}} = 0$) and on resonance ($\omega_a = \omega_c = \omega$) the two uncoupled eigenstates of $\hat{H}_a + \hat{H}_c$ are the tensor products $|g, n+1\rangle$ and $|e, n\rangle$ with degenerate eigenenergies [5]. Here, n denotes the number of photons in the cavity mode. The degeneracy can be lifted introducing the dipole interaction. On resonance the eigenenergies are

$$E_n^\pm = \hbar\omega \left(n + \frac{1}{2} \right) \pm \hbar g \sqrt{n+1} \quad (1.4)$$

with the corresponding eigenstates

$$|n, \pm\rangle = \frac{1}{\sqrt{2}} (|e, n\rangle \pm |g, n+1\rangle). \quad (1.5)$$

The energy splitting of $\hbar \cdot 2g$ between the states for $n = 0$ is also known as vacuum-Rabi splitting and the time evolution of the Schrödinger equation reveals oscillations between the two states $|e, n\rangle$ and $|g, n + 1\rangle$ at the so called Rabi-frequency $\Omega = 2g$. Therefore, the non-dissipative dynamics of the Jaynes-Cummings model are called coherent.

1.1.2 From closed to open systems - the master equation

The previous subsection dealt with the idealized interaction of an atom and a field mode, constituting a *closed* system. As already pointed out, a non-dissipative system does not represent the realistic case since the system under investigation is always coupled to the environment and is thus considered as an *open* system. In our experimental situation the coupling is mediated through two loss channels: One results from a cavity with non-zero losses at the mirrors leading to a decay of the intracavity field at a rate κ which corresponds to the half width at half maximum (HWHM) of the cavity linewidth. The second decay channel is represented by spontaneous emission of the atom to the environment at the dipole decay rate $\gamma = \Gamma/2$ with the natural linewidth Γ . Both effects lead to irreversible losses. In order to include these effects into the theoretical model, the atom-cavity system S is extended by a reservoir E consisting of a bath of harmonic oscillators to which the energy is lost [33]. The resulting Hamilton operator is given by $\hat{H}_{\text{tot}} = \hat{H}_S + \hat{H}_E$ with the Hamiltonian of the system (\hat{H}_S) and the reservoir (\hat{H}_E). Introducing the density operator $\tilde{\rho}$ for the Hilbert space of the atom-cavity system and the environment $\mathcal{H}_S \otimes \mathcal{H}_E$, the Heisenberg equation of motion reads

$$\dot{\tilde{\rho}} = \frac{1}{i\hbar} [\hat{H}_{\text{tot}}, \tilde{\rho}]. \quad (1.6)$$

Tracing over the degrees of freedom of the environment to achieve the reduced density operator ρ finally yields the so called *master equation*. It describes the interacting atom-cavity system including dissipative channels to the environment. For our system, it is given by [31, 33]

$$\begin{aligned} \dot{\rho} = & \frac{1}{i\hbar} [\hat{H}_{\text{JC}}, \rho] + \frac{1}{i\hbar} [\hat{H}_{\text{p}}, \rho] \\ & + \gamma (2\sigma\rho\sigma^\dagger - \sigma^\dagger\sigma\rho - \rho\sigma^\dagger\sigma) + \kappa (2a\rho a^\dagger - a^\dagger a\rho - \rho a^\dagger a). \end{aligned} \quad (1.7)$$

The two terms proportional to γ and κ describe the damping of the system's evolution. In order to observe coherent dynamics $g(\mathbf{r}) > (\gamma, \kappa)$ must hold, i. e. the coherent dynamics have to evolve faster than the atomic and cavity decay rate. If the inequality holds, the system is in the so called *strong-coupling regime* [5]. Besides dissipative channels, external driving of the atom-cavity system can also be taken into account. It is represented by the term including [34]

$$\hat{H}_p = -i\hbar\Omega_p (a + a^\dagger) \quad (1.8)$$

with the driving strength Ω_p at the probe laser frequency ω_p which is coupled into the cavity. According to [31] for a perfect cavity on resonance (i. e. $\omega_a = \omega_p = \omega_c$, ideal mode matching, no losses) the intracavity photon number $n_p = \langle a^\dagger a \rangle$ is related to the driving strength Ω_p as [34]

$$n_{p,0} = \frac{\Omega_p^2}{\kappa^2}. \quad (1.9)$$

For weak driving the solution for the normalized cavity transmission is given by [31]

$$\bar{T}(\delta, \Delta_{pc}, g) = \frac{\kappa^2 (\delta^2 + \gamma^2)}{(\gamma\kappa + g^2 - \delta\Delta_{pc})^2 + (\delta\kappa + \Delta_{pc}\gamma)^2}. \quad (1.10)$$

with the probe laser-atom detuning $\delta = \omega_p - \omega_a$ and the probe laser-cavity detuning Δ_{pc} . The normalized transmission corresponds to the average intracavity photon number divided by the intracavity photon number for an empty cavity on resonance ($n_{p,0}$). The dependence on the coupling strength g can be exploited for the detection scheme as will be discussed in subsection 1.2.4.

All theoretical derivations were based on the assumption that the atom is well confined within the cavity mode volume. A real atom has a finite temperature and thus cannot be considered as spatially stationary object. Proper control of the atomic position has to be experimentally assured and will be discussed in the next section.

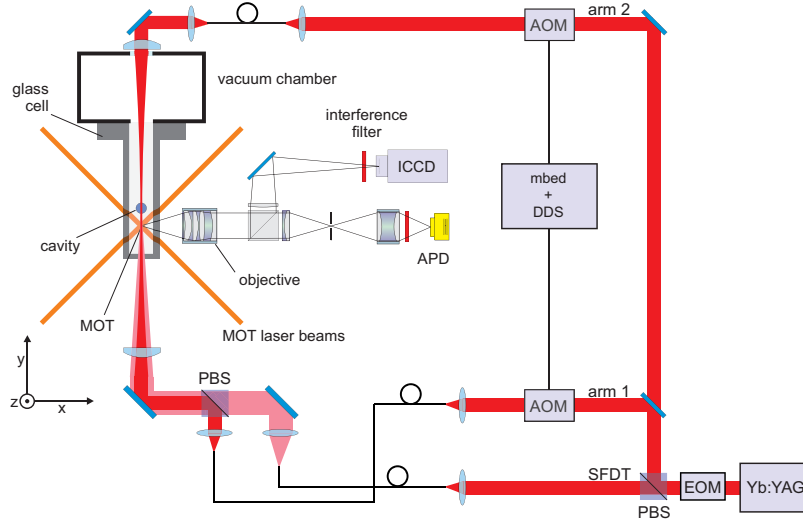


Figure 1.1 – Experimental setup of the cavity QED system: An Yb:YAG laser together with two acousto-optic modulators (AOM) and a direct digital synthesizer is used to generate a standing wave dipole trap along y . The second polarization degree of freedom is used for a new strongly focused dipole trap which allows for a tight confinement along x . Atoms are prepared in the MOT and transported with the DT to the center of the cavity where they interact with a probe laser running along z . Confinement along z is achieved with an additional laser, the so called lock laser. Imaging of the atoms inside the MOT is achieved by collecting the fluorescence light resulting from near resonant excitation with a high-numerical-aperture objective and an ICCD camera while atom counting in the MOT is realized with an APD.

1.2 Experimental setup

The experimental realization of strongly-coupled atom-cavity systems demands great effort and the existing setup has been continuously enhanced [23, 24, 26, 28, 35–45]. The following section will only give a brief overview on the experiment and focuses on the improvements which were integrated into the existing setup during the present thesis.

According to eqn. (1.2) the strong-coupling regime can be reached minimizing the mode volume V and decreasing the cavity decay rate κ . This can be realized with a high-finesse optical resonator. Since g also depends on the spatial mode profile, a good control of the atom's position inside the cavity is a prerequisite for sensitive measurements. Therefore, the preparation of cold cesium atoms will be discussed first. Additionally, the properties of the optical resonator and its stabilization are presented and a non-destructive detection scheme for the atomic state inside the cavity is introduced. Finally, two major improvements of the current setup are discussed: The confinement of the radial degree of freedom inside the cavity making use of an additional strongly focused dipole trap and the implementation of a heterodyne detection scheme, which provides the basis for theoretical calculations and measurements presented in chapter 2 and 3.

1.2.1 Magneto-optical trap

All experiments are performed in an ultra high vacuum glass cell which is connected to a cesium reservoir. A schematic representation of the setup is shown in figure 1.1. Trapping of neutral cesium atoms from the background gas is achieved with a magneto-optical trap (MOT) [7] which consists of three orthogonal pairs of counter-propagating laser beams. The latter are red-detuned with respect to the cesium D_2 transition $|F = 4\rangle \rightarrow |F' = 5\rangle$. Since a non-zero probability for transitions from $|F = 4\rangle$ to $|F' = 4\rangle$ exists, which could lead to a subsequent decay into the dark state $|F = 3\rangle$, a weak repumper is resonant with the $|F = 3\rangle \rightarrow |F' = 4\rangle$ transition compensating for this effect.

Atoms are decelerated and thus cooled exploiting the Doppler-effect: The atoms preferably absorb the red-detuned laser photons coming from the opposite direction compared to their propagation direction. This leads to a momentum decrease of the atom along that direction. The subsequent decay due to spontaneous emission entails the isotropic emission of a photon leading to no recoil on the atom on average. Thus, cooling of atoms becomes possible. In addition, a magnetic field gradient, resulting from a quadrupole field, lifts the degeneracy of Zeeman-levels which allows to trap the atoms at one position. Here, circularly polarized beams are utilized to exert position dependent restoring forces on the atoms, leading to spatial confinement of the atoms in the center of the MOT.

The loading rate of the MOT can be adjusted with an appropriate magnetic field gradient which can be switched from 30 G/cm at high loading rates to 300 G/cm with low loading rates but strong confinement. In order to achieve reasonable loading times, the MOT is loaded using low field gradients for several milliseconds (usually 50 – 300 ms) and is then switched to high field gradients. The number of loaded atoms can be determined via the detection of their fluorescence light, which is emitted due to near resonant excitation, using an objective lens with high numerical aperture together with an avalanche photo diode (APD) [46]. The desired number of loaded atoms in the MOT is achieved adjusting the loading time to an appropriate value and in addition performing multiple loading attempts. After a successful loading event, the atoms are then transferred into an optical dipole trap.

1.2.2 Transporting atoms to the cavity

As shown in figure 1.1, MOT and cavity are not at the same position but about 4.6 mm [23] apart and all atoms have to be transported from the position of the MOT to the center of the cavity. This is achieved with a dipole trap which can be used as optical conveyor belt as well. The dipole trap itself consists of two counter propagating, linearly polarized laser beams at $\lambda_{DT} = 1030$ nm and thus far off-resonant with respect to the cesium D_2 transition at $\lambda = 852$ nm used in this experiment. Both beams are generated from a single Yb:YAG laser (ELS VersaDisk-1030-10-SF) which is split into two arms whereas each of them has a power of approximately $P' = 1.8$ W at the position of the cavity. The resulting standing wave creates a conservative potential with a potential

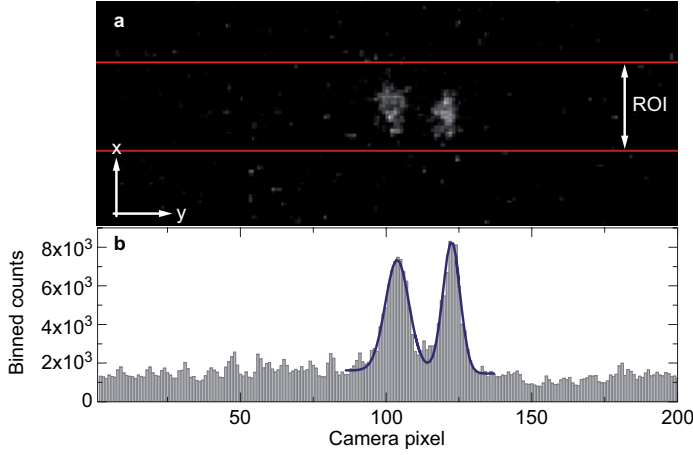


Figure 1.2 – (a) Image of two Cs atoms recorded with the ICCD camera. The red lines mark the region of interest (ROI). (b) Corresponding count histogram, where each bar contains the vertically binned counts of each pixel in the ROI. The atomic position is determined with a subsequent Gaussian fit routine (blue lines).

well separation of $\lambda_{\text{DT}}/2$ and a typical trap depth of [37]

$$U_{\text{DT}} = \frac{3\pi c^2 I_{\text{DT}} \Gamma}{2\omega_0^3 \Delta_{\text{eff}}} = k_B \cdot 1 \text{ mK} \quad (1.11)$$

allowing strong confinement along the y -direction. Here, $\Gamma = 2\pi \cdot 5.22 \text{ MHz}$ is the natural transition linewidth, ω_0 the corresponding atomic resonance frequency and $I_{\text{DT}} = 4P/(\pi w_{\text{DT},0}^2)$ the intensity of the standing wave at the anti-node with the beam waist ($1/e^2$ -radius) of the dipole trap laser and the total power $P = 2P'$. In addition, Δ_{eff} denotes the effective detuning between the dipole trap and the atomic transitions, taking into account all contributions from the D_1 and D_2 line [31, 37, 38]. The dipole trap waist $w_{\text{DT},0} = (32.5 \pm 0.4) \mu\text{m}$ lies at a distance of 2.2 mm from the cavity position and 2.4 mm from the MOT position resulting in different beam diameters at the respective point. The dipole trap waist at the position of the cavity is $w_{\text{DT},\text{cav}} = (39.1 \pm 1.5) \mu\text{m}$ resulting in typical trap frequencies along this direction at the order of 300 kHz [23].

In order to transport the atoms to the center of the cavity mode, the exact initial and final position have to be known. After transferring the atoms from the MOT into the dipole trap, imaging of the atoms is achieved by illumination with molasses beams which cause fluorescence light of each atom. The latter is in turn recorded with an intensified CCD-camera (ICCD, Roper Scientific PI-MAX). A typical picture is shown in figure 1.2 (a). Subfigure (b) shows the vertically binned pixels as histograms to determine the atoms' positions using a one dimensional fit function. The resolution of the resulting image is limited to $1.8 \mu\text{m}$ by the imaging objective [46] but the positions in the optical dipole trap can be determined with an accuracy of 143 nm [47]. This procedure allows the calculation of the distance to the center of the cavity mode needed for the computer-controlled transport. The center of the cavity is determined once before measurements are performed, for details see [35].

The transport itself is realized with a detuning δ_{DT} between both arms of the dipole trap. The interference pattern resulting from both beams will then move with a velocity

v which is given by [48]

$$v = \frac{\lambda_{\text{DT}} \delta_{\text{DT}}}{2} \quad (1.12)$$

and hence atoms are transported since they are attracted by the moving intensity maxima. The detuning is achieved with two acousto-optic modulators (AOMs) which were usually driven at 100 MHz by a digital frequency discriminator (DFD 100, APE Berlin). During the present thesis, the DFD turned out to be an unreliable source and was defective several times. Therefore, a new custom build setup was developed recently [49, 50] and integrated into the current setup. Now, a direct digital synthesizer (AnalogDevices DDS AD9954) running at a clock frequency of 400 MHz is controlled by an mbed microcontroller (ARM mbed NXP LPCL768) and replaces the DFD. The two output channels of the DDS each generate the sinusoidal 100 MHz signal at -5 dBm. Additional amplification results in an output power of approximately 34 dBm which is then used to drive the respective AOM. Measurements revealed a $1/e$ lifetime of the atoms of 16 s in the DDS-driven dipole trap configuration which is sufficiently high to perform all experiments. The DDS also gives more flexibility since arbitrary frequency ramps can be written into the DDS-RAM. In addition, the phase noise is reduced compared to the former DFD and the transport itself does not lead to additional atom losses. To conclude, the new setup represents an adequate and cheap replacement for the DFD.

1.2.3 Realization of strong coupling - a high-finesse optical cavity

After transporting the atoms to the center of the cavity mode, the atom shall be coupled to the latter. As mentioned above the strong coupling condition demands $g(\mathbf{r}) > (\gamma, \kappa)$. Since γ cannot be modified and is fixed by nature, the coupling factor $g(\mathbf{r})$ can be optimized as well as the cavity field decay rate κ . The latter should be chosen reasonably small which can be achieved with a high-finesse optical resonator. Here, a good trade-off between low values for κ and a sufficient signal strength at the cavity output mirror is necessary. The cavity used in the experiment is a Fabry-Perot resonator, consisting of two super-polished mirror substrates with highly-reflective dielectric coatings resulting in extremely low absorption and transmission losses ($\mathcal{A} = (2.0 \pm 0.2) \cdot 10^{-6}$, $\mathcal{T} = (0.6 \pm 0.1) \cdot 10^{-6}$ [31]). The mirror separation $l \approx 160 \mu\text{m}$ [31] gives a free spectral range (FSR) of

$$\omega_{\text{FSR}} = \frac{2\pi c}{2l} = 2\pi \cdot 0.95 \text{ THz} \quad (1.13)$$

which can be used to calculate the cavity field decay rate

$$\kappa \approx \omega_{\text{FSR}}(\mathcal{T} + \mathcal{A})/2\pi = 2\pi \cdot (0.40 \pm 0.02) \text{ MHz}. \quad (1.14)$$

The finesse then yields

$$\mathcal{F} = \frac{\omega_{\text{FSR}}}{2\kappa} = (1.2 \pm 0.1) \cdot 10^6 \quad (1.15)$$

and is a good figure of merit for the quality of the resonator. A rather intuitive picture can be achieved considering a single photon inside the resonator which will be reflected about $\mathcal{F}/\pi = 400000$ times before it is lost due to absorption or transmission [23]. Further details on the cavity characterization and properties can be found in [12, 21, 28, 31, 40].

The second parameter to be optimized is the coupling strength $g(\mathbf{r})$ (see eqn. (1.2)). It reveals a dependence on the mode volume V which should be chosen as small as possible in order to enhance the coupling strength. For the existing experiment the mode volume can be calculated according to [40]

$$V = \frac{\pi}{4} w_{0,\text{cav}}^2 \cdot l, \quad (1.16)$$

with the cavity mode waist $w_{0,\text{cav}} = 23 \mu\text{m}$. The maximum coupling strength in the center of the cavity mode can be calculated with eqn. (1.2) if the mode function is set to unity [40]:

$$g_0 = d \sqrt{\frac{\omega_c}{2\hbar\epsilon_0 V}} = 2\pi \cdot 18 \text{ MHz}. \quad (1.17)$$

This value is only achieved for the atomic transition $|F = 4, m_F = \pm 4\rangle \rightarrow |F' = 5, \pm 5\rangle$. Due to the birefringence of the cavity only linearly polarized light can be coupled into the resonator driving π or σ^+/σ^- transitions which lead to a population of all m_F sublevels. Since each sublevel has a slightly different coupling constant, this will lead to a decrease of the overall coupling strength. As shown in figure 1.1 strong confinement inside the cavity along y is assured with the dipole trap. Along the z -direction, a standing wave created by a lock laser, which is used to stabilize the cavity, serves as confining potential. In addition, a probe laser, which pumps the intracavity field, is coupled into the cavity as well. It is too weak to create a confining potential but the different wavelengths of lock and probe laser lead to a continuous spatial shift of the corresponding field maxima as illustrated in figure 1.3 (a). The detuning between lock and probe laser is usually chosen such that the anti-node of the probe laser coincides with a node of the blue detuned lock laser in the center of the cavity to trap the atom at the maximum probe laser field strength and thus achieve maximum coupling strength (for details, see [31]). Some experiments also demand a controlled positioning at the anti-node of the probe field which can be achieved changing the detuning between lock and probe laser. This will be used in chapter 3.

Besides hopping along the y - and z -direction, weak confinement along x leads to a further reduction of the coupling strength. Nevertheless, the experimental setup fulfills the strong-coupling condition: The experimentally achieved effective coupling strength $g_{\text{eff}} = 9 \text{ MHz} > (\kappa, \gamma)$ determined from the recorded transmission [31] was smaller than the theoretical value g_0 . In this region, already a single atom coupled to the cavity can lead to a significant change of the transmission spectrum of the cavity, depending on the chosen detunings between cavity, atom and probe laser (see also eqn. (1.10)). This effect is exploited for the non-destructive hyperfine state detection, which will be discussed next.

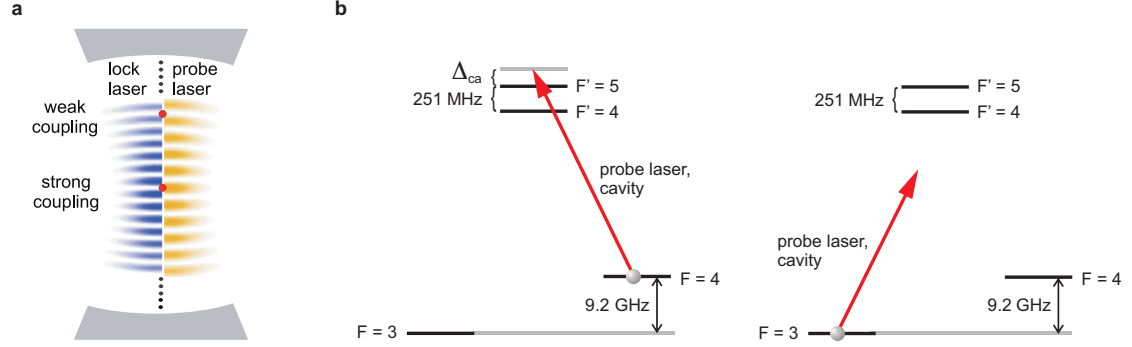


Figure 1.3 – (a) Intracavity distribution of lock and probe laser standing waves. Here, the lock laser is blue detuned from the probe laser and thus maximal coupling is achieved in the center of the cavity (lower red point) whereas minimal coupling is achieved at a node of the probe laser standing wave (upper red point). (adapted from [12]) (b) Detection scheme used for the transmission measurements: A Cs atom in state $|F = 4\rangle$ is near resonant to the cavity resonance and hence changes the transmission according to eqn. (1.10). An atom in state $|F = 3\rangle$ is far off-resonant and thus does not change the transmission. (adapted from [31])

1.2.4 Detection scheme

The stable hyperfine states $6^2S_{1/2}, |F = 3, 4\rangle$ of neutral cesium atoms are utilized to achieve an effective two-level system. A non-destructive state detection (QND measurement) inside the optical resonator can be achieved exploiting the modification of the transmission spectrum due to the strong coupling between atom and cavity. The cavity (ω_c) is usually blue detuned by several natural linewidths Γ from the $|F = 4\rangle \rightarrow |F' = 5\rangle$ cesium D_2 -transition at frequency ω_a resulting in a detuning δ . The probe laser at frequency ω_p is resonantly coupled into the cavity (i. e. $\Delta_{pc} = \omega_p - \omega_c = 0$) and its transmission is recorded with a single photon counting module (Perkin Elmer SPCM-AQRH-13). Once an atom in state $|F = 4\rangle$ is loaded into the cavity, the coupling g leads to a shift of the cavity frequency displacing the cavity out of resonance with respect to the probe laser. As a consequence the transmission of the probe laser is suppressed (see eqn. 1.10). If, on the other hand, an atom in state $|F = 3\rangle$ is loaded into the cavity, the probe laser and the cavity are far detuned from the atomic transition due to the large hyperfine splitting of 9.2 GHz (see figure 1.3 (b)). In this case the atom and the cavity are almost decoupled and there is hardly any transmission drop visible.

Hence, a non-destructive state detection for $|F = 4\rangle$ inside the cavity is possible but the state $|F = 3\rangle$ cannot be distinguished from an empty resonator. This can be circumvented applying a weak repumper on the $|F = 3\rangle \rightarrow |F' = 4\rangle$ transition which finally leads to a subsequent decay into $|F = 4\rangle$ and a transmission drop can then be detected which assures that the atom was not lost.

1.2.5 Cavity stabilization

Although the detection should in principle work as described above, it demands great effort to stabilize the setup [12, 23, 39, 40, 43]. Due to the narrow cavity linewidth of 2κ , a high stabilization of the cavity length with respect to the probe laser frequency ω_p is mandatory. Otherwise, the probe laser transmission would exhibit vast fluctuations on the SPCM, leading to the impossibility of proper measurements. Already a fluctuation of the cavity length l at the order of 10^{-13} m would lead to a complete suppression of the probe laser transmission [23]. Stabilization can be achieved with shear-piezoelectric transducers together with the lock laser at $\lambda_{\text{lock}} = 845$ nm. The latter runs along the cavity axis and its reflection is used to generate an error signal exploiting the Pound-Drever-Hall method [51]. Additionally, the lock laser is coupled into a so called transfer cavity which in turn is stabilized by a cooling laser. The latter is stabilized on the crossover signal of the $|F = 4\rangle \leftrightarrow |F' = 3/5\rangle$ transition of a cesium spectroscopy cell. Since the probe laser is generated from the cooling laser, cavity length and probe laser wavelength are stabilized with respect to each other. Due to the high intensity of the lock laser compared to the probe laser, any signal measured with the SPCM would be predominated by the lock laser transmission signal. Therefore, the polarization of both beams was chosen orthogonal which enables the suppression of the lock laser using a Glan-Allen-polarizer together with a holographic grating [28, 31].

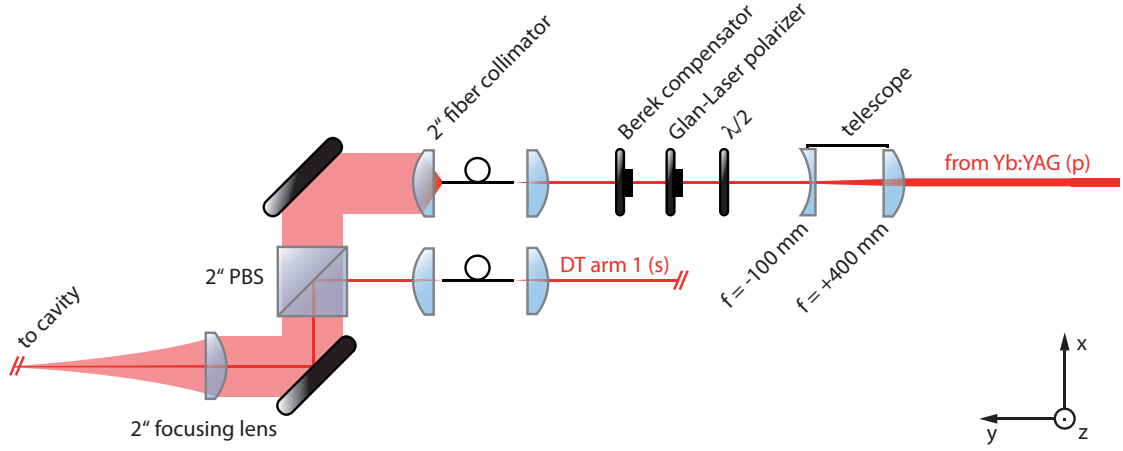


Figure 1.4 – Schematic sketch of the new strongly focused dipole trap superimposing arm 1 of the old DT.

1.2.6 Enhanced coupling control - a strongly focused dipole trap

In order to achieve three-dimensional confinement and thus enhanced coupling control additional confinement along the x -direction is necessary. A broad trapping potential has so far only been generated by the Gaussian shape of the lock and dipole trap intensity distribution. Their waists are at the order of $20 - 40 \mu\text{m}$ resulting in a weak confinement compared to the typical lattice separation of $0.4 - 0.5 \mu\text{m}$ along the other directions. The position dependent coupling strength $g(x)$

$$g(x) \propto \exp\left[-\frac{x^2}{w_{0,\text{cav}}^2}\right] \quad (1.18)$$

with the cavity mode waist $w_{0,\text{cav}}$ reveals a general problem: Due to their finite temperature, atoms can oscillate with a higher amplitude along the x -direction, leading to a rather large displacement compared to the y - and z -direction. The weak confinement also allows atoms to change their trapping site along y and z [40]. Both effects lead to a change of the coupling strength. The elimination of this degree of freedom is mandatory for stable and reproducible measurement results, especially for the observation of coherent processes. The limited space available in the experiment prohibits the integration of an additional standing wave dipole trap along the x -direction. Instead, the confining potential of a strongly focused Gaussian beam propagating along y was exploited to achieve stronger confinement along x and z by a reduced beam waist $w_{\text{SFDT},\text{cav}} < w_{\text{DT},\text{cav}}$ at the cavity position. Therefore, in addition to the existing dipole trap, a SFDT based on the idea in [35] was implemented into the setup during this thesis. In the following paragraph the experimental setup, its characterization and first measurements comparing the old and the new configuration are presented.

Experimental implementation In general, for the optical potential created by a Gaussian beam propagating along y it holds

$$U(r, y) \propto I(r, y) = I_0 \cdot \left(\frac{w_{\text{SFDT, cav}}}{w(y)} \right)^2 \exp \left[-\frac{2r^2}{w^2(y)} \right] \quad (1.19)$$

with the peak intensity I_0 at the waist position in the center of the cavity, the beam radius $w(y)$ and $r^2 = x^2 + z^2$. At $y = 0$, which corresponds to the center of the cavity, we can write

$$U(r, 0) \propto I_0 \exp \left[-\frac{2r^2}{w_{\text{SFDT, cav}}^2} \right]. \quad (1.20)$$

Thus, a reduction of the waist $w_{\text{SFDT, cav}}$ leads to a steeper decrease of the optical potential along x and z and to a stronger confinement of the atoms. In principle, the beam waist could be made arbitrarily small, only limited by the Yb:YAG laser wavelength. In the far field approximation it holds

$$w(y) = y \cdot \tan [\theta] \quad (1.21)$$

with the beam divergence given by

$$\theta = \frac{\lambda}{\pi w_{\text{SFDT, cav}}}. \quad (1.22)$$

Hence, the beam radius increases faster along y with decreasing beam waist $w_{\text{SFDT, cav}}$. Here, a commercially available 2"-lens¹ placed at a distance of 300 mm to the cavity sets an upper limit. The maximum size for the beam radius at that position is 12 mm since the aperture should have a diameter of at least $4w(y)$ to avoid optical aberrations. With this configuration the resulting beam waist at the center of the cavity yields $8.2 \mu\text{m}$ which is almost five times smaller than the original DT radius at the cavity position.

The new SFDT is already included in figure 1.1. An additional schematic drawing of the SFDT setup is shown in figure 1.4. Since the counterpropagating laser beams of the old DT are mandatory to transport and confine the atoms along y the SFDT shall be used in addition. For the new setup, the second polarization degree of freedom of the Yb:YAG laser (p-polarized) is used to superimpose one arm of the DT (arm 1, s-polarized) with the SFDT using a polarization beam splitter (PBS). Since the maximal power of the existing Yb:YAG laser is limited, an electro-optic modulator (EOM) is used for an adequate distribution among both traps depending on the experimental demands: For the transport of atoms to the cavity a deep dipole trap potential is mandatory and thus the maximum power available is required. Otherwise an increased loss of atoms would arise during the transport. Once the atoms are inside the cavity, the power in both

¹1 inch = 2.54 cm

DT arms can be decreased adiabatically while the SFDT power is increased using the EOM. Finally, the power is shared equally among both traps resulting in a reduced power of 0.9 W in each arm of the original DT and 1.8 W in the SFDT. Theoretical calculations reveal that the trap frequency along the y -direction will be reduced from approximately 320 kHz to 225 kHz, but the radial frequency along the x -direction increases from 2 kHz to 15 kHz. For first characterization measurements this property can be exploited to prove better radial confinement.

Polarization maintenance The dipole trap demands stable intensities and a high polarization purity for the position-dependent manipulation of the hyperfine ground states in cesium atoms. Deviations, e. g. due to polarization mixtures between the orthogonal modes of a polarization maintaining fiber, lead to time-dependent light shifts, which can destroy any coherent processes inside the cavity [35, 38, 52]. In order to achieve high polarization purity for the SFDT the beam passes through a Glan-Laser polarizer (Thorlabs Glan-Laser Calcite Polarizer GL5-A) and would in principle be coupled into a single mode fiber which is used to clean up any other than the TEM_{00} mode. Additionally, the fiber also guarantees a stable transfer of the beam to the desired position without introducing additional instabilities caused by optical elements like mirrors. The polarization purity for both ends of the used fiber was determined according to the procedure described in [35] and yields $[P_{\perp}/P_{\parallel}]_1 = 5 \cdot 10^{-3}$ and $[P_{\perp}/P_{\parallel}]_2 = 2 \cdot 10^{-4}$ for the respective side. Here, P_{\perp} and P_{\parallel} denote the particular power in the two orthogonal polarization modes. We chose the better end facet to be at the output in order to prevent any additional polarization impurity. The bad input polarization conservation could be compensated using a Berek compensator (Thorlabs GL5-B) before the beam is coupled into the fiber. This improves the polarization extinction by nearly an order of magnitude to $5 \cdot 10^{-4}$.

Characterization of the 2-inch collimator and polarization beam splitter The fiber output is connected to a 2''-collimator (Schaefer+Kirchhoff 60FC-T-4-M200-37) to achieve the required beam radius of 12 mm. Since wavefront distortions can lead to aberrations the wavefront quality of the collimator was checked with a shear plate interferometer (Melles Griot, Model 09 SPM 005). The results for parallel and perpendicular orientation of the collimator with respect to the interferometer, which was placed in front of the optics at a distance of 50 cm, are shown in figure 1.5. A perfectly collimated beam should result in an interference pattern completely parallel to the red line. In contrast, a non-collimated beam would exhibit a parallel but rotated pattern with respect to the red line. The observed pattern is parallel to the red line and thus collimated. Nevertheless, a slight s-shape indicates minor spherical aberrations [53]. The latter effect occurs in both orientations and might result from an imperfect collimator lens. In addition, both interference patterns exhibit a decreasing intensity with increasing distance from the center which results from the Gaussian intensity distribution of the beam.

The DT and SFDT beams are superimposed using a 2''-polarization beam splitter (man-

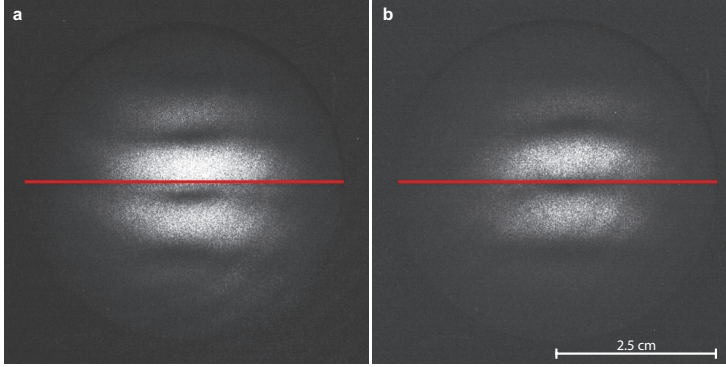


Figure 1.5 – Shear plate images taken at a distance of 50 cm in front of the 2-inch collimator in (a) parallel and (b) vertical orientation.

ufactured by LENS-Optics GmbH). Its extinction ratio for s- and p-polarized light was determined for all four sides measuring the power of a linearly polarized impinging beam at the transmission and reflection port for both polarization directions. We subsequently chose the ports with highest performance. The best extinction ratio for transmission and reflection yield

$$\begin{aligned} \left[P_{\parallel}/P_{\perp} \right]_{\text{T}} &= 3 \cdot 10^{-4} \quad \text{and} \\ \left[P_{\perp}/P_{\parallel} \right]_{\text{R}} &= 5 \cdot 10^{-2} \quad , \text{ respectively.} \end{aligned} \quad (1.23)$$

The transmission port was selected for the SFDT since the maximum intensity at the position of the cavity

$$I_{\text{max}} = \frac{2P}{\pi w_0^2} \quad (1.24)$$

depends quadratically on the waist. Thus, polarization fluctuations will be more severe due to higher intensity values leading to stronger differential light shifts between the hyperfine ground states compared to the less confined DT.

Aside from poor extinction ratios, wavefront distortions induced by an improper surface quality of the beam splitter can have a negative impact, too. Therefore, the selected surface roughness (peak-to-valley) of the cube is about $\lambda/10$ which is the best commercially available value. The influence of the PBS on the wavefront was tested revealing no additional distortion of the interference pattern on the shear plate interferometer. Additionally, the transmission losses due to the cube were checked and amount to less than 5 % which agrees well with the value given on the data sheet.

Analyzing the beam profile of the SFDT Due to the new beam radius of 12 mm the former focusing lens had to be replaced by a new 2''-lens (Schaefer+Kirchhoff 40M-M300-02, $f=300$ mm). A full simulation of the point spread function (PSF) using the computer software *OSLO* including all available lens parameters was performed and compared to the real beam profile to check the mode quality around the focal point F .

The beam profile was recorded for the new lens in combination with the 2''-collimator along the beam direction in steps of $50\ \mu\text{m}$ in a region of $\pm 1500\ \mu\text{m}$ around F . The normalized¹ results are displayed in figure 1.6 and compared to the simulation.

In figure 1.6 (a) a x - y cut through each beam profile at the central peak (at $z = 0$) is shown for every recorded beam profile resulting in a two-dimensional intensity distribution. The corresponding simulated result is displayed in subfigure (b). Theoretical and experimental results are consistent: The predicted double peak structure between $-1500\ \mu\text{m}$ and $-400\ \mu\text{m}$, which results from spherical aberrations, could be experimentally confirmed as well as the expected mode quality behind the focal point. Similar results were obtained for a z - y cut (not shown).

For a detailed analysis, three distinct beam profiles are shown in subfigures (c) - (e) and compared to the simulation presented in (f) - (h). The first shows the beam profile at the position of the double peak structure ($-500\ \mu\text{m}$) which translates into a doughnut-like profile. Experimental results agree with the PSF but in addition a slight inhomogeneity in the intensity distribution is apparent which is also visible in (a) as asymmetry between the two branches. This effect might result from a slight displacement between the optical fiber and the collimator.

In contrast, subfigure (d) reveals a Gaussian shaped intensity distribution at the focal point F with a reduced peak intensity compared to the simulation. This might result from two reasons: First, due to the comparable size of the beam waist and the pixel size of the beam profile camera ($4.4\ \mu\text{m}$) the peak intensity might be distributed among two bins and thus be reduced whereas the simulated peak value occupies exactly one bin. Second, due to optical aberrations the real waist is increased compared to the simulation. A two-dimensional fit of an elliptical Gaussian function resulted in a waist of $(10.1 \pm 1.0)\ \mu\text{m}$ and $(9.5 \pm 1.0)\ \mu\text{m}$ along the two orthogonal directions. The waist size at the focal point is thus slightly bigger than the simulated result of $w_{\text{SFDT}} = 8.8\ \mu\text{m}$ for an initially collimated beam of $12\ \text{mm}$ radius. In addition, a minor elliptical shape is present which probably results from an elliptical beam profile at the collimator input. Deviations might occur due to the finite pixel size but a self-written fitting routine taking the averaging effect of each pixel into account also resulted in bigger radii compared to the values of the PSF. Another method to determine the waist size is based on the calculation of the variance σ_w^2 of the measurement data. Under the assumption of a Gaussian beam, it holds $2\sigma_w = w_{\text{SFDT}}$ and the results agree with those achieved from the Gaussian fit. A careful analysis revealed that the position of the minimal waist has an uncertainty of approximately $\pm 75\ \mu\text{m}$ depending on the method which is used to determine the waist. From the deviations between the Gaussian fit results and the calculated variance we were able to estimate the uncertainty for the SFDT waist to 10 % of its value.

In contrast to the poor beam quality in front of the focal point, the Gaussian shape is well maintained behind F as apparent in subfigure (e). It agrees with the simulated point spread function.

¹Proper normalization was achieved dividing by the sum of all pixel values in each beam profile/PSF image.

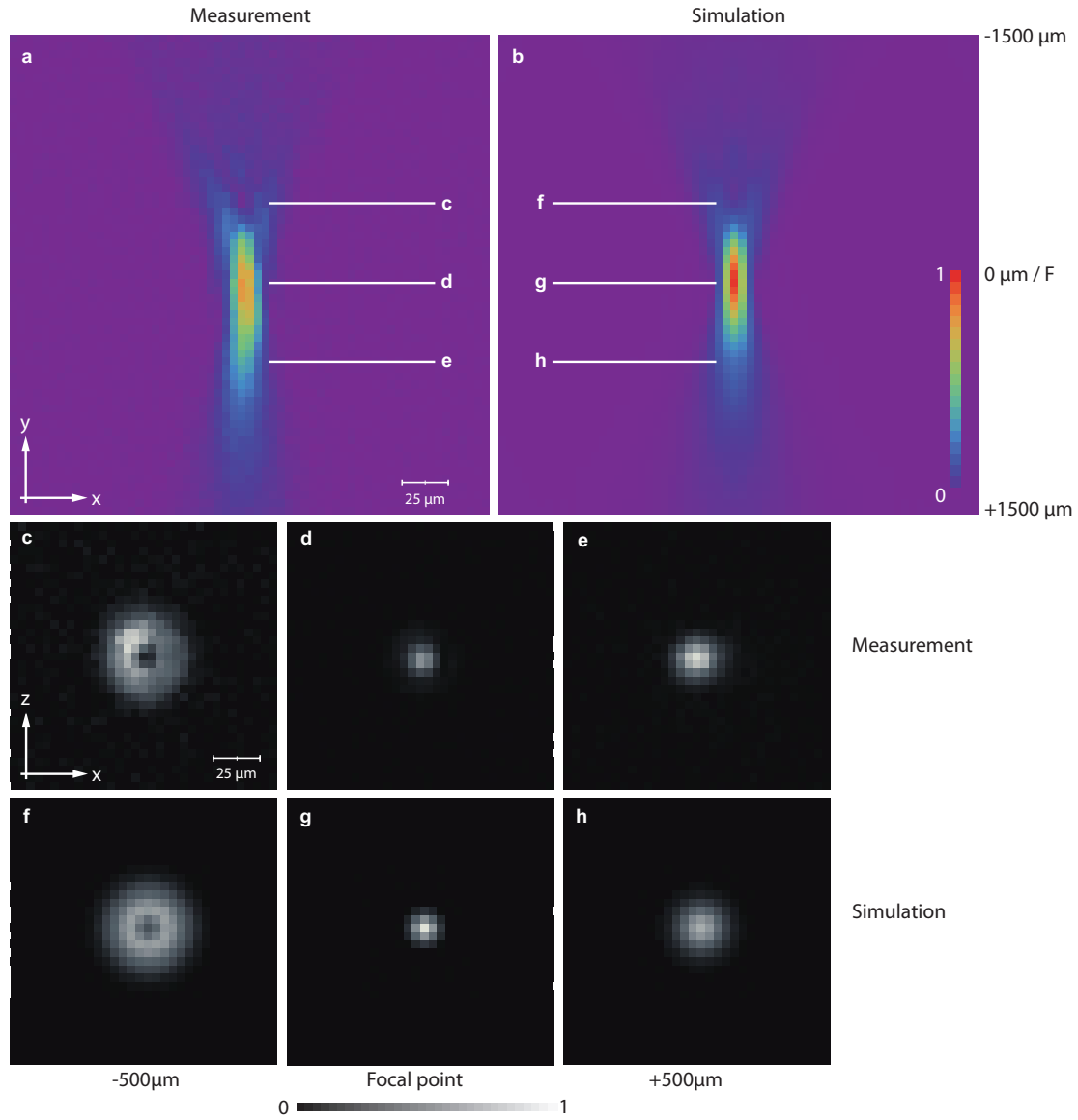


Figure 1.6 – Comparison of the measured beam profile and the expected point spread function: (a) $x - y$ - cut of the measured intensity distribution at $z = 0$, i. e. through the intensity peak of each recorded beam profile image. (b) Theoretically expected point spread function. In addition, the measured beam profile (c) in front of, (d) at and (e) behind the focal point F is shown. (f) - (h) display the expected beam profiles resulting from the calculated point spread function at the respective positions marked in subfigure (b).

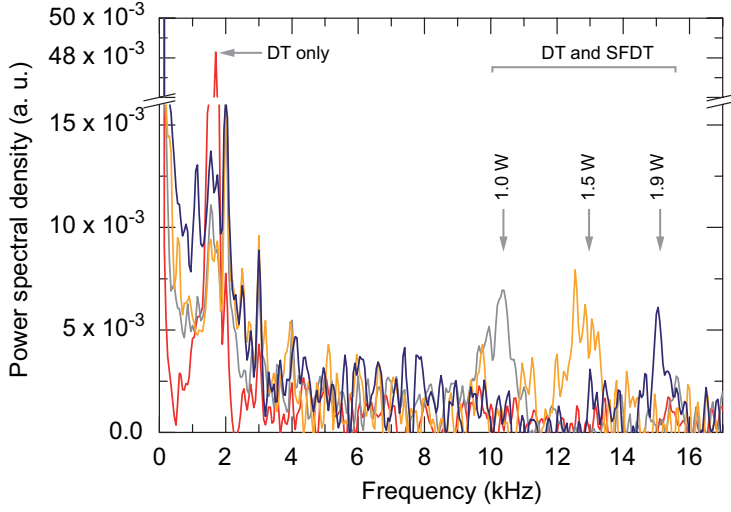


Figure 1.7 – Measured radial oscillation frequencies with the DT only (red) and with the SFDT in addition at 1.0 W (grey), 1.5 W (orange) and 1.9 W (blue). At 1.9 W the radial oscillation frequency yields (15.3 ± 0.3) kHz. The spikes at multiples of 1 kHz result from a background signal and do not originate from the atomic motion.

To conclude, a slight misalignment between the center of the cavity mode and the beam waist not only increases the beam radius at the cavity position but can also introduce negative effects due to non-Gaussian beam profiles. Further simulations revealed that the glass cell, which encloses the cavity, should not have a negative effect on the beam profile. Nevertheless, due to dust particles and tiny scratches on the surface of the glass cell, additional distortions might still occur.

Extraction of the radial trap frequency After proper alignment of the waist position with respect to the cavity mode the confinement of the atoms inside the cavity has to be quantified. An appropriate observable is the radial trap frequency ω_x since the extension of the atomic wave package ε relates to the oscillation frequency as

$$\varepsilon \propto \frac{1}{\sqrt{\omega_x}}. \quad (1.25)$$

The trap frequency can be extracted if the atoms are transported to the linear slope of the cavity mode instead of the center. Here, the cavity transmission is proportional to the coupling strength g and the latter in turn scales linearly with the atomic displacement x . Therefore, the radial oscillation frequency can be mapped to the cavity transmission. The subsequent calculation of the autocorrelation function of the recorded transmission followed by the application of the Fourier transform finally allows the extraction of the trap frequency. Figure 1.7 shows the results we achieved for the DT and SFDT configuration. Without the strongly focused dipole trap, the extracted oscillation frequency is (1.8 ± 0.2) kHz (red) while an increase is observed if the power in the SFDT branch is raised. For a power of 1.9 W in the SFDT at the position of the cavity the measured radial oscillation frequency yields (15.3 ± 0.3) kHz (figure 1.7, blue) and agrees with the theoretical expectation of 16 kHz. The extension of the atomic wave package

then reduces by a factor of three along the radial direction.

In summary, first measurements indicate that stronger confinement of the atoms inside the cavity can be achieved with the new strongly focused dipole trap but further tests are required. An imperfect polarization purity of the DT/SFDT configuration for example might still cause additional problems. Already a small admixture of circularly polarized light can lead to a strong position dependent hyperfine level splitting. This is of major disadvantage for proper microwave spectroscopy and further investigations are necessary. Additionally, cavity transmission traces can be recorded for atoms coupled to the anti-node of the cavity. The respective histograms should reveal a better agreement with a Poissonian distribution compared to the distribution resulting from measurements with the DT only. This would in turn allow a better distinction between one and two atoms coupled to the cavity mode as demanded for proper feedback control of the atomic states inside the cavity [24].

1.3 Implementation of a heterodyne detection scheme

The investigation of intracavity cooling and heating processes is of major interest in the present setup. As mentioned in the introduction, proper control of these dynamics is important to achieve sufficient cooling which is mandatory for a proper control of the coupling strength. Cavity cooling and heating processes rely on the absorption and subsequent emission of single photons. Due to energy conservation, cooling and heating is achieved by the emission of frequency shifted photons. The present setup only allows QND measurements of the atomic hyperfine states $|F = 3, 4\rangle$ but no phase or frequency information can be extracted. A different approach is optical heterodyne detection [30], which also facilitates QND measurements but in addition reveals phase and frequency information of the detected photons. In our setup, optical heterodyne spectroscopy is a powerful tool to map intracavity dynamics to the frequency domain. The implementation of this technique allows us to extract several properties, e. g. the intracavity atomic temperature or the heating and cooling rate.

The principle of optical heterodyne detection is simple: One laser beam is split into two beams, a weak probe beam, interacting at frequency ω_p with a sample and a strong local oscillator beam at frequency $\omega_{lo} = \omega_p - \Delta_{p,lo}$. Both beams are combined again and their beat signal is recorded on a photo diode or SPCM. Due to their interference the extraction of phase and frequency information is possible. The detuning $\Delta_{p,lo}$ is usually chosen in the MHz range because these frequencies can be resolved electronically and $1/f$ noise is strongly reduced.

The following subsection describes the implementation of the heterodyne setup into the current experiment and introduces the data acquisition and analysis procedure.

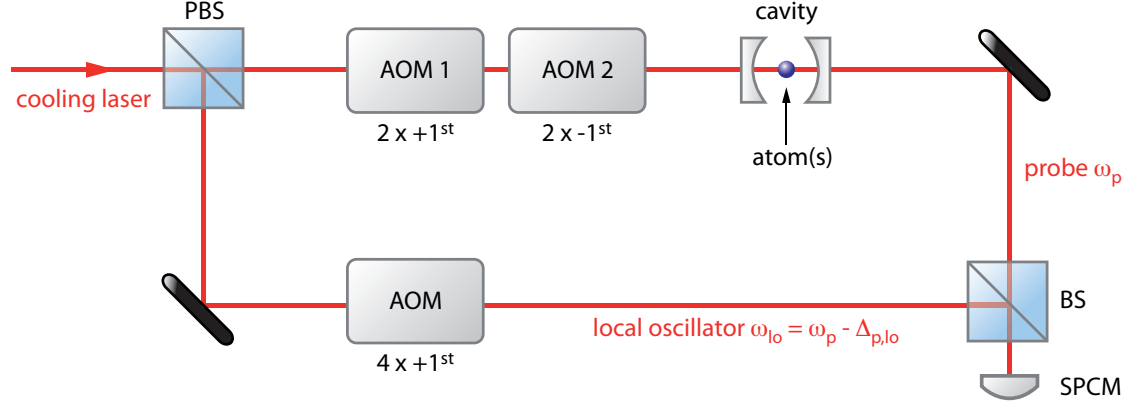


Figure 1.8 – Simplified schematic of the setup for heterodyne detection in the current CQED system. Local oscillator and probe laser are generated by the same source laser and frequency shifted with additional AOMs. The probe laser at frequency ω_p interacts with the atom(s) inside the cavity and is superimposed with the local oscillator at frequency ω_{lo} again. The resulting signal is then recorded with a SPCM.

1.3.1 Experimental setup

A schematic drawing of the optical heterodyne setup is shown in figure 1.8. The cooling laser is used as source for the probe laser and the local oscillator. Its frequency is given by [23]

$$\omega_{cool} = \omega_{44'} + \Delta\omega_d \quad (1.26)$$

with $\Delta\omega_d = 2\pi \cdot 24.90$ MHz. The probe laser is coupled into the high-finesse optical cavity and interacts with single cesium atoms therein. Two AOMs (AOM 1 and 2, see figure 1.8) are used to generate the probe laser frequency. AOM 1 is driven in -1^{st} order and AOM 2 in $+1^{st}$ order double-pass configuration such that the probe laser frequency yields [23]

$$\omega_p = \omega_{44'} + \Delta\omega_d - 2\omega_{AOM\ 1} + 2\omega_{AOM\ 2}. \quad (1.27)$$

Another AOM in a $+1^{st}$ order quadruple pass configuration generates the local oscillator frequency:

$$\omega_{lo} = \omega_{44'} + \Delta\omega_d + 4\omega_{AOM}. \quad (1.28)$$

In order to guarantee high relative frequency stability between the two beams, all AOMs are driven by frequency generators which are in turn connected to a common 10-MHz reference clock. The frequency difference $\Delta_{p,lo}$ between probe laser and local oscillator can be calculated according to eqn. (1.27) and (1.28):

$$\begin{aligned} \Delta_{p,lo} &= \omega_p - \omega_{lo} \\ &= -2\omega_{AOM\ 1} + 2\omega_{AOM\ 2} - 4\omega_{AOM}. \end{aligned} \quad (1.29)$$

1.3. IMPLEMENTATION OF A HETERODYNE DETECTION SCHEME

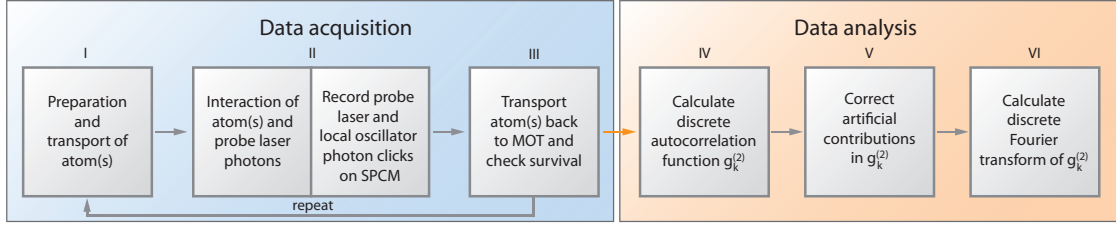


Figure 1.9 – Block diagram of data acquisition and analysis for the heterodyne detection setup.

Both beams, transmitted probe laser and the local oscillator, are again combined using an asymmetric beam splitter (BS, see figure 1.8) which transmits 90 % of the light and reflects only 10 %. Since we do not want to lose any probe laser photons transmitted through the cavity, the probe laser is transmitted while the local oscillator is reflected. The low reflection can be counterbalanced by an increased local oscillator power.

The resulting signal is finally detected as photon clicks on the SPCM. Its output is recorded with a timer card at a time resolution of $\Delta t = 50$ ns (Silicon Solutions, Timer-Card 3.0) resulting in a sampling rate of 20 MHz. In order to obey the Nyquist-Shannon sampling theorem [54, 55], which states that the sampling rate should be at least twice the maximal expected signal frequency, the highest measurable frequency would be 10 MHz. To guarantee proper sampling of the sinusoidally shaped signals, the local oscillator detuning was chosen to be less than 5 MHz. Since $1/f$ noise at low frequencies leads to a distortion of the real signal as well the detuning should still be chosen in the MHz-range. The influence of those effects will be discussed in detail in chapter 2. For our measurements a detuning of $\Delta_{p,lo} = 2\pi \cdot 1$ MHz is sufficient to facilitate a proper sampling rate as well as minor influences of any artifacts.

1.3.2 Measurement procedure and data evaluation

A simplified schematic of the data acquisition and analysis procedure is shown in figure 1.9. The measurement starts with the preparation of single cesium atoms inside the MOT which are subsequently loaded into the DT. If more than one atom was loaded into the DT, the distance between them is checked a posteriori and the data is discarded if the maximum separation exceeds $20 \mu\text{m}$. Otherwise the coupling of the atoms to the cavity mode will be reduced by more than 20 % and will lead to falsified results.

After a successful fit of the atomic position in the recorded fluorescence picture, the optical conveyor belt transports the atom(s) to the center of the cavity mode. For more than one atom, an uncertainty concerning their position still remains because the software usually transports the center of mass of the atoms to the center of the cavity mode leading to a reduced coupling factor.

Once the atoms are transported to the cavity they can interact with the probe laser. All photon clicks caused by local oscillator and transmitted probe laser are detected with

the SPCM. The latter is connected to the timercard which records all clicks. Finally, the atoms are transported back and their survival is checked inside the MOT.

These steps (figure 1.9, I - III) are repeated several times since the atom(s) have only a finite survival time inside the cavity and high statistics is necessary for proper data evaluation. Typical survival times inside the cavity amount to several seconds. For our measurements, we chose a reasonable measurement time of 5 s inside the cavity which provides a good trade-off between atom losses and high data acquisition rates.

Data evaluation is rather complex and consists of several steps (see figure 1.9, IV - VI). Hence, the coarse procedure is introduced now and details are discussed in chapter 2.

First the discrete autocorrelation function $g_k^{(2)}$ of the recorded photon clicks is calculated because the signal we are interested in results from incoherent photon scattering processes which thus possess random phases. Since only one detector is used, artificial effects superimpose the real signal. This problem could have been obviated with the implementation of a second SPCM. Since the expected signal is at the order of the detector dark count rate the signal-to-noise ratio would have been decreased. Instead we developed a routine to eliminate all artificial effects with a reliable recalibration procedure. Their influence and correction will be discussed in detail in the next chapter.

Frequency information of the scattered photons can be extracted from the $g_k^{(2)}$ -function exploiting the Wiener-Khinchin theorem [56, 57]: It states that the discrete Fourier transform (DFT) of the autocorrelation function will result in the power spectral density. Hence, the frequency spectrum is given by the Fourier transform of the discrete $g_k^{(2)}$ -function.

After the introduction into the measurement and analysis procedure, a detailed theoretical description of heterodyne detection follows in chapter 2.

Chapter 2

Theoretical aspects of heterodyne detection

In the following chapter a mathematical description of the heterodyne detection setup which allows the estimation of the signal-to-noise ratio (SNR) is presented. It enables us to choose experimental parameters for efficient measurements and also to test our understanding of the data analysis. Additionally, important improvements in the data analysis procedure, which facilitate the elimination of technical artifacts, namely the afterpulsing effect and the detector dead time, are introduced as well.

The time dependent electric field and intensity are presented first and the analytical autocorrelation function $g^{(2)}(\tau)$ is derived. Furthermore the different expected components of the analytic Fourier spectrum are discussed. After the derivation of the discretized $g^{(2)}$ -function, a detailed discussion on the influence of afterpulsing and the detector dead time follows. Subsequently, the application of the discrete Fourier transform (DFT) is discussed including possible artifacts caused by spectral leakage. Finally, a theoretical estimation of the signal-to-noise ratio is developed and compared to the measurement data.

2.1 Analytical $g^{(2)}$ -function

In order to calculate the analytical $g^{(2)}$ -function, the time dependent electric field and intensity are required. The present heterodyne setup uses the strong local oscillator beam (lo) which is superimposed with the probe laser beam (p) and detected on the SPCM. In addition, the probe laser can interact with the atoms which are trapped along the cavity axis by the lock laser standing wave. Due to the interaction of the probe laser with the atoms, first order sidebands can emerge: Being in some vibrational state $|m\rangle$ of the lock laser potential the probe laser can excite the atom and a subsequent decay can change its vibrational state from $|m\rangle$ to $|m \pm 1\rangle$. This leads to the emission

of frequency shifted photons where the energy difference corresponds to the vibrational energy level spacing. In principle also higher-order transitions, i. e. $|m\rangle \rightarrow |m \pm (2, 3, \dots)\rangle$ are possible but their probability is strongly reduced. A more detailed discussion of the physical mechanism can be found in chapter 3. In this thesis the heterodyne detection scheme is exploited to measure the motional sidebands of vibrational transitions inside the cavity. The sidebands are imprinted in the electric field as additional frequency components. The electric field including all relevant contributions is given by

$$E(t) = E_{\text{lo}}e^{-i\omega_{\text{lo}}t} + E_{\text{p}}e^{-i\omega_{\text{p}}t} + E_{\text{s}} \left(e^{-i(\omega_{\text{p}}+\omega_{\text{ax}})t} + e^{-i(\omega_{\text{p}}-\omega_{\text{ax}})t} \right) + \text{c. c.} \quad (2.1)$$

where E_i denotes the field amplitudes of the local oscillator, the probe laser and the sidebands (s) at the respective frequencies ω_{lo} , ω_{p} and $\omega_{\text{p}} \pm \omega_{\text{ax}}$. Here, ω_{ax} is the transition frequency from vibrational level $|m\rangle$ to $|m \pm 1\rangle$. The intensity can be calculated according to $I = \frac{1}{2}c\epsilon_0|E|^2$. As mentioned in the previous chapter, the SPCM can only resolve frequencies below 10 MHz. Therefore, all terms oscillating at optical frequencies are neglected in the following calculations. For simplicity an equal strength of both sidebands as well as an equal phase is assumed. Experimentally we expect incoherent sideband scattering but we will calculate the autocorrelation function later on, which destroys any phase information. Thus the simplification does not falsify the final results. The intensity then yields

$$\begin{aligned} I(t) = & I_{\text{lo}} + I_{\text{p}} + 2I_{\text{s}} + 2\sqrt{I_{\text{lo}}I_{\text{p}}}\cos[\Delta_{\text{p,lo}}t] \\ & + 2\sqrt{I_{\text{lo}}I_{\text{s}}}\left(\cos[(\Delta_{\text{p,lo}} + \omega_{\text{ax}})t] + \cos[(\Delta_{\text{p,lo}} - \omega_{\text{ax}})t]\right) \\ & + 4\sqrt{I_{\text{p}}I_{\text{s}}}\cos[\omega_{\text{ax}}t] + 2I_{\text{s}}\cos[2\omega_{\text{ax}}t] \end{aligned} \quad (2.2)$$

with the detuning between the local oscillator and probe laser given by $\Delta_{\text{p,lo}} = \omega_{\text{p}} - \omega_{\text{lo}}$. The intensity contains several terms which oscillate at different frequencies. In order to extract all frequency components a Fourier transform of eqn. (2.2) could be performed. The squared absolute value would then result in the power spectral density. Experimentally each measurement trace has a length of $T = 5 \text{ s}$ resulting in $5 \text{ s}/50 \text{ ns} = 10^8$ bins. The large number of time bins demands high computational power for the DFT and should be avoided. Additionally, the photons resulting from sideband transitions possess random phases which leads to an increase of the signal strength with \sqrt{N} only where N denotes the number of scattered photons detected. This can be understood in terms of a two dimensional random walk.

Using the autocorrelation function instead has two advantages: The most interesting frequency component results from the frequency shifted photons which are emitted due to the interaction of the probe laser with the atom at frequencies $\omega_{\text{p}} \pm \omega_{\text{ax}}$. Each vibrational level has a finite lifetime t_{life} . Thus, on the one hand the calculation of the $g^{(2)}(\tau)$ -function up to some maximum correlation time τ_{max} with $T \gg \tau_{\text{max}} \gg t_{\text{life}}$, reduces the computational load. On the other hand, since the random phase is eliminated with the calculation of the autocorrelation function, the signal strength is enhanced and

scales with N in this case. In addition, artificial effects like the detector dead time and the afterpulsing effect can only be corrected if the autocorrelation function is calculated (see section 2.4).

Therefore, we introduce the non-normalized $g^{(2)}(\tau)$ -function, given by

$$g^{(2)}(\tau) = \int_0^T I(t) \cdot I(t + \tau) dt. \quad (2.3)$$

Inserting the intensity from eqn. (2.2) results in

$$\begin{aligned} g^{(2)}(\tau) = T \cdot \{ & (I_{lo} + I_p + 2I_s)^2 + 2I_{lo}I_p \cos[\Delta_{p,lo}\tau] \\ & + 2I_{lo}I_s (\cos[(\Delta_{p,lo} + \omega_{ax})\tau] + \cos[(\Delta_{p,lo} - \omega_{ax})\tau]) \\ & + 8I_pI_s \cos[\omega_{ax}\tau] + 2I_s^2 \cos[2\omega_{ax}\tau] \}. \end{aligned} \quad (2.4)$$

A graphical representation of eqn. (2.4) is shown in figure 2.1 (a) for typical experimental parameters. The intensities of local oscillator I_{lo} and probe laser I_p are usually one to three orders of magnitude higher than the sideband intensity I_s . Therefore, the beating at 1 MHz between local oscillator and probe laser is dominant while the influence of the additional contributions oscillating at $\Delta_{p,lo} \pm \omega_{ax}$, ω_{ax} and $2\omega_{ax}$ is apparent as amplitude variations of the $g^{(2)}$ -function.

2.2 Analytical spectrum of the $g^{(2)}$ -function

The previous section showed that the extraction of all frequency components in the $g^{(2)}$ -function is possible with the application of the Fourier transform. As introduced in chapter 1, the Wiener-Khinchin theorem states that the Fourier transform of the autocorrelation function yields the power spectral density. Therefore, its application to eqn. (2.4) reveals the frequency spectrum of the measurement. The result yields

$$\begin{aligned} FT(g^{(2)}(\tau))(\omega) &= \frac{1}{\sqrt{2\pi}} \int_{-\infty}^{+\infty} g^{(2)}(\tau) e^{-i\omega\tau} d\tau \\ &= \sqrt{2\pi} \cdot T \cdot \left\{ [I_{lo} + I_p + 2I_s]^2 \cdot \delta_0 + I_{lo}I_p [\delta_{\Delta_{p,lo}} + \delta_{-\Delta_{p,lo}}] \right. \\ &\quad + I_{lo}I_s [\delta_{-[\Delta_{p,lo} + \omega_{ax}]} + \delta_{[\Delta_{p,lo} + \omega_{ax}]} + \delta_{-[\Delta_{p,lo} - \omega_{ax}]} + \delta_{[\Delta_{p,lo} - \omega_{ax}]}] \\ &\quad \left. + 4I_pI_s [\delta_{-\omega_{ax}} + \delta_{\omega_{ax}}] + I_s^2 [\delta_{-2\omega_{ax}} + \delta_{2\omega_{ax}}] \right\}. \end{aligned} \quad (2.5)$$

Here, δ_α denotes the Dirac delta distribution $\delta(\omega - \alpha)$. A graphical representation of the positive frequency components for typical experimental parameters can be found in figure 2.1 (b). The Fourier spectrum results from different contributions: A strong peak occurs at $\omega = 0$ (DC-peak) which is represented by the first term. It usually

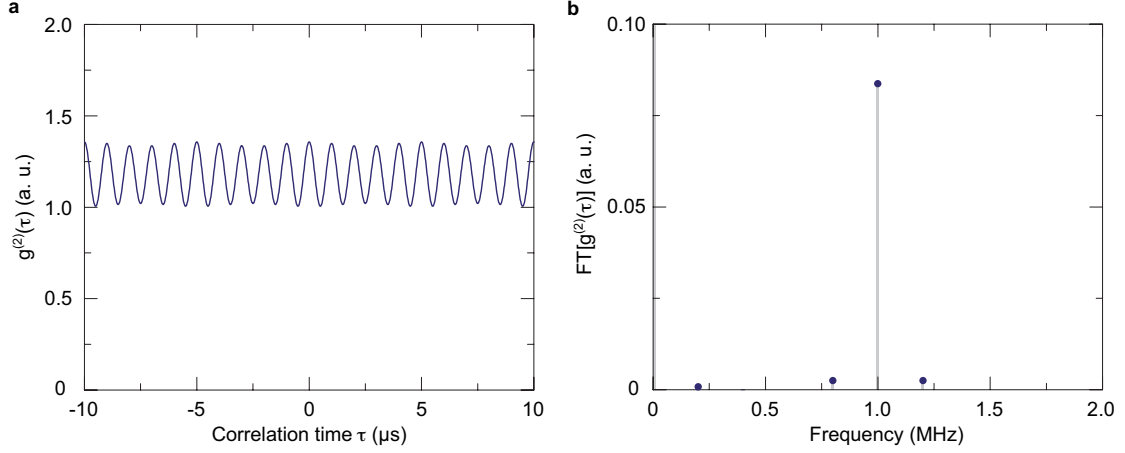


Figure 2.1 – (a) Exemplary $g^{(2)}$ function obtained from eqn. (2.4) for typical ratios of $I_p/I_{l_0} = 1/12$ and $I_s/I_{l_0} = 1/400$, $\Delta_{p,l_0} = 2\pi \cdot 1$ MHz and $\omega_{ax} = 2\pi \cdot 200$ kHz. I_{l_0} was arbitrarily set to $1 \text{ mW}/\text{cm}^2$ and T to 1 s. (b) Corresponding frequency spectrum with a strong peak at $\omega/(2\pi) = 0$ MHz, the beat signal between probe laser and local oscillator at 1 MHz and the sidebands at 0.8 MHz and 1.2 MHz. The small contribution at 0.2 MHz is hardly visible whereas the peak at 0.4 MHz vanishes at this plot range due to its weak intensity.

dominates all other contributions because the local oscillator intensity is chosen one order of magnitude larger than the probe laser intensity (here: $I_p/I_{l_0} \approx 1/12$) and the signal strength is always smaller than the probe laser intensity itself (here: $I_s/I_p = 1/32$). In addition, the so called carrier oscillating at the beat frequency between local oscillator and probe laser Δ_{p,l_0} exhibits a strength proportional to both intensities. In the spectrum, this peak is the second highest and occurs at 1 MHz which is a typical value for the chosen detunings.

The signal in frequency domain results from the frequency shifted photons as mentioned above. In figure 2.1 $\omega_{ax} = 2\pi \cdot 200$ kHz and thus the two peaks around the carrier, the so called *sidebands*, correspond to the desired signal we would like to measure. In contrast to the DC-peak and the carrier it is rather small because usually $I_s \ll (I_{l_0}, I_p)$ which explains why only a small contribution from this term is expected although the local oscillator can enhance its strength. A further contribution can be seen at ω_{ax} and the one expected at $2\omega_{ax}$ is already too small to be resolved in the plot. Nevertheless, the plot emphasizes that the expected sidebands can easily be buried in noise and a comprehension of the dependencies of the SNR is desirable.

The next section takes into account that all measurement results are discrete and a discretized expression for the $g^{(2)}$ -function is introduced.

2.3 Discretized $g^{(2)}$ -function

All calculations so far were based on intensities but the SPCM measures count rates, i. e. it detects single photon clicks. Therefore, the intensity has to be expressed in terms of the count rates n_l with $l = (\text{lo}, \text{p}, \text{s})$. The relation between these two quantities is given by

$$I_l = \frac{P_l}{A} = \frac{N_l \hbar \omega_l}{\Delta t A} = \frac{n_l \hbar \omega_l}{A} \quad (2.6)$$

with the number of photons N_l within the time interval Δt (corresponding to the time resolution of the timer card in the setup), the effective detector area A and the frequency ω_l of the photons. Since A can be assumed to be constant and the frequencies of the local oscillator, probe laser and sideband photons ω_l are approximately equal as well, we can write

$$I_l = \text{const.} \cdot n_l. \quad (2.7)$$

Hence, the intensity is directly proportional to the count rates n_l . Experimentally we detect photon clicks in a defined time interval Δt . In each time bin q the mean photon number equals the product of the photon count rate times Δt . According to eqn. (2.2) the number of photon clicks R_q in each bin q is given by

$$\begin{aligned} R_q = \Delta t & (n_{\text{lo}} + n_{\text{p}} + 2n_{\text{s}} + 2\sqrt{n_{\text{lo}}n_{\text{p}}}\cos[\Delta_{\text{p,lo}} \cdot q\Delta t] \\ & + 2\sqrt{n_{\text{lo}}n_{\text{s}}}\cos[(\Delta_{\text{p,lo}} + \omega_{\text{ax}}) \cdot q\Delta t] + \cos[(\Delta_{\text{p,lo}} - \omega_{\text{ax}}) \cdot q\Delta t]) \\ & + 4\sqrt{n_{\text{p}}n_{\text{s}}}\cos[\omega_{\text{ax}} \cdot q\Delta t] + 2n_{\text{s}}\cos[2\omega_{\text{ax}} \cdot q\Delta t]). \end{aligned} \quad (2.8)$$

In the experiment the photon detector (SPCM) can only detect one photon per bin. Since the count rate is well below one photon per bin, we may still use count rates for the mathematical description. The discrete $g^{(2)}$ -function can be calculated replacing the integration by a summation over all measurement bins q

$$\begin{aligned} g_k^{(2)} &= \sum_{q=0}^{N_{\text{t}}-N_{\text{f}}} R_q \cdot R_{q+k} \\ &\stackrel{(2.4)}{=} (N_{\text{t}} - N_{\text{f}}) \cdot \Delta t^2 \cdot \left((n_{\text{lo}} + n_{\text{p}} + 2n_{\text{s}})^2 + 2n_{\text{lo}}n_{\text{p}}\cos[\Delta_{\text{p,lo}} \cdot k\Delta t] \right. \\ &\quad + 2n_{\text{lo}}n_{\text{s}}(\cos[(\Delta_{\text{p,lo}} + \omega_{\text{ax}}) \cdot k\Delta t] + \cos[(\Delta_{\text{p,lo}} - \omega_{\text{ax}}) \cdot k\Delta t]) \\ &\quad \left. + 8n_{\text{p}}n_{\text{s}}\cos[\omega_{\text{ax}} \cdot k\Delta t] + 2n_{\text{s}}^2\cos[2\omega_{\text{ax}} \cdot k\Delta t] \right) \end{aligned} \quad (2.9)$$

with the total number of measurement bins $N_{\text{t}} = T/\Delta t$ and the total measurement time T . $g_k^{(2)}$ gives the correlations between the signal with itself at a distance of $k = \tau/\Delta t$ bins. For the measured data, the discrete values $g_k^{(2)}$ are calculated up to some maximum

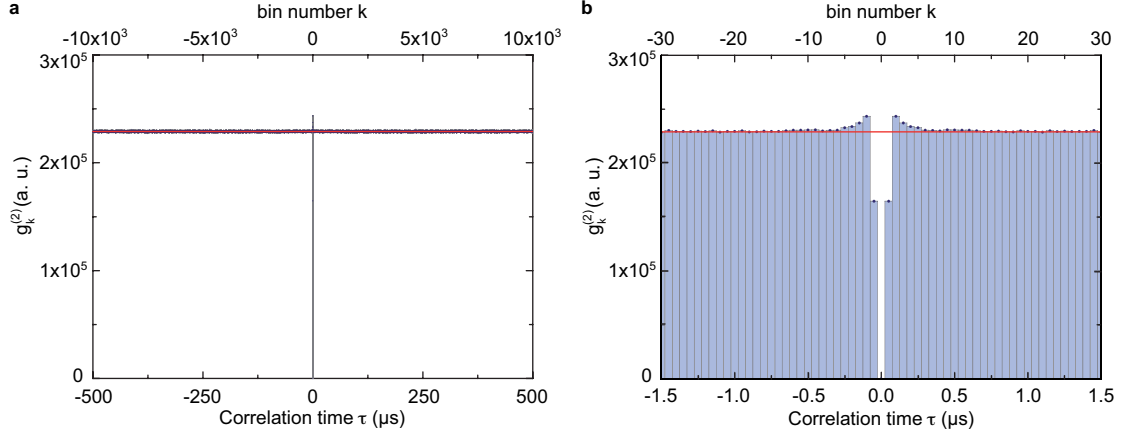


Figure 2.2 – (a) Exemplary $g^{(2)}$ data trace (blue) for a local oscillator count rate of $n_{l_o} = 2.2 \cdot 10^5$ counts/s ($n_p = 0$) and a total measurement time $T = 100$ s calculated for a maximal correlation time of $\tau_{\max} = 500 \mu\text{s}$ in comparison to the theoretical expectation according to eqn. (2.9) (red line). (b) Close up of (a): The effect of afterpulsing manifests itself as artificial increase of correlations at correlation times smaller 250 ns. The detector dead time leads to the reduction of the correlation in bin $k = \pm 1$. Furthermore due to the single detector setup no information is available for $g_0^{(2)}$.

bin $k = N_f$ which relates to the maximum correlation time τ_{\max} as $N_f = \tau_{\max}/\Delta t$. N_f is therefore the maximum correlation time expressed in bin sizes. The sum in eqn. (2.9) runs only up to $N_t - N_f$ due to the limitation by the maximum correlation time τ_{\max} : If $g_{k=N_f}^{(2)}$ for the maximum correlation bin N_f is calculated, the value for $q + k$ may not exceed N_t . Thus the maximum value for q is given by $N_t - N_f$. In general it holds $N_f \ll N_t$ because all correlations vanish on short timescales ($< 500 \mu\text{s}$). Nevertheless, summing up to N_t would lead to a visible decrease of the $g^{(2)}$ -function with increasing correlation bin k .

For further data analysis with the DFT a symmetric $g^{(2)}$ -function is desirable. Therefore, we exploit that $g_k^{(2)} = g_{-k}^{(2)}$ and generate all negative values with their positive counterpart.

2.4 Influence of afterpulsing and detector dead time

The idealized discrete $g^{(2)}$ -function is now compared to real measurement data and enables us to identify possible technical effects which superimpose the real signal. In figure 2.2, the expected result according to eqn. (2.9) is displayed for a measurement with the local oscillator only (i. e. $n_{l_o} = 2.2 \cdot 10^5$ counts/s) (red) and compared to real measurement data (grey/blue). Besides noise contributions, which always overlay the data, theoretical and experimental results agree well for correlation times greater than 500 ns. For smaller correlation times, an artificial increase of the $g^{(2)}$ -function as well as a drop at $g_0^{(2)}$ and $g_{\pm 1}^{(2)}$ is clearly visible which results from the imperfect detection scheme. Since all measurements are performed with a single detector (SPCM) the detector dead

time as well as the afterpulsing effect have to be taken into account. Both effects are extensively discussed in literature, e. g. [58–62]. Here, we would like to pursue a practical approach to correct both effects in our setup.

The afterpulsing effect describes the phenomenon that an artificial click, which is caused by some residual charge carriers in the SPCM, is created. The origin lies in the internal structure of the SPCM: It usually consists of a photo multiplier tube or a silicon APD. The latter is used in our SPCM. Here, an impinging photon usually triggers a subsequent avalanche of ionizations resulting in the desired signal (click). Nevertheless it may happen, that single charge carriers are trapped in the junction depletion layer of the semiconductor [61]. Thermal excitation can lead to their release creating a charge carrier which can trigger a second click [59]. This phenomenon is called *afterpulsing* and leads to an artificially increased count rate. For a perfect detector, the number of correlations in each bin k of the $g^{(2)}$ -function is given by

$$g_k^{(2)} = \frac{N_{\text{tot}}^2}{N_t} = N_{\text{tot}} n_{\text{tot}} \Delta t, \quad (2.10)$$

where N_{tot} denotes the total number of detected photons during the measurement time T . Due to the afterpulsing, the relation for $g_k^{(2)}$ has to be modified. The probability to detect a correlation is given by the sum of the probabilities p_r and p_a to count a correlation due to a real and an artificial click, respectively. Since the product of detected count rate times bin size $n_{\text{tot}} \cdot \Delta t$ is much smaller than one we can relate the probabilities to the count rate as follows

$$n_{\text{tot}} \Delta t = (p_r + p_a). \quad (2.11)$$

Furthermore, we have to take into account that the probability to detect a correlation due to an afterpulsing photon will decrease for higher $|k|$ in the $g^{(2)}$ -function. We hence introduce a k -dependent afterpulsing probability $p_{a,k}$. The modified autocorrelation function then reads

$$\begin{aligned} g_k^{(2)} &= N_{\text{tot}}(p_r + p_{a,k}) \\ &= N_{\text{tot}}(n_r \Delta t + p_{a,k}), \end{aligned} \quad (2.12)$$

where n_r is the real photon count rate which is of interest. The effect of afterpulsing can be visualized if the probe beam is blocked and the local oscillator is recorded only. The corresponding $g^{(2)}$ -function in figure 2.2 reveals the effect for $|k| \geq 2$: Without afterpulsing the autocorrelation function should be completely flat (red). As expected the number of correlations is artificially increased for small $|k|$ and hardly any influence of the afterpulsing is visible for high $|k|$.

In order to correct the afterpulsing we pursue the following approach: The SPCM's dark count rate of $n_d = 500$ counts/s was recorded for 20 hours. The dark count rate was chosen instead of the local oscillator since possible bunching or antibunching effects

can superimpose the afterpulsing effect leading to a falsified correction. From the dark count data the corresponding autocorrelation function $g_{d,k}^{(2)}$ is calculated. Subsequently, the mean value $\langle g_d^{(2)} \rangle$ is subtracted from $g_{d,k}^{(2)}$. Otherwise, a subtraction from the original data would eliminate the DC-term of the original data. Additionally, a renormalization factor $N_{\text{tot}}/N_{\text{tot,d}}$ is introduced because the real and dark count measurement have different measurement times and thus different total photon numbers N_{tot} and $N_{\text{tot,d}}$. The afterpulsing-corrected autocorrelation function $g_{\text{cor},k}^{(2)}$ finally yields

$$g_{\text{cor},k}^{(2)} = g_k^{(2)} - \left(g_{d,k}^{(2)} - \langle g_d^{(2)} \rangle \right) \cdot \frac{N_{\text{tot}}}{N_{\text{tot,d}}}. \quad (2.13)$$

The prevention of additional noise in the measurement data, which can lead to a reduced SNR, is of major interest. Therefore, the total dark count photon number $N_{\text{tot,d}}$ for the calculation of $g_{d,k}^{(2)}$ is chosen at least a factor of two or three higher than the measured photon number N_{tot} . In the present setup usual measurement times are on the order of several seconds and the available dark count data of several hours is sufficiently high to assure no additional noise contamination caused by the described correction procedure.

Besides the afterpulsing, a further effect stands out in figure 2.2 (b): The decreased values $g_{\pm 1}^{(2)}$ result from the detector dead time t_{dead} since the photon detection is realized with a single detector only. The measured value for t_{dead} is approximately 30 ns. We have measured that the influence in the second bin of $g^{(2)}$ is at the order of 3 % only and is thus negligible. Therefore, the dead time effect mainly affects the first bin of the autocorrelation function. Due to the detector dead time the number of correlations in the first bin is too small compared to their original value. Nevertheless we are able to correct this artifact for the bins $k = \pm 1$ if we take the detector dead time coefficient d_1 into account and modify eqn. (2.12) accordingly

$$g_1^{(2)} = N_{\text{tot}} d_1 (n_r \Delta t + p_{a,1}). \quad (2.14)$$

The numerical value for d_1 can be determined experimentally: Recording the local oscillator without the probe laser for different count rates n_{tot} and calculating the $g^{(2)}$ -function for each count rate enables us to plot $g_1^{(2)}/N_{\text{tot}}$ versus the count rate times the bin time $n_r \cdot \Delta t$ (see figure 2.3 (a)). The count rate n_r can be extracted from the $g^{(2)}$ -function again because for high $|k|$ the afterpulsing probability as well as the detector dead time are negligible and $g_k^{(2)} = N_{\text{tot}} n_r \Delta t$ for $|k| \gg 1$. A linear fit according to eqn. (2.14) reveals a value of 0.57 ± 0.01 for d_1 . The dead time effect can be successfully eliminated if $g_{\pm 1}^{(2)}$ is divided by d_1 .

A third artificial effect arises at $k = 0$ resulting once again from the fact that only one detector is used: No information exists about $g_0^{(2)}$ and its value is therefore zero. A detailed analysis of the Fourier spectra indicated that this dip has a major influence on the spectrum and a correction is desirable. The theoretical calculations suggest that $g_0^{(2)}$ has almost the same value as $g_1^{(2)}$. Therefore $g_0^{(2)}$ was set to the value of $g_1^{(2)}$ which

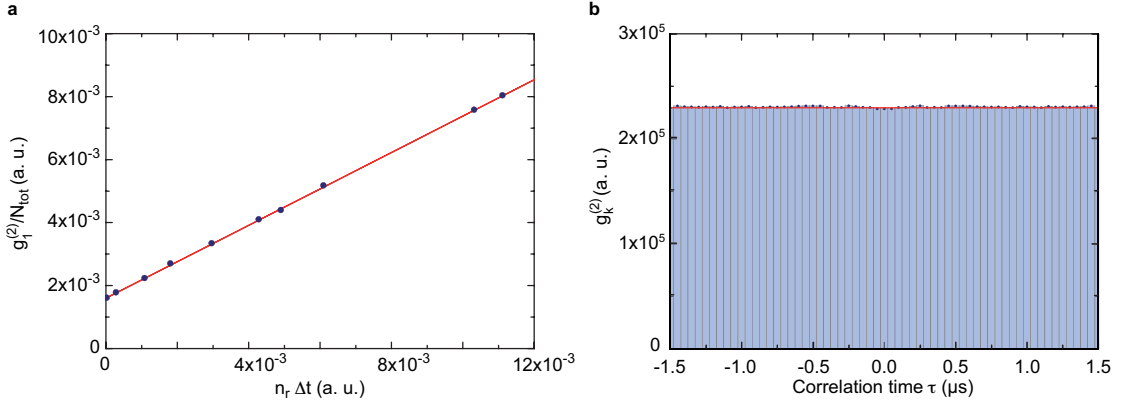


Figure 2.3 – (a) The normalized value of the first bin of the $g^{(2)}$ -function is plotted versus the local oscillator photon count rate times the bin time $n_r \cdot \Delta t$. This allows the extraction of the detector dead time coefficient d_1 from the linear fit function (for details, see text). (b) Same $g^{(2)}$ -function as in figure 2.2 (b) with corrected effects of afterpulsing and detector dead time. In addition, $g_0^{(2)}$ was set to the value of $g_1^{(2)}$. The red line denotes the theoretical expectation as in figure 2.2.

matches the theoretical expectations reasonably well and eliminates nonphysical effects in the spectrum.

To conclude, all three technical effects were eliminated leading to the corrected $g^{(2)}$ -function as shown in figure 2.3 (b) which agrees well with the theoretical expectation.

2.5 The discrete Fourier transform

The analytical calculation of the DFT of $g_k^{(2)}$ demands a discretization of the frequencies as well. Therefore, all frequencies ω will be rewritten in terms of multiples of the smallest frequency Δf which can be resolved. Hence, we can write

$$\omega \rightarrow 2\pi j\omega \Delta f \quad \text{with } j\omega \in \mathbb{Z}, \quad (2.15)$$

where $\Delta f = \frac{1}{2N_f \Delta t}$ with the total number of frequency bins $2N_f$ which are used for the Fourier transform later on. The $g^{(2)}$ -function given in eqn. (2.9) can be rewritten again using the expressions for ω , Δf and N_t :

$$\begin{aligned} g_k^{(2)} = T\Delta t \left\{ (n_{lo} + n_p + 2n_s)^2 + 2n_{lo}n_p \cos \left[2\pi j\Delta_{p,lo} \frac{k}{2N_f} \right] \right. \\ \left. + 2n_{lo}n_s \left(\cos \left[2\pi j(\Delta_{p,lo} + \omega_{ax}) \frac{k}{2N_f} \right] + \cos \left[2\pi j(\Delta_{p,lo} - \omega_{ax}) \frac{k}{2N_f} \right] \right) \right. \\ \left. + 8n_p n_s \cos \left[2\pi j\omega_{ax} \frac{k}{2N_f} \right] + 2n_s^2 \cos \left[2\pi j2\omega_{ax} \frac{k}{2N_f} \right] \right\}. \end{aligned} \quad (2.16)$$

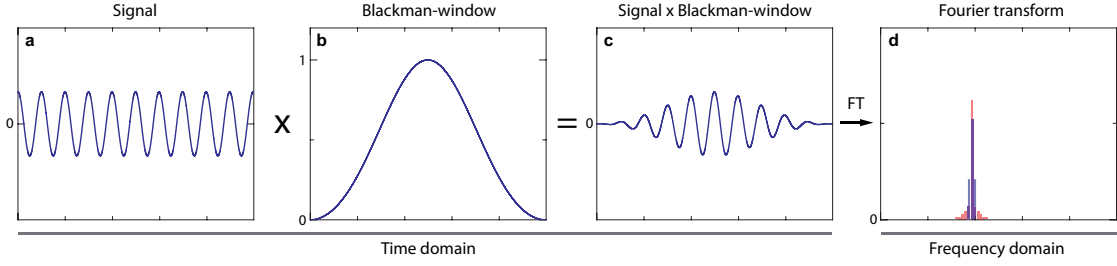


Figure 2.4 – Exemplary schematic for the application of window functions: First, the original data set (a) is multiplied with the Blackman-window (b) in time domain. The discrete Fourier transform is then applied to the resulting function (c), which gives the desired output in frequency domain (d) without the effect of spectral leakage (blue). The application of the DFT to the periodic function in (a) would lead to spectral leakage (red).

The discrete Fourier transform of $g_k^{(2)}$ then reads [63]

$$\begin{aligned}
 F_j &= \frac{1}{2N_f} \sum_{k=-N_f}^{N_f-1} g_k^{(2)} e^{-2\pi i j k / (2N_f)} \\
 &= \frac{1}{2N_f} \sum_{k=-N_f}^{N_f-1} g_k^{(2)} \{ \cos [2\pi j k / (2N_f)] - i \sin [2\pi j k / (2N_f)] \}.
 \end{aligned} \tag{2.17}$$

The summation runs from $-N_f$ to $N_f - 1$ to guarantee a periodic continuation and avoid inadvertent effects in the Fourier spectrum. Since our $g^{(2)}$ -function is symmetric around $g_0^{(2)}$ the imaginary part of the Fourier transform vanishes and only the real part has to be calculated.

Purpose of window functions The DFT can also cause additional artifacts and a careful application is inevitable. Since every time series spans over a finite time window, abrupt steps at the beginning and at the end break the periodicity and entail unwanted spectral contributions. The discrete Fourier transform of a time series, which includes a periodic signal at frequency ω , will reveal artificial effects, namely *spectral leakage* [63]. In principle the Fourier spectrum should only contain a non-zero value at ω but due to spectral leakage, sidelobes arise and neighbouring frequency bins will also contain non-zero values. If the spectrum of the measured data consist of unequally strong components which are spectrally close together, it might happen that the weaker signal (here the sidebands) is buried in the sidelobes of the stronger (here the carrier). Window functions can be used to circumvent this effect. Their application is simple since they only have to be multiplied with the original data set (see figure 2.4). In literature [64, 65] a variety of window functions for different applications is available. Two parameters usually exclude each other, namely high frequency resolution and high suppression of spectral leakage. The latter can only be achieved at the expense of frequency resolution. Therefore, one needs to find an appropriate trade-off between both parameters. We decided to choose

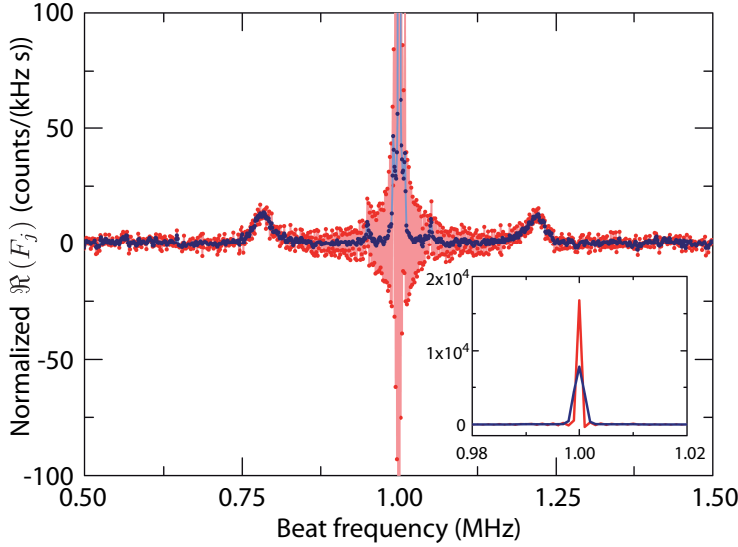


Figure 2.5 – Comparison of the real part of the Fourier spectrum of the measurement data calculated without (red) and with (blue) the Blackman-window function. The latter suppresses spectral leakage of the carrier while the broadening introduced due to the application of the window remains reasonably small (see inset).

the Blackman-window, because it exhibits a sidelobe-suppression of -58 dB while the 3 dB-bandwidth (equivalent to the full width at half maximum (FWHM)) is 1.68 bins [65]. For comparison, the intrinsic window function, resulting from the finite time series, is always present in the data: the rectangular window. It possesses the highest resolution, i. e. a 3 dB-bandwidth of 0.88 bins [64] but the suppression is only -13 dB. The Blackman-window function used is given by [65]

$$w_{k,\text{blck}} = a_0 + a_1 \cos \left[\frac{2\pi}{2N_f} k \right] + a_2 \cos \left[\frac{2\pi}{2N_f} 2k \right] \quad (2.18)$$

where $a_0 = 0.42, a_1 = 0.50, a_2 = 0.08$.

The modified autocorrelation function then yields

$$g_{k,\text{win}}^{(2)} = w_{k,\text{blck}} \cdot g_k^{(2)}. \quad (2.19)$$

The enhancement achieved with the application of a window function becomes apparent in figure 2.5. It shows the real part of the discrete Fourier spectrum of the measured data between 0.5 and 1.5 MHz calculated with and without Blackman-window for a total measurement time $T = 280$ s and a maximum correlation time $\tau_{\text{max}} = 500 \mu\text{s}$. Here, the effect of spectral leakage becomes evident: The carrier at 1 MHz is very pronounced and sidebands at 0.8 and 1.2 MHz are visible as well. Weak sidelobe suppression is seen for the original data without Blackman-window (figure 2.5, red). The corresponding carrier peak is narrow (fig. 2.5, inset, red) but both branches are spectrally broadened and energy 'leaks' to adjacent frequency bins, slightly superimposing both sidebands. In contrast, the high suppression of the Blackman-window leads to an excellent suppression of spectral leakage while the broadening of the peak itself remains reasonable (figure 2.5, blue). Additionally, spectral leakage can also lead to a redistribution of power between

real and imaginary part. This explains the artifact of the negative values in the real part of the spectrum around 1 MHz.

2.6 Estimation of the signal-to-noise ratio

Since all technical artificial effects and their elimination were discussed in the previous sections, it is of major interest to identify the different dependencies of the measured signal and its noise. Therefore, an analytical estimation of the signal-to-noise ratio in the Fourier spectrum is developed and compared to real measurements. For an estimation we hypothesize that the noise is exclusively determined by the shot noise of the local oscillator, probe laser, sideband and dark count photons. In this case, the probability $P_k(x)$ to find x clicks in bin k of $g_k^{(2)}$ is given by the Poisson distribution

$$P_k(x) = \frac{\lambda^x}{x!} e^{-\lambda} \quad (2.20)$$

with the expectation value λ which can be calculated as follows: The count rate $n_{\text{tot}} = n_{\text{lo}} + n_{\text{p}} + 2n_{\text{s}} + n_{\text{d}}$ for the contributions mentioned above is constant. All oscillating terms of eqn. (2.8) are on average zero and can thus be neglected. The total number of photons measured is then given by $N_{\text{tot}} = n_{\text{tot}}T$ and the expectation value in each bin k of the $g^{(2)}$ -function yields

$$\lambda = g_k^{(2)} = \sum_{q=0}^{N_t} \frac{N_{\text{tot}}^2}{N_t^2} = \frac{N_{\text{tot}}^2}{N_t} = \frac{(n_{\text{tot}}T)^2}{N_t} \quad (2.21)$$

with the total number of measurement bins N_t ¹. The expression can be simplified using $N_t = T/\Delta t$:

$$\lambda = \frac{(n_{\text{tot}}T)^2}{T/\Delta t} = n_{\text{tot}}^2 T \Delta t \quad (2.22)$$

and the result is equal to the constant term of eqn. (2.9). Since a Poisson distribution was assumed, the variance is given by λ as well. Thus, the standard deviation for each $g_k^{(2)}$ is $\sqrt{\lambda}$. The Fourier coefficients F_j are given by eqn. (2.17) and their error will be estimated next. Due to the intrinsic symmetry of the $g^{(2)}$ -function around $g_0^{(2)}$ the imaginary part of each Fourier component is zero and the investigation can be limited to the real part only. The latter is given by

$$\Re(F_j) = \frac{1}{2N_f} \sum_{k=-N_f}^{N_f-1} g_k^{(2)} \cos \left[2\pi \frac{jk}{2N_f} \right] \quad (2.23)$$

$$\approx \frac{2}{2N_f} \sum_{k=0}^{N_f-1} g_k^{(2)} \cos \left[2\pi \frac{jk}{2N_f} \right]. \quad (2.24)$$

¹For this estimation we assume $N_t \approx N_t - N_f$ and $N_t + 1 \approx N_t$

Here, the last equation holds due to the symmetry of the $g^{(2)}$ -function: The data for $g_k^{(2)}$ with $k < 0$ is generated by duplication of the data from the corresponding $g_k^{(2)}$ with $k > 0$. In addition, the approximation was introduced because $g_0^{(2)}$ will be taken twice and $g_{-N_f}^{(2)}$ will be neglected. For the estimation of the error we may assume that all $g_k^{(2)}$ with $k \geq 0$ contribute equally to each F_j . Therefore, the approximation is still valid. The expected error can be calculated using Gaussian error propagation

$$\begin{aligned}
 \Delta [\Re(F_j)] &= \frac{1}{N_f} \sqrt{\sum_{k=0}^{N_f-1} \left(\Delta g_k^{(2)} \cos \left[2\pi \frac{j}{2N_f} k \right] \right)^2} \\
 &= \frac{1}{N_f} \sqrt{\sum_{k=0}^{N_f-1} \left(\sqrt{\lambda} \cos \left[2\pi \frac{j}{2N_f} k \right] \right)^2} \\
 &= \frac{n_{\text{tot}} \sqrt{\Delta t T}}{N_f} \sqrt{\sum_{k=0}^{N_f-1} \cos^2 \left[2\pi \frac{j}{2N_f} k \right]} \\
 &= n_{\text{tot}} \sqrt{\frac{\Delta t T}{2N_f}} \\
 &= n_{\text{tot}} \Delta t \sqrt{\frac{T}{2\tau_{\text{max}}}}.
 \end{aligned} \tag{2.25}$$

As a next step, the expected signal strength in the Fourier spectrum is estimated. The signal is given by the sidebands around the carrier, which spread over several frequency bins. In order to estimate the SNR the broadening will lead to a decreased signal strength which is taken into account in further considerations (see below). The contribution of the right sideband to the $g^{(2)}$ -function can be extracted from eqn. (2.16) as

$$g_{k,s}^{(2)} = 2n_{\text{lo}}n_s\Delta tT \cos \left[2\pi j_s \cdot \frac{k}{2N_f} \right] \tag{2.26}$$

with $j_s = j_{\Delta_{\text{p,lo}} + \omega_{\text{ax}}}$ under the assumption that the frequency ($\Delta_{\text{p,lo}} + \omega_{\text{ax}}$) can be expressed as a multiple of Δf . In this case the signal will contribute to one bin in the Fourier spectrum only which is desirable for the analytical analysis. According to eqn. (2.17) the real part of the discrete Fourier transform yields

$$\begin{aligned}
 \Re(F_{j=j_s}) &= \frac{1}{2N_f} \sum_{k=-N_f}^{N_f-1} 2n_{\text{lo}}n_s\Delta tT \cos \left[2\pi j_s \cdot \frac{k}{2N_f} \right] \cdot \cos \left[2\pi j \cdot \frac{k}{2N_f} \right] \\
 &= 2n_{\text{lo}}n_s\Delta tT \frac{1}{2N_f} \sum_{k=-N_f}^{N_f-1} \cos^2 \left[2\pi j_s \cdot \frac{k}{2N_f} \right] \\
 &= 2n_{\text{lo}}n_s\Delta tT \frac{1}{2N_f} \left(\frac{2N_f}{2} \right) \\
 &= n_{\text{lo}}n_s\Delta tT
 \end{aligned} \tag{2.27}$$

for the positive frequency component. The negative frequency component at $-j_s$ will give the same result because $\cos(j_s) = \cos(-j_s)$. Multiplying the result by a factor of two will thus give the single sided spectrum of the real part of the Fourier transform of the $g^{(2)}$ -function.

As already mentioned above the measured signal in Fourier domain is usually broadened and has a certain spread over several bins j . This is mainly caused by three reasons: First of all, the vibrational state has a certain lifetime which leads to spectral broadening. Second, the atoms are trapped in a sinusoidal potential which has unequally spaced adjacent energy levels and thus photons resulting from transitions between the vibrational states $|m\rangle \rightarrow |m \pm 1\rangle$ have a frequency which depends on m . This effect leads to a broadening in frequency domain as well. Furthermore the atom is only weakly confined along the x -direction which introduces additional broadening as well. A detailed discussion of different broadening mechanisms follows in chapter 3. Here, we take them into account by equally spreading the signal over several bins introducing a scaling factor $\Delta f/S_W$ with the frequency resolution Δf and the signal width S_W . Due to the Wiener-Khinchin theorem, which states that the Fourier transform of the autocorrelation function gives the power spectral density, the signal can be spread over several bins. The modified signal is given by

$$\Re(F'_{j_s}) = n_{lo}n_s\Delta t T \frac{\Delta f}{S_W} \quad \text{with } j_s = j_{\Delta p, lo+\omega_{ax}} - \frac{S_W}{2\Delta f}, \dots, j_{\Delta p, lo+\omega_{ax}} + \frac{S_W}{2\Delta f}. \quad (2.28)$$

Finally, the SNR can be calculated with eqns. (2.25) and (2.28):

$$\text{SNR} = \frac{\Re(F'_{j_s})}{\Delta[\Re(F_j)]} = \frac{n_{lo}n_s\Delta t T \Delta f}{n_{tot}\Delta t \sqrt{\frac{T}{2\tau_{max}}} S_W} \quad (2.29)$$

with $\Delta f = \frac{1}{2N_f\Delta t}$ and $N_f = \frac{\tau_{max}}{\Delta t}$ this equation simplifies to

$$\begin{aligned} \text{SNR} &= \frac{n_{lo}n_s T}{n_{tot} \sqrt{\frac{T}{2\tau_{max}}} 2N_f \Delta t S_W} \\ &= \frac{n_{lo}n_s T}{n_{tot} \sqrt{\frac{T}{2\tau_{max}}} 2\tau_{max} S_W} \\ &= \frac{n_{lo}}{n_{tot}} \cdot \frac{n_s}{S_W} \cdot \sqrt{\frac{T}{2\tau_{max}}}. \end{aligned} \quad (2.30)$$

As expected the result indicates that the SNR can be improved with increasing measurement time. In addition, it also depends on the different count rates n_l with $l = (lo, p, s, d)$. The first factor suggests that high local oscillator count rates are desirable since then this factor will trend towards unity. Typical parameters in our case are listed in table 2.1.

Table 2.1 – Experimental count rates.

CONTRIBUTION	COUNT RATE	EXPERIMENTAL VALUE (COUNTS/S)
local oscillator	n_{lo}	$1.64 \cdot 10^5$
probe laser	n_{p}	$1.60 \cdot 10^4$
sideband signal	n_{s}	$0.05 \cdot 10^4$
dark count rate	n_{d}	$0.05 \cdot 10^4$

These values result in a ratio of $n_{\text{lo}}/n_{\text{tot}} = 0.91$. If the local oscillator count rate is doubled the ratio would only increase up to 0.95. Therefore, n_{lo} is already chosen sufficiently high in the current setup and a further increase would not have a considerable effect on the SNR. Decreasing the probe laser count rate n_{p} would not increase the SNR because n_{s} also depends on n_{p} and would decrease as well.

In addition, the SNR also depends on τ_{max} . In principle this parameter can be chosen arbitrarily small but the resolution of the Fourier spectrum depends also on τ_{max} since $\Delta f = 1/(2\tau_{\text{max}})$. Thus a reduction in τ_{max} would lead to a better signal-to-noise ratio but the frequency resolution would be decreased as well. For each purpose, this effect should be taken into account to find a good trade-off between resolution and proper SNR.

Since all calculations are based on the assumption of shot noise in the recorded signal we would like to compare the theoretical estimation with experimentally measured data in the following section.

2.7 Verification of estimated signal-to-noise ratio

We now pursue a detailed comparison of theoretical and experimental results focusing on possible deviations from the expected SNR. For the following analysis we followed the measurement procedure for heterodyne detection as described in chapter 1, limited to one atom inside the cavity only. All artificial effects were eliminated, following the recalibration procedure described in section 2.4. The DFT was performed without the Blackman-window function because its effect was not considered in the previous noise analysis.

First, eqn. (2.25) shall be verified: In order to calculate the error $\Delta [\Re(F_j)]$ of each real Fourier component in the measured spectrum, the variance

$$\sigma^2 = \frac{1}{(N_f - b)} \cdot \sum_{j=b}^{N_f} (\Re(F_j) - \langle \Re(F) \rangle)^2 \quad (2.31)$$

is calculated in the range from 2 – 10 MHz (background) for the corrected measurement

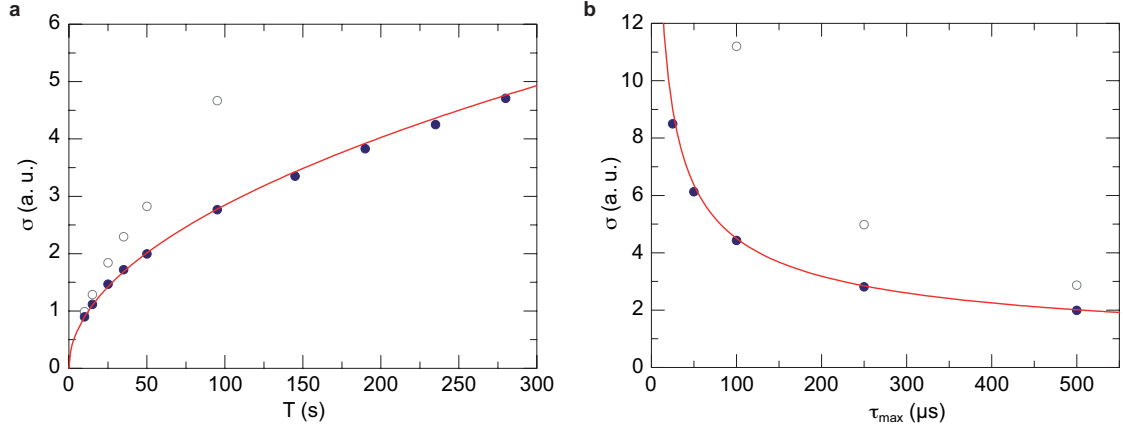


Figure 2.6 – Comparison of spectral noise in the measured data (blue points) with the theoretical expectation (red line) according to eqn. (2.32). The standard deviation σ was calculated for the real part of the Fourier transform of the corrected measurement data between 2 and 10 MHz for (a) different total measurement times T (at $\tau_{\max} = 500 \mu\text{s}$) and (b) different maximum correlation times τ_{\max} (at $T = 50 \text{ s}$). Grey circles denote the calculated standard deviation for the uncorrected measurement data.

data. Here, $j = b$ marks the bin at 2 MHz, $j = N_f$ the corresponding one at 10 MHz and $\langle \Re(F) \rangle$ is the average value of all real Fourier components between 2 and 10 MHz. The variance was determined for different measurement times T and maximum correlation times τ_{\max} . In general, it should hold

$$\Delta [\Re(F_j)] = n_{\text{tot}} \Delta t \sqrt{\frac{T}{2\tau_{\max}}} = \sigma. \quad (2.32)$$

Figure 2.6 shows the results for different T at fixed $\tau_{\max} = 500 \mu\text{s}$ (a) and for different τ_{\max} at fixed $T = 50 \text{ s}$ (b). The plot reveals good agreement of σ (blue points) with the theoretical expectation (red curve) calculated for the parameters given in table 2.1. We conclude that the measurements already reach the shot noise limit and the influence of other contributions, e. g. technical noise, can be neglected.

In contrast to the recalibrated data, the uncalibrated original data (figure 2.6, grey circles) shows a higher noise level compared to the expectation given in eqn. (2.25). In principle both results should be equal. Since the variance is calculated over a wide spectral range, any spectrally broad signal influences the value of the variance. The increased variance results from the drop at $g_0^{(2)}$ which translates into a spectrally broad contribution in frequency domain. The following analysis will therefore only take the recalibrated data into account.

As a next step, the dependence of the sideband strength on T and τ_{\max} is investigated. According to eqn. (2.27) it should scale linearly with T and reveal no dependence on τ_{\max} . Here, the area of the sidebands is calculated by summation over all frequency bins in a limited spectral region around the sideband peaks. Since the spectrum contains some

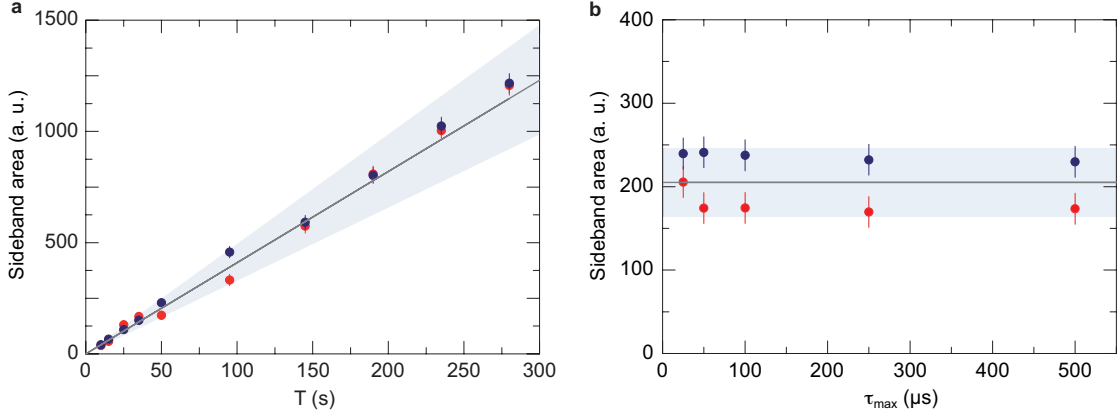


Figure 2.7 – Measured sideband areas of the left (red points) and right (blue points) sideband in comparison to the theoretical expectation (grey line) according to eqn. (2.27) for (a) different measurement times T (at $\tau_{\max} = 500 \mu\text{s}$) and (b) different maximum correlation times τ_{\max} (at $T = 50 \text{ s}$). Since no a priori information is available for n_s , the shaded areas mark the region for $n_s = 400 - 600$ counts/s.

constant offset, the mean value of the background close to each sideband is determined and subsequently subtracted before summing over all bins.

Figures 2.7 (a) and (b) show the calculated area of the left (red) and right (blue) sideband for different measurement times T at $\tau_{\max} = 500 \mu\text{s}$ and for different maximum correlation times τ_{\max} at $T = 50 \text{ s}$, respectively. The theoretical expectation (grey line) is plotted according to eqn. (2.27) with the parameters of table 2.1. The value of n_s can only be estimated in advance and in principle remains as free parameter. Therefore, we included different count rates into the theoretical expectation represented by the shaded area which marks the region for sideband photon count rates between $n_s = 400$ counts/s (lower limit) and $n_s = 600$ counts/s (upper limit). All measured sideband areas for different T and τ_{\max} lie within this region and we conclude that a typical count rate between 400 and 600 counts/s is reasonable.

The linear dependence of the signal strength on T is approved although fluctuations of the sideband areas are present in figure 2.7 (a). They might result from a non-constant coupling strength of the atom to the cavity which changes from one measurement to the other, leading to a fluctuation of n_s as well. Furthermore spectral leakage could also have a slight effect on the sideband area. From figure 2.7 (b) we further conclude that the sideband area does not depend on τ_{\max} as long as $\tau_{\max} > 1/S_W$. The asymmetry of the left and right sideband area is visible for this measurement with $T = 50 \text{ s}$ of data but decreases for higher measurement times as displayed for $\tau_{\max} = 500 \mu\text{s}$ in figure 2.7 (a).

Finally, the theoretically estimated SNR is compared to the experimental results. In eqn. (2.30), the signal was equally spread over several bins, introducing the signal width S_W . In order to achieve an appropriate comparison, we choose the height of the sideband in

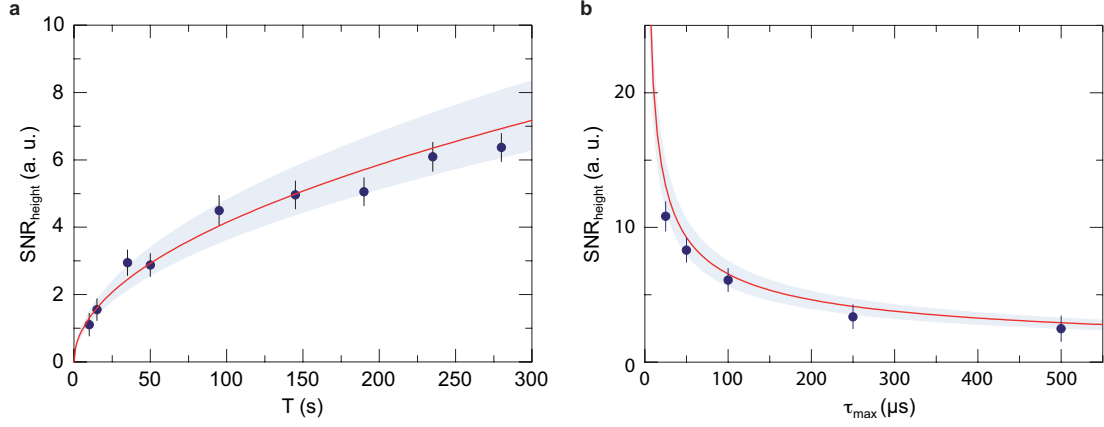


Figure 2.8 – Comparison of the SNR resulting from the measured data (blue points) in comparison to the theoretical expectation (red line) according to eqn. (2.30) for (a) different measurement times T (at $\tau_{\max} = 500 \mu\text{s}$) and (b) maximum correlation times τ_{\max} (at $T = 50 \text{ s}$). Here, only the peak height of the measured signal was considered for the signal strength. The shaded areas define the lower and upper bound for signal widths S_W between 30 and 40 kHz.

the experimental data as signal strength. Equation (2.30) suggests that

$$\text{SNR} \propto \sqrt{\frac{T}{\tau_{\max}}} \quad (2.33)$$

holds in this case. Figure 2.8 presents the corresponding results for T and τ_{\max} (blue points). The parameters of table 2.1 were used again for the theoretical estimation but additionally the signal width S_W remains as free parameter. It was set to a reasonable value of 35 kHz. The expectation with these parameters is plotted as red curve in figure 2.8 together with the shaded area which corresponds to different signal widths S_W ranging from 30 kHz to 40 kHz while the sideband count rate n_s is fixed to 500 counts/s this time. In addition, at $\tau_{\max} = 500 \mu\text{s}$ the signal is very noisy due to the small frequency bin size of 1 kHz. We therefore averaged over 10 bins to achieve reasonable heights in figure 2.8 (a). In figure 2.8 (b), we only averaged over 10 bins for $\tau_{\max} = 500 \mu\text{s}$ and over 5 bins for $\tau_{\max} = 250 \mu\text{s}$. For smaller values of τ_{\max} the peak height could be determined without averaging due to the decreased frequency resolution and thus less noisy spectra.

Both plots agree with our theoretical expectation, nevertheless deviations are noticeable which predominantly result from the sideband signal. First, the coupling of the atom to the cavity might not be constant and thus translate into the sideband strength and height. This effect could lead to the observed spread around the expected result for different measurement times T (figure 2.8 (a)). Second, we observed that the center of the sideband peak varied within a range of $\pm 3 \text{ kHz}$ between different measurement sequences with a duration of $T = 100 \text{ s}$. This might also influence the SNR and lead to a decreased growth of the peak with increasing measurement time, as indicated for $T \geq 200 \text{ s}$ in figure 2.8 (a). In principle this effect could be caused by lock laser intensity

fluctuations (see section 3.3.3). Other effects causing the peak frequency fluctuations have not yet been identified.

Besides those two aspects, an equally spread signal was assumed for the theoretical estimation. It is compared to the height of a Lorentzian-like shaped sideband which can lead to systematic deviations occurring in figure 2.8 (b). Here, the SNR is always smaller than the expected value. Nevertheless, all results lie within a reasonable parameter range.

In the next chapter first measurements of motional sidebands emerging from Raman-scattering in a high-finesse optical cavity are presented.

Chapter 3

Mapping intracavity dynamics to the frequency domain

After a brief theoretical and experimental introduction in chapter 1 and a detailed analysis of the heterodyne detection scheme in chapter 2, this chapter focuses on the application of heterodyne detection as a tool to map the intracavity dynamics to the frequency domain.

We would like to measure the motional sidebands of single cesium atoms trapped inside the optical cavity to investigate intracavity cooling dynamics. In the literature the quantized motion of trapped atoms was already studied using optical heterodyne detection, for example for neutral Rb atoms in free-space [66] or inside an optical cavity for an ensemble of atoms [67]. In our setup, a detailed investigation could reveal more information about intracavity cooling dynamics of single cesium atoms, i. e. their temperature, cooling and heating rate. Their extraction is of major interest since their analysis allows us to quantify the performance of intracavity cooling processes which should be as efficient as possible to achieve ground-state cooling. In the future this detection scheme might become useful to develop new cooling schemes for our setup.

The first part of this chapter introduces the theoretical framework describing the origin of motional sidebands and the expected cooling rate based on a model by M. Bienert and G. Morigi [68]. Subsequently, the discussion of our measurement results follows and a simplified model to describe the observed line shape of the motional sidebands is introduced. The latter allows a first extraction of the approximate cooling rate and temperature of the atoms inside the cavity. Finally, the simple model is compared to the theoretical expectations and possible weaknesses are discussed.

3.1 Theoretical description

Our atoms are trapped in a complex three-dimensional dipole trap potential. To achieve an analytically solvable model, we assume a one dimensional optical harmonic potential

$$U(z) = \frac{1}{2}M\omega_{\text{ax}}^2 z^2 \quad (3.1)$$

with the atomic mass M , the trap frequency ω_{ax} and the displacement from the center of the trap z . An atom trapped in this potential possesses the discrete energies

$$E_m = \hbar\omega_{\text{ax}} \left(m + \frac{1}{2} \right) \quad (3.2)$$

with the corresponding vibrational state $|m\rangle$. The atom's motional state can be changed via light scattering. In a simple picture this can be understood in terms of Stokes and anti-Stokes Raman scattering: An atom in vibrational state $|m\rangle$ can be excited by a photon of frequency ω_p and a subsequent decay via the emission of a frequency shifted photon $\omega_{p'} = \omega_p \pm \omega_{\text{ax}}$ can change its state to $|m \pm 1\rangle$. These processes can be related to cooling and heating processes since a higher vibrational quantum number m corresponds to a higher energy and thus higher temperature. Therefore, transitions from $|m\rangle$ to $|m + 1\rangle$ ($|m - 1\rangle$) lead to heating (cooling) of the atom. A single cesium atom in an optical trap can be combined with an optical cavity to enhance or suppress the respective scattering rates. A theoretical model published by M. Bienert and G. Morigi [68], which describes the interaction of a trapped two-level system with a single mode of an optical cavity externally driven by a weak probe laser, resembles our experimental situation. The main results are discussed in the following section.

3.1.1 Theoretical derivation of sideband scattering rates

The atom-cavity system under consideration is shown in figure 3.1. Inside the cavity a two-level atom of mass M is trapped in a one dimensional harmonic potential along the cavity axis with trap frequency ω_{ax} . The atom's ground (excited) state is denoted by $|g\rangle$ ($|e\rangle$). A weak probe laser drives the cavity whereas the mode of the latter can interact with the atom [68]. Due to imperfect mirrors, photons can leak out of the cavity at the decay rate 2κ . In addition, photons can also be lost due to spontaneous emission Γ into the modes of the electromagnetic field. The total Hamiltonian of the system in a frame rotating with the laser frequency is given by [68]

$$H_{\text{tot}} = H_{\text{ext}} + H_{\text{int}} + H_{\text{cav}} + W + H_{\text{emf}} \quad (3.3)$$

where the center-of-mass motion of the atom in the harmonic trap is described by H_{ext} , the electronic degree of freedom by H_{int} and the cavity degree of freedom by H_{cav} . The

3.1. THEORETICAL DESCRIPTION

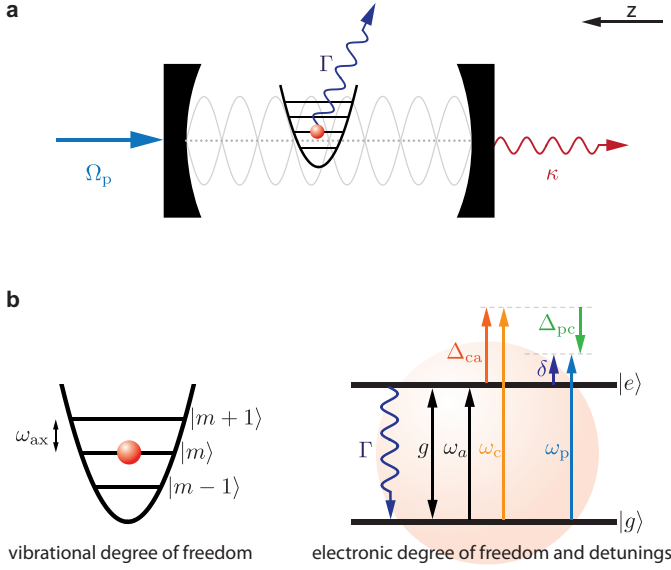


Figure 3.1 – (a) Schematic of the assumed experimental situation: An atom (red) is trapped in a harmonic trap which is displaced by a defined phase angle φ from the intra-cavity field (grey). The cavity is pumped by a probe laser ω_p at rate Ω_p along the cavity axis. The atom can be excited and a subsequent decay leads to the emission of a photon due to spontaneous decay (Γ) or due to cavity losses (κ). (b) In the harmonic trap with level spacing ω_{ax} the atom possesses a vibrational quantum number m (left). The electronic degree of freedom and the relevant detunings between probe laser (ω_p), atom (ω_a) and cavity (ω_c) are depicted in the right schematic. In addition, the coupling introduced by the cavity between both states is denoted by g .

exact expressions are given by

$$H_{\text{ext}} = \hbar\omega_{ax} \left(b^\dagger b + \frac{1}{2} \right) \quad (3.4)$$

$$H_{\text{int}} = -\hbar (\Delta_{ca}|e\rangle\langle e| + \Delta_{pc}|g\rangle\langle g|) \quad (3.5)$$

$$H_{\text{cav}} = -\hbar\Delta_{pc}a^\dagger a \quad (3.6)$$

with the creation (annihilation) operator $b^\dagger(b)$ of a vibrational quantum and the creation (annihilation) operator $a^\dagger(a)$ of a cavity photon. In addition, the detuning between cavity resonance and atomic resonance is given by $\Delta_{ca} = \omega_c - \omega_a$ and the respective probe-cavity detuning by $\Delta_{pc} = \omega_p - \omega_c$. The interactions are described by [68]

$$W = W_p + W_c(z) \\ = \hbar\Omega_p(a + a^\dagger) + \hbar g(z) (|e\rangle\langle g|a + |g\rangle\langle e|a^\dagger). \quad (3.7)$$

The first term describes the rate $\Omega_p = \sqrt{P\kappa}/(\hbar\omega_p)$ at which the cavity is driven by the external probe laser with the power of the probe laser P . The second term, the Jaynes-Cummings term, takes the atom-cavity interaction into account. Here, the position dependent coupling strength $g(z)$ is of major importance for our experiment. It is given by

$$g(z) = g_0 \cos[kz + \varphi] = g_0 \cos\left[\frac{2\pi}{\lambda_p}z + \varphi\right], \quad (3.8)$$

where φ denotes the relative position between the trap center and the intracavity spatial mode function. For an atom at $z = 0$ the coupling can thus be maximized if the trap center and mode function are at the same position in space. The last operator in eqn. (3.3) denotes the electromagnetic field modes external to the cavity and their coupling to the atom-cavity system:

$$\begin{aligned}
 H_{\text{emf}} &= H_{0, \text{emf}} + W_{\kappa} + W_{\Gamma}(z) \\
 &= \hbar \sum_{\vec{k}, \varepsilon} (\omega_{\vec{k}} - \omega_{\text{p}}) c_{\vec{k}, \varepsilon}^{\dagger} c_{\vec{k}, \varepsilon} + \hbar \sum_{\vec{k}, \varepsilon}^{(\kappa)} \left(g_{\vec{k}, \varepsilon}^{(\kappa)} a^{\dagger} c_{\vec{k}, \varepsilon} + h.c. \right) \\
 &\quad + \hbar \sum_{\vec{k}, \varepsilon}^{(\Gamma)} \left(g_{\vec{k}, \varepsilon}^{(\Gamma)} |e\rangle \langle g| \exp [i(\vec{k} \cdot \vec{e}_z)z] c_{\vec{k}, \varepsilon} + h.c. \right).
 \end{aligned} \tag{3.9}$$

Here, $\omega_{\vec{k}}$ describes the frequency of the external mode with the respective creation (annihilation) operator $c_{\vec{k}, \varepsilon}^{\dagger}$ ($c_{\vec{k}, \varepsilon}$) which creates (destroys) a photon of wave vector \vec{k} and polarization index $\varepsilon = (1, 2)$ in the external modes. The first term describes the free dynamics of the external modes whereas the second (third) term denotes the coupling between the cavity (the atom) and the external modes. The exact expressions for $g_{\vec{k}, \varepsilon}^{(\Gamma)}$ and $g_{\vec{k}, \varepsilon}^{(\kappa)}$ can be found in [69, 70]. Both interactions cause photon losses due to spontaneous emission of the atom at a rate Γ or due to cavity losses at rate 2κ , respectively.

The strength of the motional sidebands of trapped cesium atoms depends on the coefficients A_{\pm} where A_{-} (A_{+}) is proportional to the transition rate from $|m\rangle$ to $|m-1\rangle$ ($|m+1\rangle$). Under the assumption that the internal state dynamics and the center-of-mass motion are weakly coupled, the absorption and emission of photons couples only neighboring vibrational energy levels [68]. This allows a description of the vibrational population change by a rate equation

$$\frac{dp_m}{dt} = (m+1)A_{-}p_{m+1} - [(m+1)A_{+} + mA_{-}]p_m + mA_{+}p_{m-1}, \tag{3.10}$$

with the population p_m of the vibrational state $|m\rangle$. The explicit expressions for the photon scattering rates resulting from the change of the motional state were calculated in [68] under two major assumptions: Weak mechanical coupling was assumed which is equivalent to a small Lamb-Dicke parameter $\eta \ll 1$. The latter is defined as

$$\eta = \varepsilon k \tag{3.11}$$

which relates the extension of the atomic ground state wave packet $\varepsilon = \sqrt{\hbar/(2M\omega_{\text{ax}})}$ to the exciting laser wavelength $\lambda_{\text{p}} = 2\pi/k$. An intuitive picture is given in [71]: It states that the Lamb-Dicke parameter is proportional to $\sqrt{E_{\text{rec}}/(\hbar\omega_{\text{ax}})}$ with the recoil energy E_{rec} due to spontaneous emission of a photon. Thus, in the Lamb-Dicke regime, the recoil energy transferred to the atom is much smaller than the vibrational level spacing.

Since the position operator is given by $z = \varepsilon(b + b^\dagger)$, η is proportional to $k \cdot z$ which allows the approximation of the position dependent interactions ($W_c(z)$ and $W_\Gamma(z)$) up to first order in η by the corresponding Taylor series.

The second condition to be fulfilled is a low intracavity photon number which corresponds to weak driving of the cavity by the probe laser and thus allows a perturbative treatment of the interaction dynamics with the latter. The state space then reduces to the states

$$|g, 0\rangle, |g, 1\rangle \text{ and } |e, 0\rangle. \quad (3.12)$$

The application of scattering theory allows the calculation of the scattering rates A_\pm , a detailed calculation can be found in [34] and [68]. Here, we are interested in the final result which is given by

$$A_\pm = \eta^2 A_0 \left[\mathcal{D} + \tan^2[\varphi] \left\{ \mathcal{A}_\pm^{(\Gamma)} + \mathcal{A}_\pm^{(\kappa)} \right\} \right] \quad (3.13)$$

with

$$A_0 = \Gamma \Omega_p^2 \frac{g_0^2 \cos^2[\varphi]}{f(\Delta_{pc})}. \quad (3.14)$$

The dependence on the laser frequency is summarized in $f(\Delta_{pc})$ yielding

$$f(\Delta_{pc}) = \left[\Delta_{pc}(\Delta_{ca} + \Delta_{pc}) - \frac{\kappa\Gamma}{2}(1 + 2C) \right]^2 + \left[\Delta_{pc} \frac{\Gamma}{2} + (\Delta_{ca} + \Delta_{pc})\kappa \right]^2 \quad (3.15)$$

with the single atom cooperativity defined as

$$C = \frac{g_0^2 \cos^2[\varphi]}{\kappa\Gamma}. \quad (3.16)$$

In eqn. (3.13) \mathcal{D} is the diffusion constant and describes the diffusive motion of the atom in lowest non-vanishing order of η caused by the recoil of a spontaneously emitted photon [68]. Nevertheless, mechanical effects on the atom-cavity system are mainly governed by the terms

$$\begin{aligned} \mathcal{A}_\pm^{(\kappa)} &= \frac{8\kappa^2 C}{f(\Delta_{pc} \mp \omega_{ax})} \left[(\delta \mp \omega_{ax}/2)^2 + \frac{\Gamma^2}{4} \right] \text{ and} \\ \mathcal{A}_\pm^{(\Gamma)} &= \frac{1}{f(\Delta_{pc} \mp \omega_{ax})} \left[\left[(\Delta_{pc} \mp \omega_{ax})\delta - \frac{\kappa\Gamma}{2}(1 - 2C) \right]^2 + \left[(\Delta_{pc} \mp \omega_{ax})\frac{\Gamma}{2} + \delta\kappa \right]^2 \right] \end{aligned}$$

with the probe laser atom detuning $\delta = \Delta_{pc} + \Delta_{ca}$. Here, the excitation of the state $|g, 0\rangle \otimes |m\rangle$ due to the absorption of a photon and a cavity-induced change of the motional state from $|m\rangle$ to $|m \pm 1\rangle$ followed by a decay due to cavity losses κ is connected to

$\mathcal{A}_{\pm}^{(\kappa)}$. Similarly, the process with final spontaneous decay into free space instead of cavity losses is connected with $\mathcal{A}_{\pm}^{(\Gamma)}$. The heterodyne detection setup is only sensitive on scattering processes induced by $\mathcal{A}_{\pm}^{(\kappa)}$. As apparent from eqn. (3.13), A_{\pm} exhibits a complex dependence on φ which sensitively depends on the experimental parameters. For our experimental situation, two regions around $\varphi = \pi/2$ show large scattering rates A_{\pm} whereas only small values are expected at $\varphi = 0$. In addition, both scattering rates depend on $1/f(\Delta_{\text{pc}} \mp \omega_{\text{ax}})$ and can hence be maximized if $f(\Delta_{\text{pc}} \mp \omega_{\text{ax}})$ becomes minimal which is achieved if the probe laser detuning is chosen close to the motional sideband frequency ω_{ax} [68]. An important parameter which enables us to distinguish between cooling and heating is the cooling rate [34, 72]

$$\Gamma_{\text{cool}} = A_- - A_+. \quad (3.17)$$

Cooling can thus be enhanced if A_- dominates A_+ . In order to achieve long lifetimes the mean vibrational quantum number [73]

$$\langle m \rangle = \frac{A_+}{A_- - A_+} \quad (3.18)$$

should be minimized. Additionally, the steady state vibrational population distribution [34, 73]

$$p_m = \left(1 - \frac{A_+}{A_-}\right) \left(\frac{A_+}{A_-}\right)^m \quad (3.19)$$

can be calculated analytically from the scattering rates.

3.1.2 Estimation of cooling rates for the experimental parameters

Equations (3.13) and (3.17) can be used to plot the cooling rate for our experimental setup. The parameters we use are summarized in table 3.1. Figure 3.2 (a) shows Γ_{cool} (blue) as a function of the phase φ , with the respective detunings

$$\begin{aligned} \Delta_{\text{pc}} &= 2\pi \cdot 0 \text{ MHz} \quad \text{and} \\ \delta = \Delta_{\text{ca}} &= 2\pi \cdot 20 \text{ MHz}. \end{aligned} \quad (3.20)$$

The highest cooling rate is achieved at $\varphi = 0.41\pi$ while no cooling is present at $\varphi = 0$ which corresponds to the situation where the atom is maximally coupled to the cavity mode. In contrast, the cooling rate becomes slightly negative and thus heating occurs around the anti-node at $\varphi = \pi/2$ where the coupling between the cavity mode and the atom is minimal. Since the cooling rate is maximal close to $\varphi = \pi/2$ this is the most interesting regime for further investigations. The cooling map around this region is shown in figure 3.2 (b) as a function of the probe-atom detuning δ and the probe-cavity

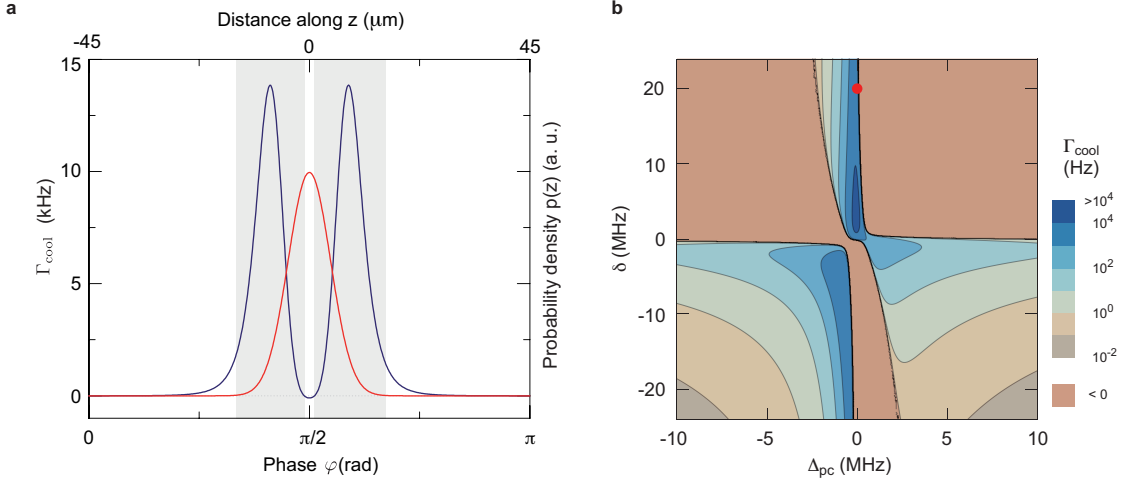


Figure 3.2 – (a) Cooling rate Γ_{cool} (blue) as a function of the phase φ with $\omega_{\text{ax}} = 2\pi \cdot 234$ kHz at the respective detunings $\Delta_{\text{pc}} = 2\pi \cdot 0$ MHz and $\delta = \Delta_{\text{ca}} = 2\pi \cdot 20$ MHz. The atomic probability density $p(z)$ along z before loading the atom into the cavity is shown in red. The grey shaded areas denote the regions which were taken into account for the averaged cooling map presented in (b). (b) Cooling map for our experimental parameters as a function of the probe-atom detuning δ and the probe-cavity detuning Δ_{pc} (for details: see text). Strong cooling regions are shown in blue while orange denotes heating regions ($\Gamma_{\text{cool}} < 0$). The red point marks the detunings chosen for the measurements.

detuning Δ_{pc} . The red point denotes the detunings chosen for subsequent measurements ($\Delta_{\text{pc}} = 0, \delta = 2\pi \cdot 20$ MHz) where a high cooling rate is assured. Since the position for atoms loaded into the cavity cannot be controlled perfectly in our experiment, the cooling map shows an averaged result. Here, averaging was performed for all φ within the grey shaded area in figure 3.2 (a). As a first approximation the respective cooling rates were weighted by the spatial probability distribution $p(z)$ of the atoms along the z -direction before being loaded into the cavity. The probability density is determined by the Gaussian shaped DT potential and yields

$$p(z) = \frac{1}{N} \exp \left[-\frac{2z^2}{k_B T} \frac{U_{0,\text{DT}}}{w_{\text{DT,cav}}^2} \right] \quad (3.21)$$

with the temperature T along z , the DT potential depth $U_{0,\text{DT}} = k_B \cdot 1$ mK, the DT beam radius at the cavity position $w_{\text{DT,cav}} = 39$ μm and a normalization factor N . The relation between the phase φ and the actual position z inside the cavity is given by

$$z(\varphi) = \frac{\lambda_p \cdot \lambda_l}{4|\lambda_p - \lambda_l|} \cdot \left(\frac{\varphi}{\pi} - 0.5 \right). \quad (3.22)$$

The first factor arises from the detuning between the probe and the lock laser which usually amounts to one to three cavity free spectral ranges. Thus, the respective phase φ between the trapping potential and the intracavity field changes from one lattice site to the other (for details, see [31]). Here, λ_p/l denotes the probe and lock laser

wavelength, respectively. The additional shift of 0.5 occurs because the atoms are loaded into the cavity at $\varphi = \pi/2$. The probability density $p(z)$ for a reasonable temperature of $T = 50 \mu\text{K}$ is shown as red curve in figure 3.2 (a). Since heating occurs around $\varphi = \pi/2$ atoms might be rapidly heated out of the lock laser potential and hop to some neighboring lattice sites where cooling occurs. Thus, the heating region was not taken into account for the averaging process. The exact extraction of the phase distribution is rather complex and could possibly be achieved using a sophisticated Bayesian analysis of all measured probe laser transmission traces.

Table 3.1 – Experimental parameters used for the theoretical calculations.

PARAMETER	VALUE
Γ	$2\pi \cdot 5.2 \text{ MHz}$
κ	$2\pi \cdot 0.4 \text{ MHz}$
g	$2\pi \cdot 9 \text{ MHz}$
ω_{ax}	$2\pi \cdot 0.234 \text{ MHz}$
Ω_{p}	$2\pi \cdot 0.17 \text{ MHz}$
η	0.1
\mathcal{D}	1

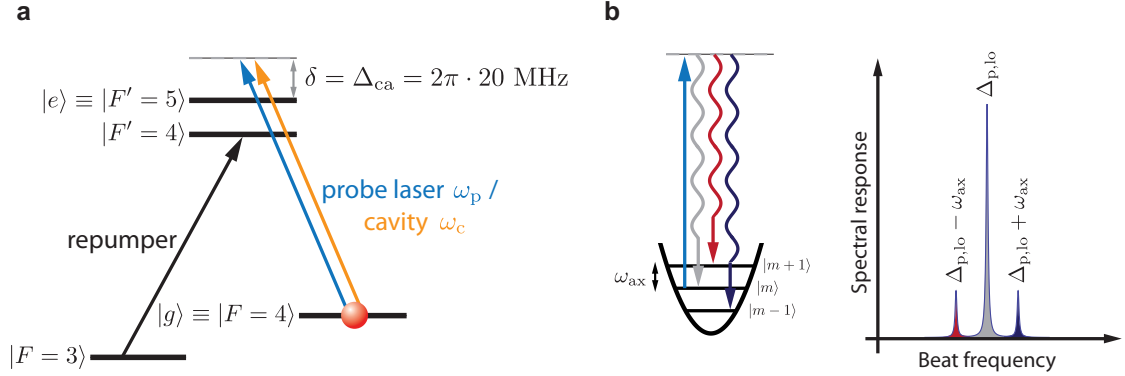


Figure 3.3 – (a) Level scheme with different transitions: Probe laser and cavity are 20 MHz detuned from $|F = 4\rangle \rightarrow |F' = 5\rangle$, the repumper is resonant with the $|F = 3\rangle \rightarrow |F' = 4\rangle$ transition. (b) Schematic representation of sideband transitions and idealized spectral response expected for the heterodyne measurements. The latter includes the Stokes (red) and anti-Stokes (blue) sideband.

3.2 Measuring the quantized motion of single atoms

Experiments are performed with cesium atoms coupled to the cavity mode for an interaction time of 5 s (setup see figure 1.8). They are prepared in the hyperfine state $|F = 4\rangle$ which represents the ground state $|g\rangle$. The excited state $|e\rangle$ is represented by $|F' = 5\rangle$. Furthermore the probe laser with frequency ω_p is in resonance with the cavity ($\Delta_{pc} = 0$) and both have an effective detuning of $\delta = \Delta_{ca} = 2\pi \cdot 20$ MHz from the $|F = 4\rangle \rightarrow |F' = 5\rangle$ transition where the light shifts due to the dipole trap and lock laser are already included. In addition, a repumper is resonant with the $|F = 3\rangle \rightarrow |F' = 4\rangle$ transition, otherwise the state $|F = 3\rangle$ represents a dark state (see figure 3.3 (a)). The detuning between probe laser and local oscillator is set to $\Delta_{p,lo} = 2\pi \cdot 1$ MHz and the respective count rates on the SPCM are chosen according to table 2.1 in chapter 2. All subsequent measurements are performed without the SFDT since it was not implemented into the setup at that time.

In our setup, trapping is achieved along all spatial directions. Nevertheless the confinement along the x direction is rather weak (see figures 1.1 and 3.5). Cesium atoms trapped along the cavity axis due to the lock laser potential have a finite temperature and are thermally distributed over the vibrational states $|m\rangle$. As discussed in the previous subsection the absorption of a probe laser photon leads to an excitation and a subsequent decay into state $|F = 4\rangle$ again which can change the vibrational state. While heating occurs along all spatial dimensions, cooling transitions can only be induced along the cavity axis due to the geometry of the setup. Thus, an intentional reduction of the temperature is only possible along this axis¹. Motional sidebands become measurable due to the frequency shifted decay photons leaking out of the cavity. As apparent from figure 3.2 (a), the atoms should be trapped at a phase difference of $\varphi \approx 0.41\pi$ between

¹Cooling must also occur along the other spatial dimensions, otherwise the atomic lifetimes observed could not be explained. But the underlying mechanisms are not understood so far.

the intracavity electric field and the intracavity dipole trap to achieve maximal cooling rates which also results in large scattering rates into the cavity mode.

The experimental setup only allows us to place the atoms in lattice sites around 0 or $\pi/2$ but exact positioning is not possible. Thus only a fraction of atoms really resides at 0 or $\pi/2$. The latter configuration is achieved by red-detuning the lock laser frequency one cavity free spectral range with respect to the probe laser frequency (about 0.95 THz, $\lambda_l = 854.6$ nm). Due to limited control of the exact position along z and in addition heating at $\varphi = \pi/2$ atoms can nevertheless hop to neighboring lattice sites and thus reside at different φ which results in a distribution of scattering rates.

The observation of first order sidebands for maximal coupling ($\varphi = 0$) is almost impossible, since the scattering rates predicted by theory should vanish. Nevertheless, first measurements at the anti-node revealed weak sidebands which suggest rather large hopping distances of the atoms to neighboring lattice sites along z in this configuration. Since larger scattering rates are expected around $\varphi = \pi/2$ all subsequent measurements of motional sidebands were performed at or close to the node of the intracavity field.

Extraction of the trap frequency along the cavity axis In order to extract frequency information from the photon clicks measured with the SPCM, the data analysis procedure as introduced in chapter 1.3 was performed. Since each measurement trace consists only of 5 s of data, enough statistics is gained by adding up all autocorrelation functions before performing the Fourier transform. The real part of the Fourier transform for one-atom data is displayed in figure 3.4. Here, blue (red) data points denote measurements at low (high) lock laser intensities for a total measurement time $T = 280$ s ($T = 105$ s). According to eqn. (2.27) both spectra were normalized by $n_{l_0} \cdot \Delta t \cdot T$. Therefore, the y -axis denotes the photon scattering rate n_s per frequency bin and per second for both sidebands.

The expected frequency contributions were already discussed in chapter 2 and can be best identified in the coherent intensity distribution given in eqn. (2.2):

$$\begin{aligned} I(t) = & I_{l_0} + I_p + 2I_s + 2\sqrt{I_{l_0}I_p} \cos[\Delta_{p,l_0}t] \\ & + 2\sqrt{I_{l_0}I_s} (\cos[(\Delta_{p,l_0} + \omega_{ax})t] + \cos[(\Delta_{p,l_0} - \omega_{ax})t]) \\ & + 4\sqrt{I_pI_s} \cos[\omega_{ax}t] + 2I_s \cos[2\omega_{ax}t]. \end{aligned}$$

As expected, aside from the strong carrier peak at $\Delta_{p,l_0} = 2\pi \cdot 1$ MHz, sidebands are clearly pronounced at $\Delta_{p,l_0} \pm \omega_{ax}$. The contributions at frequency ω_{ax} are hardly visible in the spectrum while those at $2\omega_{ax}$ are completely buried in noise (both not shown). In addition, two spurious sidebands emerge close to the carrier at 1.00 ± 0.05 MHz. Their origin could not be identified yet but they do not result from interactions with the atom since they also occur if no atom resides in the cavity.

A first check on the sidebands is performed exploiting the relation between the trap frequency ω_{ax} and the lock laser intensity I_{lock} since the latter generates the trapping

potential along z . In general it holds

$$\omega_{\text{ax}} \propto \sqrt{I_{\text{lock}}}. \quad (3.23)$$

The lock laser intensity of both measurements shown in figure 3.4 differs by a factor of two. Therefore, the trap frequency should change by a factor of $\sqrt{2}$. In order to verify the dependence, for a first estimation a Gaussian function was fitted to each sideband and the position of its maximum was used to determine the trap frequency. The fitted values and the corresponding trap frequencies can be found in table 3.2 and agree with the expected $\sqrt{2}$ -dependence within the error margin.

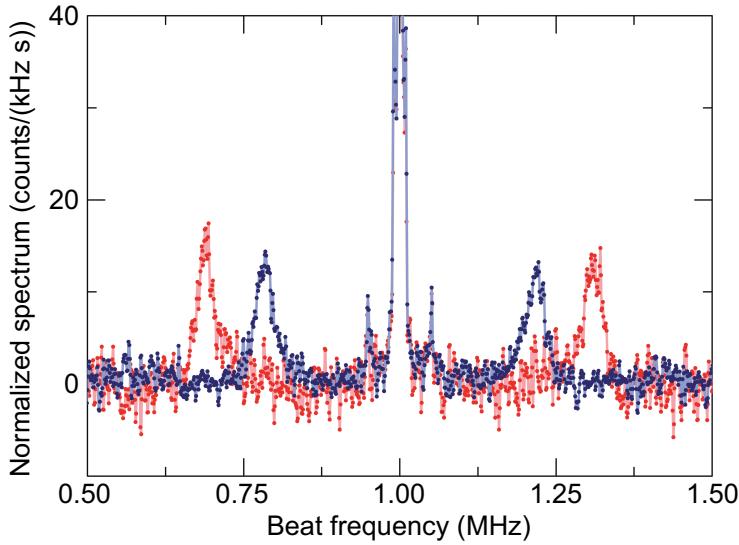


Figure 3.4 – Normalized frequency spectrum for low (blue) and high (red) lock laser intensities. Besides the strong carrier peak at 1 MHz, motional sidebands at the lock laser trap frequency emerge at $\pm\omega_{\text{ax}}/2\pi = \pm 216/310$ kHz for low/high lock laser intensities. Additional peaks arise at ± 50 kHz around the carrier which result from technical artifacts.

Table 3.2 – Extracted trap frequencies resulting from motional sidebands. Here, $\omega_{L/R}$ denotes the measured frequency of the beat signal for the left/right sideband. The extracted and averaged trap frequencies are given by $\omega_{\text{ax},l/h}$ where l/h denotes the values extracted for low/high lock laser intensities.

I_{LOCK}	$\omega_L/2\pi$ [KHZ]	$\omega_R/2\pi$ [KHZ]	$\omega_{\text{AX}}/2\pi$ [KHZ]
low	784 ± 3	1216 ± 3	216 ± 2
high	689 ± 3	1309 ± 3	310 ± 2
	theor. ratio	ω_h/ω_l	$\sqrt{2} = 1.41$
	exp. ratio	$\omega_{\text{ax},h}/\omega_{\text{ax},l}$	1.43 ± 0.02

A distinct feature is the strong asymmetry of the sidebands with a tail towards the carrier frequency at 1 MHz. This is mainly caused by two different broadening mechanisms superimposing the natural linewidth: The first results from the sinusoidally shaped po-

tentials the atoms are trapped in. In contrast to the idealized assumption of a harmonic trap for the theoretical estimation, the vibrational energy levels are non-equidistant. Thus, transition frequencies between adjacent levels depend on the vibrational quantum number and are decreasing with increasing m . A second mechanism resulting in broadening is the radial degree of freedom of the atoms along x since the measurements shown above were performed without the SFDT. Therefore, the atoms experience different lock laser intensities and thus trap frequencies as a function of x . Further broadening arises from fluctuations of the lock laser intensity. Additionally, depending on the assumption of a harmonic or anharmonic trap the vibrational level transition linewidth $2\gamma_{\text{vib}}$ might depend on m as well. A detailed discussion of all effects follows in section 3.3.

3.3 Analytical description of different broadening mechanisms

The following section develops an analytical description of two possible broadening mechanisms which lead to the observed asymmetric line shape. Furthermore the possibility of a vibrational level dependent transition linewidth $2\gamma_{\text{vib}}$ as well as broadening due to lock laser fluctuations will be discussed. The section begins with an analysis of the radial motion along the x -direction, followed by an investigation of the effect of the anharmonic potential. The effects will be combined and compared to the measured data. This allows an estimation of the transition linewidth $2\gamma_{\text{vib}}$ as well as the temperature of the atom along z .

3.3.1 Influence of radial degree of freedom on sideband structure

In our setup strong confinement of the atom is only possible along the dipole trap axis (y) and the cavity axis (z). Especially if the new strongly focused dipole trap is not in use, only weak confinement along the radial x -direction is achieved with the Gaussian shapes of the dipole trap and lock laser only (see figure 3.5). An oscillating atom along this direction is exposed to different lock laser intensities and thus to different trap frequencies ω_{ax} along the cavity axis as a function of x . Therefore, an influence on the structure of the sidebands is expected and the effect of the radial degree of freedom will be investigated. The potential along the x -axis is given by the lock laser and dipole trap laser

$$V_x = -U_{0,\text{lock}} \exp\left[\frac{-2x^2}{w_{0,\text{lock}}^2}\right] - U_{0,\text{DT}} \exp\left[\frac{-2x^2}{w_{0,\text{DT}}^2}\right] - U_{0,\text{SFDT}} \exp\left[\frac{-2x^2}{w_{0,\text{SFDT}}^2}\right] \quad (3.24)$$

with the potential $U_{0,i}$ which denotes the respective trapping potential created by lock laser, dipole trap and strongly focused dipole trap. The corresponding beam radii at the position of the cavity are given by $w_{0,\text{lock}/\text{DT}/\text{SFDT}}$ and the radial displacement of the atom from the center of the beam by x . For small amplitudes the Gaussian potentials

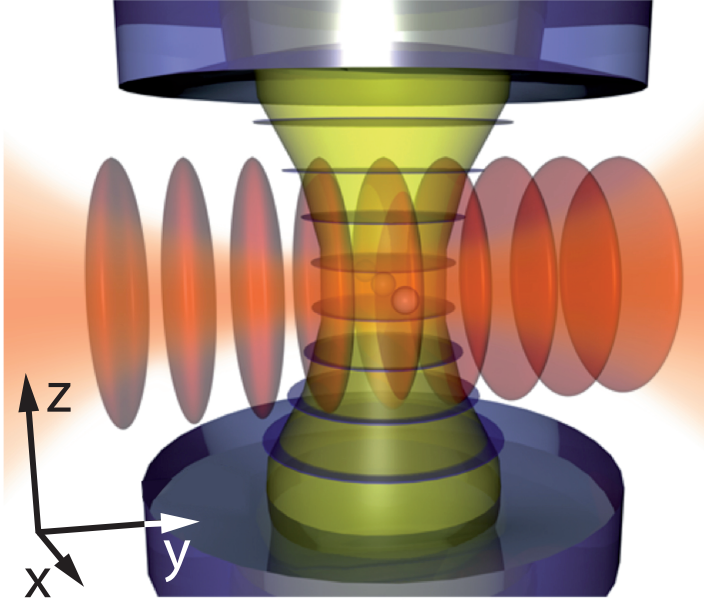


Figure 3.5 – Configuration of different trapping lasers inside the cavity: The standing wave DT (red disks) strongly confines the atoms along the y -direction whereas trapping along the z -direction is achieved with the standing-wave resulting from the lock laser (blue disks). Additional confinement along x can in principle be achieved with a strongly focused Gaussian beam (red) which superimposes the DT along the y -direction. The atoms usually reside inside the cavity and are exposed to the probe laser (yellow). (adapted from [31])

can be approximated by a harmonic potential. Expanding V_x around $x = 0$ yields

$$V_x \approx -(U_{0,\text{lock}} + U_{0,\text{DT}} + U_{0,\text{SFDT}}) + 2x^2\zeta$$

$$\text{with } \zeta = \left(\frac{U_{0,\text{lock}}}{w_{0,\text{lock}}^2} + \frac{U_{0,\text{DT}}}{w_{0,\text{DT}}^2} + \frac{U_{0,\text{SFDT}}}{w_{0,\text{SFDT}}^2} \right). \quad (3.25)$$

Since constant terms in the optical potential only lead to a light shift but do not contribute to the oscillation frequency, they are neglected in the following treatment. The Hamiltonian of the system is given by

$$H = \frac{p^2}{2M} + 2x^2\zeta. \quad (3.26)$$

The oscillation frequency ω_x along the radial direction yields

$$\omega_x = \sqrt{\frac{4}{M}\zeta}. \quad (3.27)$$

We are also interested in the probability distribution $p(x)$ to find the atom at a certain position x along the radial direction. Here, the classical probability $f_{\text{MB}}(x, T_x)$ will be used which is a proper approximation due to the high number of occupied vibrational states along x . For a fixed temperature T_x along the radial direction it is given by the

normalized Boltzmann-factor

$$f_{\text{MB}}(x, T_x) = \frac{1}{N} \exp[-E/(k_B T_x)] \quad (3.28)$$

$$\stackrel{(3.27)}{=} \frac{1}{N} \exp\left[-2x^2\zeta/(k_B T_x)\right]$$

with the normalization

$$N = \int_{-\infty}^{\infty} \exp\left[-2x^2\zeta/(k_B T_x)\right] dx \quad (3.29)$$

and

$$E = \frac{1}{2} M \omega_x^2 x^2. \quad (3.30)$$

Since the atom moves along the x -direction and the lock laser propagating along z has a Gaussian intensity distribution, the axial trap frequency along z will be different at different positions along x . The optical potential of the lock laser is given by

$$U_{\text{lock}} = U_{0,\text{lock}} \cdot \exp\left[\frac{-2x^2}{w_{0,\text{lock}}^2}\right] \cdot \cos^2[kz]. \quad (3.31)$$

Using the harmonic approximation for the potential along the z -direction the trap frequency yields

$$\omega_{\text{ax}}(x) = \sqrt{\frac{4}{M} U_{0,\text{lock}} \exp\left[\frac{-2x^2}{w_{0,\text{lock}}^2}\right]} \quad (3.32)$$

$$= \omega_{\text{ax},0} \cdot \exp\left[\frac{-x^2}{w_{0,\text{lock}}^2}\right]$$

with the vibrational transition frequency $\omega_{\text{ax},0}$ at $x = 0$. The trap frequency thus decreases if the atom is displaced from the center of the lock laser mode at $x = 0$. Therefore, the broadening due to the radial oscillation will extend only to lower frequencies.

The spectral line shape is also determined by the coupling strength g of the atoms to the cavity mode which is proportional to the electric field of the probe laser E_p . Since the electric field distribution of the probe laser beam along the x -axis exhibits a Gaussian shape as well, the coupling strength is reduced for an atom oscillating along this direction according to

$$g(x) = g_0 \exp\left[\frac{-x^2}{w_{0,p}^2}\right] \approx g_0 \exp\left[\frac{-x^2}{w_{0,\text{lock}}^2}\right], \quad (3.33)$$

where g_0 yields the maximal coupling strength at the center of the cavity mode. The last approximation is valid because the mode waist of lock laser and probe laser inside the cavity are approximately equal. Nevertheless, for reasonable temperatures ($T_x < 80 \mu\text{K}$), at least 93 % of the population distribution (eqn. (3.28)) is comprised within $x = \pm 7 \mu\text{m}$ and $g(x = 7 \mu\text{m})$ reduces to $0.91 \cdot g_0$ only. Therefore, the dependence on $g(x)$ will be neglected in the following calculations.

In order to graph the expected radial broadening, the spectral response $R(\omega_{\text{ax}})$ has to be calculated. A transformation from spatial to frequency domain has to be applied first resulting in

$$R(\omega_{\text{ax}}) = f_{\text{MB}}(x, T_x) \cdot 2 \cdot \frac{dx}{d\omega_{\text{ax}}} \quad (3.34)$$

where the factor of two arises because the normalization of the Boltzmann-factor in spatial domain was calculated from $x = -\infty$ to $+\infty$ but frequency domain spans from 0 to $+\infty$ only. An expression for the third factor can be found with eqn. (3.32). Additionally, the dependence on x can be eliminated using eqn. (3.32). The result yields

$$R(\omega_{\text{ax}}) = \frac{1}{\omega_{\text{ax}}} \left(\frac{\omega_{\text{ax},0}}{\omega_{\text{ax}}} \right)^{-2\xi} \sqrt{\frac{2\xi}{\pi \ln \left(\frac{\omega_{\text{ax},0}}{\omega_{\text{ax}}} \right)}} \quad (3.35)$$

where $\xi = \frac{w_{0,\text{lock}}^2}{k_B T_x} \left(\frac{U_{0,\text{lock}}}{w_{0,\text{lock}}^2} + \frac{U_{0,\text{DT}}}{w_{0,\text{DT}}^2} + \frac{U_{0,\text{SFDT}}}{w_{0,\text{SFDT}}^2} \right)$.

The spectral response function is displayed in figure 3.6 (a) for typical experimental parameters $T_x = 50 \mu\text{K}$, $\omega_{\text{ax},0} = 2\pi \cdot 300 \text{ kHz}$ and $U_{0,\text{lock}} = k_B \cdot 0.58 \text{ mK}$. The blue curve shows the spectral broadening if the dipole trap is used only, i. e. $U_{0,\text{DT}} = k_B \cdot 1 \text{ mK}$ and $U_{0,\text{SFDT}} = 0$. Since $R(\omega_{\text{ax}})$ diverges at $\omega_{\text{ax}} = \omega_{\text{ax},0}$ the full width at half maximum is not applicable to quantify broadening. The area under the spectral line is used instead. Here, about 70% of the spectral area is comprised within a region of $\Delta_{\text{rad}} = 2\pi \cdot 4.2 \text{ kHz}$ around $\omega_{\text{ax},0}$.

The improved setup including the strongly focused dipole trap is shown in red ($U_{0,\text{DT}} = k_B \cdot 0.5 \text{ mK}$ and $U_{0,\text{SFDT}} = k_B \cdot 4 \text{ mK}$). As expected, the effect of radial broadening is decreased even further to $\Delta_{\text{rad}} = 2\pi \cdot 0.2 \text{ kHz}$ and hence almost negligible. Nevertheless if the temperature is increased, it becomes more pronounced and will therefore be included into the model.

So far the vibrational transition line itself was assumed to have zero intrinsic width. For a more realistic model, the above result can be convolved with a Lorentzian function introducing a natural line width $2\gamma_{\text{vib}}$

$$L(\omega, \omega_{\text{ax},0}, \gamma_{\text{vib}}) = \frac{1}{\pi} \frac{\gamma_{\text{vib}}}{(\omega - \omega_{\text{ax},0})^2 + \gamma_{\text{vib}}^2}. \quad (3.36)$$

There is no possibility to independently determine the linewidth $2\gamma_{\text{vib}}$ for our measurements. Thus, a reasonable value of $\gamma_{\text{vib}} = 2\pi \cdot 7 \text{ kHz}$ was assumed. The convolved spectral

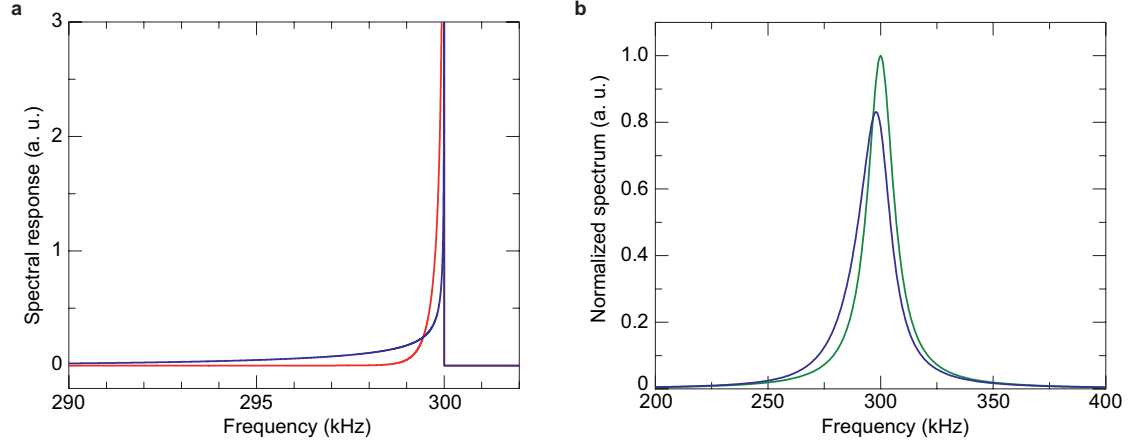


Figure 3.6 – (a) Spectral response function for the influence of radial broadening with (red) and without (blue) the SFDT at $T_x = 50 \mu\text{K}$ and $\omega_{\text{ax},0} = 2\pi \cdot 300 \text{ kHz}$. (b) Influence of radial degree of freedom (without SFDT) convolved with a Lorentzian (blue, linewidth $2\gamma_{\text{vib}} = 2\pi \cdot 14 \text{ kHz}$) in comparison to a regular Lorentzian function at $T_x = 50 \mu\text{K}$ and $\omega_{\text{ax},0} = 2\pi \cdot 300 \text{ kHz}$ (green). The effective broadening is already small without the SFDT.

line (without SFDT, blue) in figure 3.6 (b) reveals a slight asymmetry compared to the Lorentzian (green) for the frequency $\omega_{\text{ax},0} = 2\pi \cdot 300 \text{ kHz}$ which was also expected. In addition, the peak frequency is slightly shifted to lower values. We conclude that the effect of the radial oscillation on the asymmetry of the sidebands is rather small.

3.3.2 Sideband transitions in sinusoidal potentials

The theoretical treatment presented in section 3.1.1 assumed a harmonic trapping potential. In the experimental setup the real trap exhibits a sinusoidal shape. In contrast to a harmonic potential, the energy levels are thus non-equidistant. The following paragraph presents the exact trap frequencies of the sinusoidally shaped potential along z using Mathieu's differential equation to solve the Schrödinger equation.

The Hamiltonian of the system is given by

$$\hat{H} = \frac{\hat{p}^2}{2M} + U_{0,\text{lock}} \cos^2(kz). \quad (3.37)$$

With $\hat{p} = -i\hbar\partial_z$ and the optical potential $U_{0,\text{lock}} \cos^2(kz) = \frac{1}{2}(U_{0,\text{lock}} \cos(2kz) + 1)$ at $x = 0$ the rewritten Hamiltonian yields

$$\hat{H} = -\frac{\hbar^2\partial_z^2}{2M} + \frac{U_{0,\text{lock}}}{2} + \frac{U_{0,\text{lock}}}{2} \cos(2kz). \quad (3.38)$$

The stationary Schrödinger equation is then given by

$$-\frac{\hbar^2\partial_z^2}{2M}\Psi(z) + \left(\frac{U_{0,\text{lock}}}{2} - E_m + \frac{U_{0,\text{lock}}}{2} \cos(2kz)\right)\Psi(z) = 0. \quad (3.39)$$

This equation exhibits the same structure as Mathieu's differential equation [74]:

$$\partial_z^2 f(z) + (a - 2q \cos(2z)) f(z) = 0. \quad (3.40)$$

Equating coefficients in eqns. (3.39) and (3.40) results in

$$a = \frac{M(2E_m - U_{0,\text{lock}})}{(\hbar k)^2} \quad (3.41)$$

$$q = \frac{U_{0,\text{lock}} M}{2(\hbar k)^2}. \quad (3.42)$$

The energies E_m of the different vibrational levels are calculated with the help of *Mathematica* which provides solutions to Mathieu's differential equation. We are now interested in the different transition frequencies between adjacent levels which produce the first order sidebands in the spectra of the heterodyne measurements. They are given by the difference of the energies of two adjacent levels with quantum number m and $m + 1$

$$\Delta E_m = E_{m+1} - E_m = \hbar \omega_{\text{ax},m}. \quad (3.43)$$

Under the assumption of a Boltzmann distribution for the population of the states of the system, the probability for an atom to be in state m is given by

$$p_m(E_m, T_z) = \frac{1}{Z(E_m, T_z)} \exp\left(-\frac{E_m}{k_B T_z}\right) \quad (3.44)$$

with the canonical partition function

$$Z(E_m, T_z) = \sum_{m=0}^{\infty} \exp\left(-\frac{E_m}{k_B T_z}\right). \quad (3.45)$$

Assuming a Lorentzian line shape for each transition the resulting heating (+) and cooling (−) transition line is calculated by summation over all transition lines at the corresponding transition frequency weighted by their respective probability:

$$L_{\pm}(\omega) = C_{\pm} \cdot \sum_{m=0}^{\infty} L(\omega, \mp \omega_{\text{ax},m-b_{\mp}}, \gamma_{\text{vib}}) \cdot (m + b_{\pm}) \cdot p_m(E_m, T_z) \quad (3.46)$$

with the Lorentzian function $L(\omega, \omega_{\text{ax},m}, \gamma_{\text{vib}})$ as defined in eqn. (3.36), a scaling factor C_{\pm} and $b_{+(-)} = 1(0)$. The resulting spectral line is shown in figure 3.8.

3.3.3 Influence of lock laser intensity fluctuations

Aside from broadening due to radial oscillations and the anharmonic potential, lock laser intensity fluctuations can translate into broadening of the motional sideband. The lock

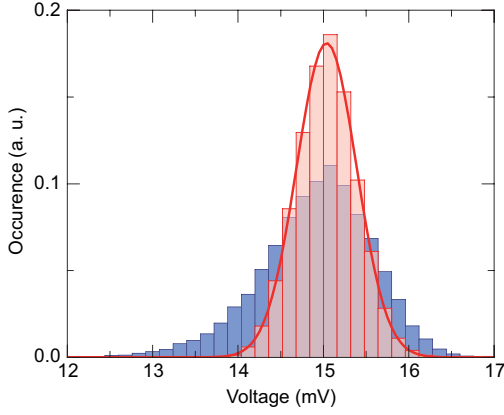


Figure 3.7 – Comparison of the measured lock laser intensity distribution (blue bars) to a thermal light source (red bars). The thermal light source is compared to a Gaussian intensity distribution (red line). The signal was measured with the lock laser APD in units of Volt.

laser transmission was recorded with an APD for each measurement trace at a time resolution of 1 ms which allowed an a posteriori estimation of the intensity fluctuations. For the measurements presented in figure 3.4 the lock laser intensities were binned (bin size 1 ms) and compared to the signal of a thermal light source (flashlight) which was adjusted to the same signal strength and recorded with the same APD. The resulting normalized histograms are shown in figure 3.7. The flashlight signal represents a shot noise limited source and follows the expected Gaussian distribution (red line). It reveals that additional broadening is introduced due to lock laser fluctuations in our measurements. A distinct feature is the asymmetry of the lock laser intensity distribution towards lower intensities which indicate the occurrence of lock laser transmission drops due to fluctuations of the cavity frequency relative to the laser frequency. This might contribute to the observed asymmetric lineshapes. In order to quantify the broadening, a sophisticated approach would include the deconvolution of both distributions to retrieve the original function of the lock laser. The latter would allow the calculation of the exact influence on the sideband structure. As a first error estimate, we assume both distributions to be Gaussian. Then, we exploit the fact that the variance Var of two convolved Gaussian functions is given by the sum of their variances [75]. In order to obtain the real variance of the lock laser intensity $Var(I_{\text{lock, re}})$ without shot noise contributions, the variance of the measured lock laser transmission $Var(I_{\text{lock}})$ and the thermal light source $Var(I_{\text{therm}})$ are subtracted:

$$Var(I_{\text{lock, re}}) = \pm [Var(I_{\text{lock}}) - Var(I_{\text{therm}})] = \pm 0.4 \text{ mV}^2 = \sigma_{I, \text{lock}}^2. \quad (3.47)$$

Relating this value to the mean value of $\bar{I}_{\text{lock}} = 14.9 \text{ mV}$ results in an uncertainty of

$$\frac{\sigma_{I, \text{lock}}}{I} = \pm 0.04. \quad (3.48)$$

According to eqn. (3.23) the trap frequency fluctuations are thus at the order of $\sigma_{\omega_{\text{ax, lock}}} = \pm 0.02 \cdot \omega_{\text{ax}}$. If the spectral line is assumed to follow a normal distribution the influence on the total linewidth can be estimated by quadratic subtraction again.

Finally, the contribution of the lock laser fluctuations to the overall broadening with the trap frequency at the order of $\omega_{ax} = 2\pi \cdot 220$ kHz yields

$$\Delta_{\text{lock}} = \Delta_s - \sqrt{\Delta_s^2 - \left(2\sqrt{2} \ln 2 \sigma_{\omega_{ax}, \text{lock}}\right)^2} = 2\pi \cdot 2 \text{ kHz} \quad (3.49)$$

with the observed sideband full width at half maximum $\Delta_s \approx 2\pi \cdot 35$ kHz. The factor of $2\sqrt{2} \ln 2$ arises since the fullwidth at half maximum relates to σ as $\text{FWHM} = 2\sqrt{2} \ln 2 \sigma$. In conclusion, approximately $2\pi \cdot 2$ kHz of additional broadening is introduced due to the lock laser fluctuations. Since the lock laser intensity was recorded with a time resolution of 1 ms, all fluctuations at frequencies higher than 1 kHz are averaged out and are thus not detectable. Therefore, additional broadening can still be introduced if additional fluctuations occur on shorter timescales. Mechanical fluctuation which might cause lock laser intensity fluctuations are unlikely at frequencies above 1 kHz. Thus, lock laser fluctuations as a source for linewidth broadening are neglected.

3.3.4 Level dependent transition linewidth

The exact dependence between the vibrational transition linewidth $2\gamma_{\text{vib}}$ and the vibrational level m is unknown for our setup. In case that the transition lines are well separated, i. e. for a strongly anharmonic potential, the linewidth $2\gamma_{\text{vib}}$ is given by the inelastic photon scattering rate [76]:

$$\gamma_{\text{vib}} \propto m. \quad (3.50)$$

On the other hand, if the potential is purely harmonic, one can show that the decay rate of coherences between neighboring vibrational levels is independent of the vibrational level m [72, 73]. The linewidth is then determined by the cooling rate Γ_{cool} as given in eqn. (3.17). Since the dipole trap has a sinusoidal shape, a clear distinction between the harmonic and anharmonic case is not possible. The real dependence on the transition linewidth might be a mixture of both models. Hence, for a first estimation the transition linewidth is assumed to be independent of m .

3.3.5 Resulting spectral line shape

The resulting line shape is now calculated including the broadening due to the anharmonic potential and the radial degree of freedom. Possible broadening introduced by lock laser fluctuations is neglected. With the expressions given in eqns. (3.28), (3.36) and (3.44) the spectral line shape caused by heating and cooling transitions can be described

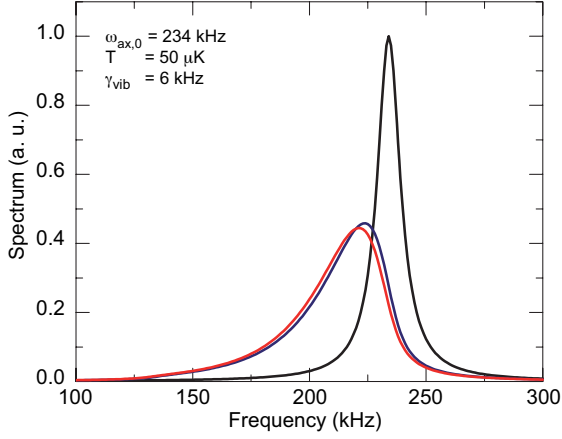


Figure 3.8 – Contribution of different broadening mechanisms: A regular Lorentzian (black, $\omega_{\text{ax},0} = 2\pi \cdot 234 \text{ kHz}$, $2\gamma_{\text{vib}} = 2\pi \cdot 12 \text{ kHz}$) is compared to the simulated lineshape taking the anharmonic potential into account (blue, $\omega_{\text{ax},0} = 2\pi \cdot 234 \text{ kHz}$, $2\gamma_{\text{vib}} = 2\pi \cdot 12 \text{ kHz}$, $T = 50 \mu\text{K}$) and in addition the radial degree of freedom which results from eqn. (3.51) (red, same parameters).

according to

$$\begin{aligned}
 S_{\pm}(\omega) &= S_{\pm}^* \cdot L_{\pm}(\omega) \\
 &= S_{\pm}^* \cdot \sum_{m=0}^{\infty} \int_{-\infty}^{+\infty} f_{\text{MB}}(x, T_x) \cdot (m + b_{\pm}) \\
 &\quad \cdot \frac{1}{\pi} \frac{\gamma_{\text{vib}}}{(\omega \pm \omega_{\text{ax},m-b_{\pm}}(x))^2 + \gamma_{\text{vib}}^2} \cdot p_m(E_m, T_z) dx \\
 &\quad \text{where } S_{\pm}^* = S_{\pm} / \int_{-\infty}^{+\infty} L_{\pm}(\omega) d\omega \quad \text{and } b_{+(-)} = 1(0).
 \end{aligned} \tag{3.51}$$

Here, S_+ (S_-) denotes the total number of Stokes (anti-Stokes) sideband photons detected at the SPCM which can in principle be theoretically calculated if the phase φ between the lock laser trapping potential and the probe laser as well as the correct coupling constant g are known (see next section). In eqn. (3.51) the oscillation along the radial direction is assumed to be adiabatic with respect to the axial frequency and diabatic compared to heating and cooling mechanisms along the cavity, i. e. the motional population distribution will not change while the atom oscillates along the radial direction. Therefore, $p_m(E_m, T_z)$ is not modified and the distribution at $x = 0$ will be used for all calculations which is justified since the spatial distribution peaks at this position. Additionally, $T_x = T_z = T$ is assumed for all further calculations.

To estimate the influence of both broadening mechanisms, the regular Lorentzian function ($\omega_{\text{ax},0} = 2\pi \cdot 234 \text{ kHz}$, $\gamma_{\text{vib}} = 2\pi \cdot 6 \text{ kHz}$) is shown in figure 3.8 (black) in comparison to the spectral line resulting from the anharmonic potential (blue) at a temperature of $T = 50 \mu\text{K}$. The red graph additionally takes the radial degree of freedom into account which corresponds to the solution of eqn. (3.51). As expected the radial degree of freedom leads only to a minor correction and shifts the peak position slightly to lower trap frequencies. The major contribution to the asymmetry arises from the anharmonic trapping potential.

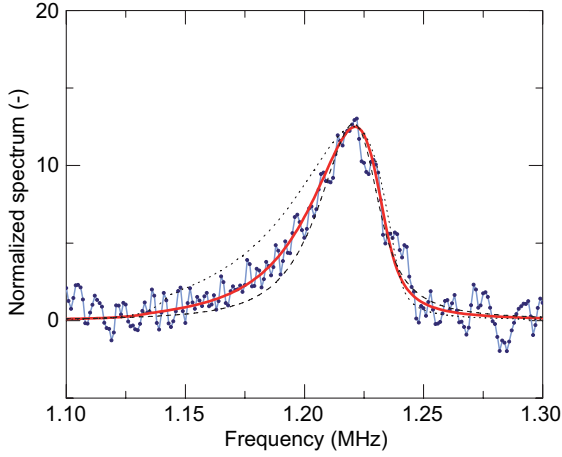


Figure 3.9 – Comparison of the measured vibrational anti-Stokes sideband at low lock laser intensities (blue) and simulated line shapes according to eqn. (3.51) for different sets of parameters: Best agreement with the data is achieved for $T = 50 \mu\text{K}$, $2\gamma_{\text{vib}} = 2\pi \cdot 12 \text{ kHz}$ and $\omega_{\text{ax},0} = 2\pi \cdot 234 \text{ kHz}$ (red). The dashed (dotted) black line denotes the simulated results with $T = 30 \mu\text{K}$, $2\gamma_{\text{vib}} = 2\pi \cdot 18 \text{ kHz}$ and $\omega_{\text{ax},0} = 2\pi \cdot 229 \text{ kHz}$ ($T = 80 \mu\text{K}$, $2\gamma_{\text{vib}} = 2\pi \cdot 6 \text{ kHz}$ and $\omega_{\text{ax},0} = 2\pi \cdot 239 \text{ kHz}$). They mark the lower and upper bounds for the temperature and linewidth estimation.

3.4 Comparison of modeled line shape and measurements

The modeled line shape is now compared to the measured motional sidebands at low lock laser intensities. Since a numerical fit of the resulting function given in eqn. (3.51) is computationally very costly, all free parameters ($S_{\pm}, T, \omega_{\text{ax},0}, \gamma_{\text{vib}}$) were manually optimized. Figure 3.8 shows three calculated line shapes for the indicated parameters together with the experimental one-atom data at low trap frequencies ($\omega_{\text{ax},l} = 2\pi \cdot 216 \text{ kHz}$). At high temperatures (dotted line, $T = 80 \mu\text{K}$) the corresponding vibrational transition linewidth $2\gamma_{\text{vib}} = 2\pi \cdot 6 \text{ kHz}$ has to be chosen sufficiently small to properly fit the steep slope towards higher frequencies. Nevertheless, the left shoulder is overestimated since a higher temperature leads to higher mean vibrational quantum numbers and thus higher vibrational levels will be occupied which in turn lead to lower vibrational transition frequencies contributing to the spectral asymmetry. The sudden kink at 1.14 MHz results from the finite number of occupied vibrational levels taken into account for the simulation. They will only lead to a minor correction of the spectral line shape and are thus neglected. In contrast, at low temperatures (dashed line, $T = 30 \mu\text{K}$) the right slope is described properly if the linewidth $2\gamma_{\text{vib}}$ is increased to $2\pi \cdot 18 \text{ kHz}$. Nevertheless, the data is underestimated at lower trap frequencies which results from the lower temperature and thus a lower mean vibrational quantum number. Best agreement with the dataset is achieved for a temperature of $T = 50 \mu\text{K}$ and a linewidth $2\gamma_{\text{vib}} = 2\pi \cdot 12 \text{ kHz}$ with the lowest vibrational transition frequency given by $\omega_{\text{ax},0} = (E_1 - E_0)/\hbar = 2\pi \cdot 234 \text{ kHz}$. In comparison to the calculated lock laser trap frequency $\omega_{\text{ax},l}$ in section 3.2, where a Gaussian fit function was used, a discrepancy of approximately 10% is apparent which can be explained by the anharmonic trap again. The total photon scattering rates S_{-} deduced from the fit functions lie between 500 cps for $T = 30 \mu\text{K}$ and 700 cps for $T = 80 \mu\text{K}$.

Although figure 3.9 suggests that the simple model describes the data sufficiently well it allows only a rough estimation of the atom's temperature along z inside the cavity. Additional broadening mechanisms like fluctuations of the lock laser intensity and hopping along the y - and z -direction (for details, see [40]) were not taken into account and

might lead to an overestimation of the natural linewidth $2\gamma_{\text{vib}}$ or the temperature T . The aforementioned possible vibrational level dependent linewidth $2\gamma_{\text{vib}}$ could also lead to deviations. Furthermore the atomic wave package has a spatial probability distribution which depends on the vibrational level. This can also lead to a vibrational level dependent probe laser transmission and thus influences the recorded photon scattering rate. To conclude, the parameter range can be limited to

$$\begin{aligned}
 S_- &= 500 - 700 \text{ cps} \\
 \omega_{\text{ax},0} &= 2\pi \cdot (229 - 240 \text{ kHz}) \\
 T &= 30 - 80 \mu\text{K} \\
 2\gamma_{\text{vib}} &= 2\pi \cdot (6 - 18 \text{ kHz}).
 \end{aligned} \tag{3.52}$$

The corresponding values for the Stokes sideband agree with these values. In addition, a numerical fit to the spectrum neglecting the radial degree of freedom lies within the estimated parameter range as well and we conclude that the radial oscillation is almost negligible at temperatures below $100 \mu\text{K}$. In order to achieve smaller uncertainties, a more sophisticated approach would include a full quantum mechanical simulation of the system using a master equation approach.

Comparison to the expected scattering rate The total photon number scattered out of the cavity mode which is expected at the SPCM can also be calculated according to eqns. (3.13), (3.14) and (3.19)

$$S_{\pm}(\varphi) = \frac{1}{2} \sum_{m=0}^{\infty} p_m \cdot (m + b_{\pm}) \cdot \eta^2 A_0 \tan^2[\varphi] A_{\pm}^{(\kappa)} \cdot \eta_{\text{det}}. \tag{3.53}$$

Here, $+$ ($-$) again denotes photon scattering from the Stokes (anti-Stokes) sideband and $b_{+(-)} = 1(0)$. The factor $1/2$ arises since the output of one cavity mirror is detected. The total detection efficiency is comprised in η_{det} which yields 4.4% [23]. As mentioned previously the phase cannot be exactly determined. Therefore, we average over a phase distribution around $\pi/2$ again. Each scattering rate is weighted with the respective spatial probability distribution $p(\varphi)$ as introduced in eqns. (3.21) and (3.22). Hence, the theoretically expected photon scattering rate adds up to

$$\bar{S}_{\pm} = \int_0^{0.49\pi} p(\varphi) \cdot S_{\pm}(\varphi) d\varphi + \int_{0.51\pi}^{\pi} p(\varphi) \cdot S_{\pm}(\varphi) d\varphi. \tag{3.54}$$

Similarly the averaged cooling rate Γ_{cool} is calculated according to eqn. (3.17). In addition, the expected temperature can be deduced from the ratio A_-/A_+ [73]:

$$T = \frac{\hbar\omega_{\text{ax}}}{k_B \cdot \ln(A_-/A_+)}. \tag{3.55}$$

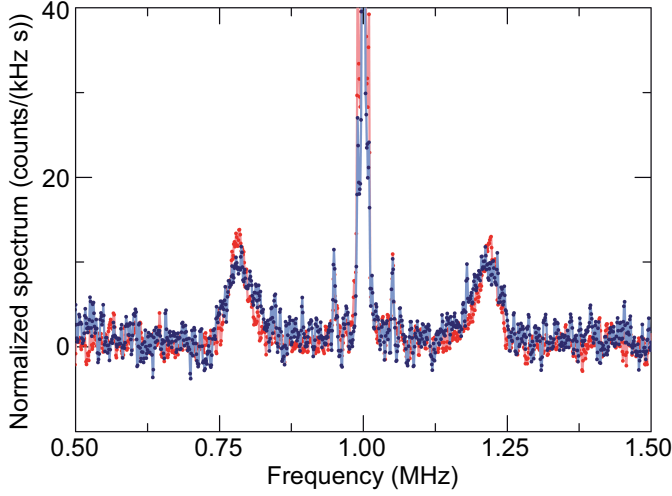


Figure 3.10 – Normalized frequency spectrum for one (red) and two (blue) atoms inside the cavity. The two-atom data exhibits a slightly increased linewidth.

The calculated parameters for $\omega_{ax} = \omega_{ax,0} = 2\pi \cdot 234$ kHz and using the values given in table 3.1 then read

$$\begin{aligned}\bar{S}_- &= 500 \text{ cps} \\ T &= 26 \mu\text{K} \\ \Gamma_{\text{cool}} &= 2\pi \cdot 5 \text{ kHz}.\end{aligned}\tag{3.56}$$

Comparing eqns. (3.52) and (3.56) reveals that the simple model provides proper estimates within an appropriate order of magnitude. The theoretical model also possesses a significant uncertainty since the phase distribution as well as the precise coupling constant g are unknown. As apparent from figure 3.2, the cooling rate rapidly changes over a small range of φ which demands a good a priori knowledge of the phase φ to achieve reliable predictions.

3.5 Future challenges

Since all measurements were performed before the SFDT was set up, a major problem was the weak control of the coupling strength. Atoms could hop along the cavity axis which results in an uncertainty of φ and thus g . The new SFDT might allow better control of the coupling to the cavity which could in turn enable us to prove intracavity ‘ g -control’ via heterodyne detection. A Bayesian analysis in combination with a hidden Markov model [77] would in addition allow the extraction of the φ -distribution from the measured cavity transmission traces and thus lead to more accurate theoretical estimates.

Besides the observation of motional sidebands resulting from one atom inside the cavity, the investigation of possible collective cooling effects for two or more atoms coupled to the cavity will be of interest. First measurements were already performed but further investigations are necessary to develop a deeper understanding (see figure 3.10).

The heterodyne detection setup can also be used to investigate intracavity EIT-cooling [23, 25] as well as the influence of the SFDT on the structure of the sidebands. The simulations suggest that the latter should not significantly affect the sideband width. Further ideas comprise measurements at different detunings, e. g. at $\Delta_{\text{pc}} = \pm\omega_{\text{ax}}$ to enhance or suppress cooling transitions which then results in a strong Stokes/anti-Stokes sideband asymmetry.

Summary and outlook

The most prominent challenge in recent experiments is a sufficient control of the coupling strength g . For most experiments and especially for the realization of entanglement of two atoms inside the cavity this property has to be controlled reasonably well. Better coupling control can be achieved by stronger confinement of the atom on the one hand and sufficient cooling of the atom on the other hand.

The present thesis therefore pursued two main objectives: Enhanced confinement and the investigation of intracavity cooling dynamics of single atoms trapped inside a high-finesse optical cavity. The first could be achieved with the implementation of a strongly focused dipole trap. It should allow for stronger confinement along the x -direction and thus better coupling control of the atoms. The experimental characterization of the SFDT revealed good agreement with theoretical expectations: The collimated beam exhibits minor aberrations introduced by the 2'' collimator. Behind the focusing lens the measured beam profile agrees well with the expected point spread function and exhibits a minimum waist of approximately $(9.8 \pm 1.0) \mu\text{m}$. The measurement of the radial trap frequency revealed an increase from $(1.8 \pm 0.2) \text{kHz}$ with the original DT configuration to $(15.3 \pm 0.3) \text{kHz}$ with the SFDT setup. This indicated enhanced confinement of the atoms inside the cavity and agrees with the theoretical expectations. In the future, transmission histograms of atoms coupled to the cavity might reveal a distribution close to a Poissonian which would then allow a better distinction between one and two atoms coupled to the cavity. This is eligible for proper feedback control of the atomic state(s) inside the cavity [24].

Aside from proper confinement, sufficient cooling inside the cavity is desirable and hence cooling dynamics should be investigated intensively. In order to gain further insight into intracavity cooling dynamics a new detection scheme, namely heterodyne detection, was integrated into the existing experimental setup. Besides the introduction of the theoretical framework of heterodyne detection, the analytical description of the continuous electric field and intensity distribution for motional sideband transitions was developed. Furthermore the analytical expression for the autocorrelation function and the corresponding Fourier spectrum were presented as well and discretized expressions for both were found, representing the experimental situation. Additionally, technical effects which superimpose the signal, namely the detector dead time and the afterpulsing effect, were successfully eliminated. A derivation of the signal-to-noise ratio in heterodyne measure-

ments was presented and compared to our measurement results. In summary we achieved a proper description of the SNR which agreed well with experimental results and the choice of optimal parameters to achieve a high signal-to-noise ratio became possible.

Heterodyne spectroscopy was exploited to detect the motional sidebands of single cesium atoms trapped inside the high-finesse optical cavity. The measured trap frequencies along the cavity axis revealed the expected dependence on the lock laser intensity as well as distinct asymmetries. The latter mainly arose due to an anharmonic trapping potential. In addition, other sources which might cause broadening were discussed, namely radial oscillations, lock laser fluctuations and a vibrational level dependent transition linewidth. We conclude that radial oscillations have only a minor influence on the overall broadening even if the SFDT is not used. The effect of lock laser fluctuations on the sideband structure is negligible whereas the contribution of the vibrational level dependent transition linewidth could not be clearly identified.

A simplified model was developed taking into account the most prominent broadening sources in order to extract the intracavity atomic temperature and the respective cooling rate. A comparison to a theoretical model introduced by M. Bienert and G. Morigi revealed that our model allows a rough estimation of the temperature and cooling rate but a more sophisticated approach is necessary to gain further insight. Here, a full quantum simulation might lead to more accurate results.

One major limiting parameter for the simulations was the uncertainty concerning the phase φ between the cavity mode function and the trapping potential. The SFDT might reduce the atomic hopping along the z direction which should enable better control of φ and thus g . In the near future we might be able to prove that proper coupling control is achieved in our setup.

Since only few measurements have been performed with the new heterodyne setup, a variety of ideas already exists for future measurements. They include the investigation of possible collective cooling effects of two or more atoms coupled to the cavity as well as the investigation of intracavity EIT-cooling. Especially for the investigation of new cooling schemes and their efficiency the heterodyne detection setup opens up new possibilities. Furthermore the influence of the SFDT on the sideband structure can also be investigated. Although simulations suggest that its influence on the structure of the sidebands is rather small, a comparison to experimental data could confirm the expectations and a detailed analysis should be conducted as well.

If strong confinement of the atoms is well controlled in the near future and ground state cooling becomes possible with the application of new cooling schemes, the realization of two-atom entanglement inside the cavity might become feasible.

Bibliography

- [1] T. Pellizzari et al. *Decoherence, Continuous Observation, and Quantum Computing: A Cavity QED Model*. In: Phys. Rev. Lett. **75**, 21 (1995).
- [2] P. W. Shor. *Polynomial-time algorithms for prime factorization and discrete logarithms on a quantum computer*. In: SIAM Review **41**, 2 (1999), pp. 303–332.
- [3] S. A. Aljunid et al. *Phase shift of a weak coherent beam induced by a single atom*. In: Phys. Rev. Lett. **103**, 153601 (2009).
- [4] P. R. Berman. *Cavity Quantum Electrodynamics*. Academic Press, San Diego, 1994.
- [5] S. Haroche and J.-M. Raimond. *Exploring the Quantum*. Oxford University Press, 2006.
- [6] E. T. Jaynes and F. W. Cummings. *Comparison of quantum and semiclassical radiation theories with application to the beam maser*. In: Proceedings of the IEEE **51** (1963), pp. 89–109.
- [7] H. J. Metcalf and P. van der Straten. *Laser Cooling and Trapping*. Springer, 1999.
- [8] C. J. Hood et al. *Real-Time Cavity QED with Single Atoms*. In: Phys. Rev. Lett. **80**, 4157 (1998).
- [9] P. Münstermann et al. *Single slow atoms from an atomic fountain observed in a high-finesse optical cavity*. In: Opt. Comm. **159**, 63 (1999).
- [10] S. Nußmann et al. *Submicron Positioning of Single Atoms in a Microcavity*. In: Phys. Rev. Lett. **95**, 173602 (2005).
- [11] J. A. Sauer et al. *Cavity QED with optically transported atoms*. In: Phys. Rev. A **69**, 051804 (5 2004).
- [12] M. Khudaverdyan et al. *Controlled insertion and retrieval of atoms coupled to a high-finesse optical resonator*. In: New Journal of Physics **10**, 073023 (2008).
- [13] C. J. Hood et al. *The Atom-Cavity Microscope: Single Atoms Bound in Orbit by Single Photons*. In: Science **287**, 1447 (2000).
- [14] J. McKeever et al. *Experimental realization of a one-atom laser in the regime of strong coupling*. In: Nature **425** (2003), pp. 268–271.
- [15] K. M. Birnbaum et al. *Photon blockade in an optical cavity with one trapped atom*. In: Nature **436** (2005), pp. 87–90.

- [16] T. Wilk et al. *Single-Atom Single-Photon Quantum Interface*. In: Science **317**, 5837 (2007).
- [17] H. J. Kimble. *The quantum internet*. In: Nature **453**, 1023 (2008).
- [18] A. D. Boozer et al. *Cooling to the ground state of axial motion for one atom strongly coupled to an optical cavity*. In: Phys. Rev. Lett. **97**, 083602 (2006).
- [19] J. Bochmann et al. *Lossless state detection of single neutral atoms*. In: Phys. Rev. Lett. **104**, 203601 (2010).
- [20] R. Gehr et al. *Cavity-based single atom preparation and high-fidelity hyperfine state readout*. In: Phys. Rev. Lett. **104**, 203602 (2010).
- [21] M. Khudaverdyan et al. *Quantum jumps and spin dynamics of interacting atoms in a strongly coupled atom-cavity system*. In: Phys. Rev. Lett. **103**, 123006 (2009).
- [22] S. Reick et al. *Analyzing quantum jumps of one and two atoms strongly coupled to an optical cavity*. In: J. Opt. Soc. B **27**, A152 (2010).
- [23] T. Kampschulte. “Coherently driven three-level atoms in an optical cavity”. PhD thesis. Institute of Applied Physics, University of Bonn, 2011.
- [24] S. Brakhane. “Kontrolle der Atom-Resonator-Wechselwirkung mit Hilfe einer Regelschleife”. Diploma thesis. Institute of Applied Physics, University of Bonn, 2011.
- [25] T. Kampschulte et al. *Optical Control of the Refractive Index of a Single Atom*. In: Phys. Rev. Lett. **105**, 153603 (2010).
- [26] M. Eckstein. “Three-level physics of a single atom coupled to a high finesse cavity”. Diploma thesis. Institute of Applied Physics, University of Bonn, 2010.
- [27] A. S. Sørensen and K. Mølmer. *Measurement Induced Entanglement and Quantum Computation with Atoms in Optical Cavities*. In: Phys. Rev. Lett. **91**, 9 (2003).
- [28] Alexander Thobe. “Quantum Jumps of One and Two Atoms in a Strongly Coupled Atom-Cavity System”. Diploma thesis. Institute of Applied Physics, University of Bonn, 2009.
- [29] C. Monroe et al. *Resolved-sideband Raman cooling of a bound atom to the 3D zero-point energy*. In: Phys. Rev. Lett. **75**, 4011 (1995).
- [30] S. Svanberg. *Atomic and molecular spectroscopy*. Springer, 2004.
- [31] Sebastian Reick. “Internal and external dynamics of a strongly-coupled atom-cavity system”. PhD thesis. Institute of Applied Physics, University of Bonn, 2009.
- [32] Sergio M. Dutra. *Cavity Quantum Electrodynamics - The Strange Theory Of Light In A Box*. John Wiley and Sons, 2005.
- [33] H. Carmichael. *An Open System Approach to Quantum Optics*. Springer-Verlag, Berlin, 1993.
- [34] M. Bienert and G. Morigi. *Cavity cooling of a trapped atom using electromagnetically induced transparency*. In: N. J. Phys. **14**, 023002 (2012).

- [35] Mkrtych Khudaverdyan. “A controlled one and two atom-cavity system”. PhD thesis. Institute of Applied Physics, University of Bonn, 2009.
- [36] Stefan Kuhr. “A controlled quantum system of individual neutral atoms”. PhD thesis. Institute of Applied Physics, University of Bonn, 2003.
- [37] Wolfgang Alt. “Optical Control of Single Neutral Atoms”. PhD thesis. Institute of Applied Physics, University of Bonn, 2004.
- [38] Dominik Schrader. “A Neutral Atom Quantum Register”. PhD thesis. Institute of Applied Physics, University of Bonn, 2004.
- [39] Yevhen Miroshnychenko. “An atom-sorting machine”. PhD thesis. Institute of Applied Physics, University of Bonn, 2006.
- [40] Igor Dotsenko. “Single atoms on demand for cavity QED experiments”. PhD thesis. Institute of Applied Physics, University of Bonn, 2007.
- [41] Wenjamin Rosenfeld. “A high finesse optical resonator for cavity QED experiments”. Diploma thesis. Institute of Applied Physics, University of Bonn, 2003.
- [42] M. Khudaverdyan. “Addressing of individual atoms in an optical dipole trap”. Diploma thesis. Institute of Applied Physics, University of Bonn, 2003.
- [43] A. Stiebeiner. “Deterministische Kopplung eines einzelnen Atoms an die Mode eines Resonators hoher Finesse”. Diploma thesis. Institute of Applied Physics, University of Bonn, 2007.
- [44] K. Lenhard. “Stabilisierung eines Resonators hoher Finesse zur Atom- Lichtfeld-Kopplung”. Diploma thesis. Institute of Applied Physics, University of Bonn, 2008.
- [45] K. Schörner. “Ein phasenstabilisiertes Lasersystem für resonatorinduzierte Raman-Prozesse”. Diploma thesis. Institute of Applied Physics, University of Bonn, 2008.
- [46] W. Alt. *An objective lens for efficient fluorescence detection of single atoms*. In: *Optik - International Journal for Light and Electron Optics* **113**, 142 (2002).
- [47] I. Dotsenko et al. *Submicrometer Position Control of Single Trapped Neutral Atoms*. In: *Phys. Rev. Lett.* **95**, 3 (2005).
- [48] D. Schrader et al. *An optical conveyor belt for single neutral atoms*. In: *Applied Physics B* **73** (2001), pp. 819–824.
- [49] Anna Hambitzer. “Direct synthesis of light polarization for state-dependent transport of atoms”. MA thesis. Institute of Applied Physics, University of Bonn, 2012.
- [50] Maximilian Genske. “Bloch oscillations in discrete quantum walks”. MA thesis. University of Cologne, 2012.
- [51] R. W. P. Drever et al. *Laser phase and frequency stabilization using an optical resonator*. In: *Applied Physics B* **31**, 2 (1983), pp. 97–105.
- [52] D. Schrader et al. *Neutral atom quantum register*. In: *Phys. Rev. Lett.* **93**, 150501 (2004).
- [53] Daniel Malacara. *Optical Shop Testing*. John Wiley and Sons, 1992.

- [54] C. E. Shannon. *Communications in the presence of noise*. In: Proceedings of the IRE **37** (1949), pp. 10–21.
- [55] H. Nyquist. *Certain topics in telegraph transmission theory*. In: AIEE Transactions **47** (1928), pp. 617–644.
- [56] N. Wiener. *Generalized harmonic analysis*. In: Acta Mathematica **55** (1930), pp. 117–258.
- [57] A. Y. Khinchin. *Korrelationstheorie der stationären stochastischen Prozesse*. In: Math. Annalen **109** (1934), pp. 604–614.
- [58] Ming Zhao et al. *Afterpulsing and its correction in fluorescence correlation spectroscopy experiments*. In: Applied Optics **42**, 19 (2003), pp. 4031–4036.
- [59] Henri Dautet et al. *Photon counting techniques with silicon avalanche photodiodes*. In: Applied Optics **32**, 21 (1993), pp. 3894–3900.
- [60] Goro Nishimura and Masataka Kinjo. *Dead-time distortion in fluorescence correlation measurements*. In: Applied Optics **44** (2005), pp. 3458–3467.
- [61] M. Höbel and J. Ricka. *Dead-time and afterpulsing correction in multiphoton timing with nonideal detectors*. In: Rev. Sci. Instrum. **65**, 7 (1994), pp. 2326–2336.
- [62] Ekkehard Overbeck and Christian Sinn. *Silicon avalanche photodiodes as detectors for photon correlation experiments*. In: Rev. Sci. Instrum. **69** (1998), pp. 3515–3523.
- [63] Tilman Butz. *Fouriertransformation für Fußgänger*. B. G. Teubner, Stuttgart, 2000.
- [64] Gerhard Heinzel, Albrecht Rüdiger, and Roland Schilling. *Spectrum and spectral density estimation by the Discrete Fourier transform (DFT), including a comprehensive list of window functions and some new flat-top windows*. In: Max Planck Society eDoc server 395068 (2002).
- [65] F. J. Harris. *On the Use of Windows for Harmonic Analysis with the Discrete Fourier Transform*. In: Proceedings of the IEEE **66**, 1 (1978), pp. 51–83.
- [66] P. S. Jessen et al. *Observation of Quantized Motion of Rb Atoms in an Optical Field*. In: Phys. Rev. Lett. **69**, 1 (1992), pp. 49–52.
- [67] Nathan Brahm et al. *Optical Detection of the Quantization of Collective Atomic Motion*. In: Phys. Rev. Lett. **108**, 133601 (2012).
- [68] Marc Bienert and Giovanna Morigi. *Cooling the motion of a trapped atom with a cavity field*. In: arXiv:1208.5942v1 (2012). URL: <http://arxiv.org/abs/1208.5942v1>.
- [69] C. Cohen-Tannoudji, J. Dupont-Roc, and G. Grynberg. *Atom-Photon Interactions: Basic Processes and Applications*. John Wiley and Sons, 1998.
- [70] H. J. Carmichael. *Statistical Methods in Quantum Optics*. Springer, 2002.
- [71] J. Eschner et al. *Laser cooling of trapped ions*. In: J. Opt. Soc. Am. B **20**, 5 (2003), pp. 1003–1015.

- [72] M. Lindberg and S. Stenholm. *The master equation for laser cooling of trapped particles*. In: J. Phys. B: At. Mol. Phys. **17** (1984), pp. 3375–3389.
- [73] Stig Stenholm. *The semiclassical theory of laser cooling*. In: Reviews of Modern Physics **58**, 3 (1986), pp. 699–739.
- [74] E. Mathieu. *Mémoire sur le mouvement vibratoire d'une membrane de forme elliptique*. In: Journal de Mathématiques pures et appliquées (1868), pp. 137–203.
- [75] E. T. Jaynes. *Probability Theory: The Logic of Science*. Cambridge University Press, 2003.
- [76] G. Grynberg and C. Robilliard. *Cold atoms in dissipative optical lattices*. In: Physics Reports **355** (2001), pp. 335–451.
- [77] O. Cappé, E. Moulines, and T. Ryden. *Inference in Hidden Markov Models*. Springer, 2000.

Danksagung

Zunächst möchte ich mich bei Herrn Professor Meschede dafür bedanken, dass ich meine Masterarbeit in seiner Arbeitsgruppe anfertigen durfte und somit die Möglichkeit erhalten habe in einem komplexen und zugleich spannenden Experiment mitarbeiten zu dürfen. Während meiner Zeit in der Arbeitsgruppe habe ich es genossen, in einem solch internationalen Umfeld zu arbeiten und die stete Unterstützung für Besuche von Konferenzen und Seminaren zu erfahren.

Des weiteren möchte ich Herrn Professor Fiebig danken, der sich als Zweitgutachter für diese Arbeit zur Verfügung gestellt hat, obwohl er mittlerweile in Zürich forscht und lehrt.

Weiterhin gilt mein Dank allen Gruppenmitgliedern, die mich bei meiner Masterarbeit unterstützt haben:

- Zunächst möchte ich mich hier besonders bei René bedanken, der mich ein Jahr lang hervorragend betreut und tapfer ertragen hat. Die vielen Stunden mit dir im Labor haben mir wirklich viel Freude bereitet, René!
- Außerdem möchte ich mich bei Tobias und Seokchan für die vielen spannenden physikalischen Diskussionen, welche zum Gelingen dieser Arbeit beigetragen haben, und den Rat, mit dem sie mir stets beiseitestanden, bedanken.
- Ein besonderer Dank gilt hier auch Wolfgang, der immer wieder bereit war, über Probleme zu diskutieren und es besonders verstand diese einfach darzustellen.
- In der Teepause gab es Gelegenheit sich mit den anderen Gruppenmitgliedern auch über Themen abseits der Physik auszutauschen und über die einzelnen (kulturellen) Sichtweisen zu diskutieren, was ich sehr bereichernd fand.
- René, Tobias, Seokchan, Wolfgang und Deena möchte ich weiterhin danken, Teile meiner Arbeit Korrektur gelesen zu haben.

Mit dem Ende meines Studiums möchte ich auch meinen Eltern danken, die mich während der gesamten Studienzeit finanziell unterstützt haben.

Der größte Dank geht an meine Freundin, die mich während der gesamten Masterarbeitszeit, und besonders kurz vor der Abgabe, unterstützt und vorzüglich bekocht hat. Vielen Dank, liebe Lotte!

Statutory declaration

I hereby certify that the work presented here was accomplished by myself and without the use of illegitimate means or support, and that no sources and tools were used other than those cited.

Bonn, October 22nd 2012

Submission date: October 22nd 2012